A Study on Azimuthal Decorrelation between Jets with Large Rapidity Separation

Chang Lyong Kim
Department of Physics
Graduate School
Korea University

January 11, 1996

Contents

1 Introduction **1**

2 Quantum Chromodynamics **3**

2.1 QCD Theory from Experiments 3

2.2 The Quark-Parton Model 5

2.3 Perturbative QCD and Asymptotic Freedom 7

2.4 Factorization Theorem 8

2.5 The Structure Function 11

2.5.1 Parton Distributions 14

2.5.2 Evolution of Parton Distributions 14

2.5.3 GLAP and BFKL evolution 18

2.5.4 Application of the GLAP Evolution 24

2.5.5 Application of the BFKL Evolution 26

3 Dijet Production **29**

3.1 Kinematics 29

3.2 The definition of a Jet 30

3.3 Dijet production with BFKL 32

3.3.1 Dijet inclusive cross section 34

3.3.2 The Results 37

4 The DØ Detector **41**

4.1 Detector Overview 41

4.2 The Central Detector 43

4.3 The Calorimeter 46

4.3.1 Operation Principles 49

4.3.2 Massless Gap and InterCryostat Detectors 51

4.3.3 Calorimeter Performance 51

4.4 The Muon System 53

4.5 The Trigger system 53

5 Jet Reconstruction **56**

5.1 DØ Cone Algorithm 56

5.2 Jet Energy Scale Correction 59

5.3 Energy Resolution 65

5.4 Position Bias Corrections and Position Resolution 68

5.4.1 η Bias 69

5.4.2 η bias correction 71

5.4.3 ϕ Bias 71

5.4.4 Position Resolution 74

5.5 Reconstruction Efficiency 74

5.6 Trigger Efficiency 80

6 Data Selection and Analysis **83**

6.1 Luminosity 83

6.2 Data Sample 85

6.2.1 Bad Data Runs 85

6.2.2 Multiple Interactions 86

6.2.3 η Bias Correction 88

6.2.4 Good Jet Quality Cuts 89

6.2.5 Energy Scale Correction 90
6.3 Analysis 90
6.3.1 Analysis Cuts 91
6.3.2 Characteristics of two tagged jets 95
6.3.3 $< \cos[n(\pi - \Delta\phi)] >$ 96

7 Systematics **102**
7.1 Jet Energy Scale Uncertainty 102
7.1.1 Jet Energy Scale V4.0 102
7.1.2 Out-of-Cone Showering Correction 104
7.2 Intercryostat Detector Region 105
7.3 Good Jet Quality Cut 108
7.4 Jet Position Biases and Resolutions 110
7.4.1 Position Biases 110
7.4.2 Position resolution 110
7.5 Summary 111

8 Theoretical Predictions **117**
8.1 JETRAD 117
8.2 HERWIG 121
8.3 GEANT Detector Simulation 126
8.4 BFKL Prediction 127

9 Comparisons to Theory and Conclusions **129**
9.1 Experimental Results and Comparison 129
9.2 Conclusions 132

List of Figures

2.1 The interactions between quarks and gluons 4

2.2 The running strong coupling constant: $\alpha_s(Q^2)$, courtesy of J. Yu. (Ph.D. thesis, New York university at Stony Brook, 1993.) 7

2.3 Factorization of the single hadron inclusive cross section at large p_t, See Eq.(2.2) 9

2.4 Kinematic variables for deep inelastic electron-proton scattering . . . 10

2.5 Comparison of the measured structure function $F_2(x, Q^2)$ (ZEUS data in 1993) with NLO parton densities. 12

2.6 (a) the proton interacting with a virtual photon, γ^* (b) $\gamma^* q \rightarrow q, O(\alpha)$ (c) $\gamma^* q \rightarrow qg$, quark contribution at $O(\alpha\alpha_s)$ (d) $\gamma^* g \rightarrow q\overline{q}$, gluon contribution at $O(\alpha\alpha_s)$ (e) $\gamma^* q \rightarrow qgg$, quark contribution at $O(\alpha\alpha_s^2)$. 13

2.7 The Evolution of Parton Distributions 20

2.8 (a) GLAP and (b) BFKL evolutions ($\gamma^* q$ or $\gamma^* g$) 21

2.9 An example of GLAP evolution using MRSD'$_-$ structure function; u_v for *up valence* quark, u_{sea} for *up sea* quark, g for *gluon* as a function of momentum fraction x. 23

2.10 (a) Pomeron exchange in double diffractive $p\bar{p}$ scattering, (b) Feynman Ladder diagram for colorless two gluon exchange, Pomeron, (c) Scattering amplitude for t channel jet production. The scattering amplitude (c) is the same as (b). 27

3.1 Evolution of a jet 31
3.2 Multigluon amplitude a) at tree level b) with the virtual radiative corrections, represented by the thicker gluon line. 34
3.3 Feynman diagrams for a) $gg \rightarrow gg, O(\alpha_s^2)$ b) $gg \rightarrow ggg, O(\alpha_s^3)$ c) $gg \rightarrow gggg, O(\alpha_s^4)$. 36
3.4 A comparison between leading order and higher order effect in $\Delta\phi$ and $< \cos(\pi - \Delta\phi) >$ distributions. 38
3.5 From top to bottom, relative to the peak, the solid lines are the normalized $\Delta\phi$ distributions at $\Delta\eta = 5$, 6 and 7. (Here, $\phi = \Delta\phi$) . . 39

4.1 The DØ Detector 42
4.2 The DØ tracking system 43
4.3 The DØ Calorimeter 47
4.4 A cross section of the calorimeter 48
4.5 The layer structure of the DØ calorimeter 49
4.6 A typical unit cell of the calorimeter 50

5.1 Jet Energy Scale Correction Version 4.2: The top plot shows the jet energy scale as a function of jet E_T at $\eta = 0.0$, and the bottom at $\eta = 2.0$. The dotted and dashed lines represent $\pm 1\sigma$ uncertainty. . . . 64
5.2 Jet Energy Resolution as a function of Scale Corrected Jet E_T in all η regions for R = 0.7 cone jets. 67
5.3 HERWIG Monte Carlo simulation of the η bias for all jet energies(GeV) as a function of η_d^{reco}. 70
5.4 HERWIG Monte Carlo simulation of the η bias. $< \delta(E_{jet}^{reco}, \eta_d^{reco}) >$ before the correction are plotted as solid crosses. The dotted crosses represent the bias after the correction. 72
5.5 HERWIG Monte Carlo simulation of the η bias between parton jets and particle jets as a function of $\eta_d^{particle}$ and energies (GeV) 73

5.6 HERWIG Monte Carlo simulation of the ϕ bias between parton jets and calorimeter jets as a function of η_d^{reco} and energies (GeV). 75
5.7 The η resolution from a HERWIG Monte Carlo simulation. 77
5.8 The ϕ resolution from a HERWIG Monte Carlo simulation. 77
5.9 Jet reconstruction efficiency as a function of parton jet E_T using HERWIG4.6 and DØ GEANT. 79
5.10 Jet reconstruction efficiency as a function of pseudorapidity using HERWIG5.8 and DØ GEANT. 81
5.11 Total L1L2 event efficiency for JET_LOW: a) $0.0 < |\eta| < 0.6$, b) $0.6 < |\eta| < 1.6$, c) $1.6 < |\eta| < 4.0$, d) $0.0 < |\eta| < 4.0$. 82

6.1 (a) Multiple interaction flag (MUL_INTF) distributions for JET_LOW, (b) longitudinal vertex distributions for each flag, (c) number of jets for each flag with $P_T^{min} = 8$GeV, (d) number of jets for each flag with $P_T^{min} = 20$GeV. 87
6.2 (a) The distribution of jets in η and ϕ space, (b) transverse energy, (c) pseudorapidity, (d) azimuthal angle distributions of the leading, 2nd, and 3rd jets after ordering in E_T. 92
6.3 (a) The scatter plot of the two tagging jets for E_T and b) for azimuthal angle ϕ, c) jet multiplicity distribution, d) the distribution of rapidity interval ($\Delta\eta = \eta_{forward} - \eta_{backward}$) between the two tagging jets. . . 93
6.4 The scatter plot of the two tagging jets in η space. 94
6.5 Jet multiplicity distribution for various bins of rapidity interval (no $\bar{\eta}$ cut is applied). 96
6.6 (a) Average jet multiplicity distribution, (b) forward jet E_T distributions for $\Delta\eta = 1$, 3, and 5 bins. (c) Average jet multiplicity distribution, (d) forward jet E_T distributions for $\Delta\eta = 1$, 3, and 5 bins with $\bar{\eta} \leq 0.5$. 97

6.7 Pseudorapidity distributions of the two tagging jets, forward jet (jet 1) and backward jet (jet 2), as a function of rapidity intervals: Solid lines are for no rapidity boost cut and the dotted lines for rapidity boost cut. 98
6.8 (a) Azimuthal angle difference, $\Delta\phi = \phi_{forward} - \phi_{backward}$, for various rapidity intervals, 1, 3 and 5, without the $\bar{\eta}$ cut, (b) with the $\bar{\eta}$ cut. The distributions are normalized to unit area. 99
6.9 Average values of the correlation variables $\cos[n(\pi - \Delta\phi)]$ versus $\Delta\eta$ for the first moment $n = 1$ and second moment $n = 2$. 100

7.1 The dotted lines represent $< \cos[n(\pi - \Delta\phi)] >$ with the low jet energy scale correction, the dashed lines for the high energy correction, and the solid circles for the nominal values. Only statistical errors are shown. 103
7.2 The jet energy scale correction as a function of pseudorapidity at fixed transverse momenta, 25 GeV and 40 GeV. 105
7.3 The pseudorapidity distribution for, (a) the leading jets and (b), the second leading jets ($E_T > 20$ GeV). Note the excess in the ICR. . . . 106
7.4 The solid circle represent the average of $\cos(\pi - \Delta\phi)$ with ICR jets, and the open triangles without ICR jets. 107
7.5 (a) The distribution of the electromagnetic fraction (EMF) after the hot cell fraction (HCF) cut and the coarse hadronic fraction (CHF) cut are applied. (b) The solid line represents the jets removed with the $0.05 <$ EMF < 0.95 requirement, and the dotted line with 0.07 $<$ EMF < 0.92. 108
7.6 The solid circles represent the average of $\cos(\pi - \Delta\phi)$ with the standard good jet cuts, and the open triangles without those cuts. 109
7.7 The comparison of the systematic errors for $\Delta\eta = 0$ through 5 (n=1). See text for details. (continues in the next page). 114

8.1 The distributions of azimuthal angle differences for various rapidity intervals 1, 3, and 5 (a) without $\bar{\eta}$ cut and (b) with $\bar{\eta} < 0.5$ in JETRAD. The distributions are normalized to unit area. 118
8.2 (a) JETRAD $< \cos(\pi - \Delta\phi) >$ values with and without exclusion of the one central bin, (b) $< \cos(\pi - \Delta\phi) >$ values using various renormalization scales, (c) using different pdf's, (d) using two different jet algorithms. 120
8.3 The distributions of the azimuthal angle differences for various rapidity intervals 1, 3, and 5 (a) without $\bar{\eta}$ cut and (b) with $\bar{\eta} < 0.5$ using the parton jets of HERWIG. The distributions are normalized to unit area. 123
8.4 The average of $\cos(\pi - \Delta\phi)$ using HERWIG events, (a) for comparison between parton and particle jets and, (b) for the effects of rapidity boost cut. 124
8.5 The evolution of azimuthal angle decorrelations from parton level to particle and calorimeter levels. Particle jets contain the effects of fragmentation and calorimeter jets contain the effects of particle showering in the calorimeter. 125
8.6 The showering uncertainty: $\frac{(<\cos>_{cajet} - <\cos>_{pejet}) + (<\cos>_{cajet} - <\cos>_{pjet})}{2}$ for (a) the first moment and (b) the second moment. 126
8.7 The average of $\cos[n(\pi - \Delta\phi)]$ with and without $\bar{\eta}$ cut using BFKL resummation. 128

9.1 The average of $\cos(\pi - \Delta\phi)$ as a function of rapidity interval, for the experimental data, JETRAD, HERWIG, and the BFKL predictions of Del Duca and Schmidt. (for the first moment, n = 1) 130
9.2 The average of $\cos 2(\pi - \Delta\phi)$ as a function of rapidity interval, for the experimental data, JETRAD, HERWIG, and the BFKL predictions of Del Duca and Schmidt. (for the second moment, n = 2) 131

List of Tables

2.1 Comparison of GLAP and BFKL evolution 24

4.1 Characteristics of the Central Detector 45

4.2 The performance of the DØ calorimeter 52

4.3 The jet triggers. The z-vertex position is given in cm and E_t thresholds in GeV. The z-vertex is not always applied to JET_HIGH. JT(n,E_t) means that at least **n** trigger towers had transverse momentum greater than the minimum E_t. L2JT(n,E_t) is for jets, not for trigger tower, and means that at least **n** jets had transverse momentum greater than E_t. 55

5.1 Jet energy resolution as a function of pseudorapidity interval. 68

5.2 η bias parameterization for $|\eta_d| \in$ [0.1,1.8]. 76

5.3 η bias parameterization for $|\eta_d| \in$ [1.8,3.0]. 76

5.4 η bias parameterization for $|\eta_d| > 2.4$. 76

5.5 Parameterization of the jet η resolution. 78

5.6 Parameterization of the jet ϕ resolution. 78

6.1 Average values of the correlation variables, $\cos[n(\pi - \Delta\phi)]$, versus $\Delta\eta$ for the first moment $n = 1$ and second moment $n = 2$ with their statistical errors. See Fig. 6.9. 101

7.1 The lists of statistical errors and the differences between $< \cos(\pi - \Delta\phi) >_{extremes} - < \cos(\pi - \Delta\phi) >_{nominal}$ for the first moment n=1. See text for details. 112
7.2 The lists of statistical errors and the differences between $< \cos 2(\pi - \Delta\phi) >_{extremes} - < \cos 2(\pi - \Delta\phi) >_{nominal}$ for the first moment n=2. See text for details. 113

Abstract

We present the first experimental measurement of jet–jet azimuthal correlation as a function of the rapidity interval between two jets. The data were accumulated using the DØ detector during the 1992–93 collider run of the Fermilab Tevatron at $\sqrt{s} = 1.8$ TeV. These results are compared to next–to–leading order (NLO) QCD predictions and to two leading–log approximations (LLA) where the leading–log terms are resummed to all orders in α_s. The final state jets as predicted by NLO QCD are more correlated azimuthally than the data. The parton shower LLA Monte Carlo HERWIG describes the data well and the analytical LLA prediction based on BFKL resummation is found to be less correlated than the data.

Chapter 1

Introduction

Matter, as currently understood, consists of two types of elementary particles: quarks and leptons. These are the fundamental building blocks of the Universe including our bodies. We also believe that the electromagnetic, weak, and strong forces describe the behavior of these elementary particles and, somehow, the harmony between the interaction forces and the elementary particles creates the most exotic phenomenon, life.

For the last forty years, comprehensive theories have been established to describe the behavior of the elementary particles and interactions between these particles. Quantum Chromodynamics (QCD), as one of such, is believed to be a precise and complete theory of quarks and gluons explaining various strong interaction phenomena. Since the strong force keeps quarks and gluons from manifesting themselves directly, jets or collimated sprays of hadrons, are the physical observable in the experimental situations.

Including recent progress in next–to–leading order (NLO) calculations, perturbative QCD has been quite successful in the description of high p_T central jet production at hadron colliders, such as the inclusive single jet [1] and dijet cross sections [2]. Along with this advance in the understanding of perturbative QCD, the higher energy colliders, such as the Fermilab Tevatron ($p\bar{p}$) and HERA(ep), have opened up a new era in the study of perturbative QCD including investigation of diffractive and small-x physics [3].

These new perturbative QCD regimes or equivalently higher order phenomena may be described by summing all orders in α_s, and not just by fixed order perturbative QCD. The BFKL resummation [4] calculation formulated by Balitsky, Fadin, Kuraev and Lipatov predicts that these higher order contributions manifest themselves as enhanced radiation accompanying a hard scattering process. This enhanced radiation effect may be observed at the Fermilab Tevatron $p\bar{p}$ Collider at $\sqrt{s} = 1.8$ TeV. Experimentally, additional radiation can be revealed by the transverse momentum and azimuthal angle correlations between dijets with large rapidity separation. In particular, the enhanced radiation is expected to reduce the azimuthal correlation of two jets.

We have studied the azimuthal correlation between the two jets with the largest rapidity separation above certain minimum transverse momentum in events produced in the Tevatron $p\bar{p}$ collisions. In leading order, these two jets will be absolutely correlated in both transverse momentum and azimuthal angle. With additional radiation the degree of this correlation is expected to be decreased. These higher order effects become particularly interesting as the rapidity interval between the hard scattering jets becomes large.

This dissertation reports the first measurement of azimuthal angle correlation at rapidity separations of up to five units. The correlation as a function of rapidity interval is compared to various QCD predictions which treat higher order terms differently. The DØ detector [5] is particularly suited for this study since the hermetic calorimetric coverage to $|\eta|$ of 4.0 makes it possible to extend the measurement of azimuthal correlation to rapidity intervals up to five units.

Chapter 2

Quantum Chromodynamics

Quantum Chromodynamics (QCD) is a non-Abelian gauge theory with a three dimensional gauge symmetry, SU(3) of color. In contrast Quantum Electrodynamics (QED) is based on an Abelian gauge theory with one dimensional local phase rotation, U(1) of electric charge. This difference in the underlying symmetry produces a significant complication in the interactions of the carriers of force. In QED, only photons interact with electrically charged fermions or antifermions because photons do not carry electric charge. In QCD, on the other hand, there are three- and four–gluon interactions possible, since the gluons do carry the color charge, as well as gluon–quark–antiquark interactions as shown in Fig. 2.1.

2.1 QCD Theory from Experiments

In retrospect, experimental results have motivated the birth of QCD. Therefore, we will briefly review the main experimental developments which have led to the formulation of QCD and thus illustrate its origin while reinforcing our belief that QCD is an accurate theory of the strong interaction.

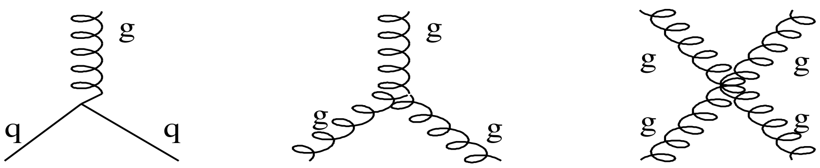

Figure 2.1: The interactions between quarks and gluons

Why quarks? In 1964 Gell-Mann and Zweig suggested the quark model [6] that described the hadron spectrum known at that time. They have introduced three very curious particles, **quarks**(u, d, s), having fractional electrical charges and baryonic quantum numbers. This quark model reduced the "zoo" of hadrons to simple combinations of those quarks, mesons consisting of quark-antiquark pairs, and baryons of three quarks. With the successful description of hadron structure, quarks became the essence of QCD.

Why color? The quark model includes hadrons which consist of identical quarks. In particular, the Δ^{++} contains three u quarks with no orbital angular momentum in a symmetric S= 3/2 spin state. According to the Pauli principle, one cannot build such baryons from quarks with a symmetrical coordinate wave function. That is, it is impossible to have an antisymmetrical wave function for Δ^{++}. A solution to this puzzle was to increase the number of quarks by introducing a new quantum number, **color** [7]. One needs at least three color charges, such as *red, green and blue*, for each quark flavor to describe the spectrum of baryons, e.g. the Δ^{++} hyperon consists of three u quarks of different colors. Since then, there has been a great deal of experimental evidence for three color charges [8]. One of the examples is that the ratio $R = \frac{\sigma(e^+e^- \rightarrow hadrons)}{\sigma(e^+e^- \rightarrow \mu^+\mu^-)}$ depends on the sum of the squares of the electric charges of all types of quarks available since an intermediate virtual photon annihilates into a quark-antiquark pair. The experimental results have been consistent with the existence of three color charges for each quark flavor.

Why gluons? All the attempts to find free quarks have failed. A strong force, overruling the electromagnetic repulsion of the three u quarks in the Δ^{++} hyperon, must be invoked to bind quarks into hadrons. The color charge of quarks yields a new color field making this strong binding possible. It is only natural to assume intermediate particles for the strong force as in the electromagnetic force of QED. This intermediate particle, the **gluon**, is the quanta of the color field that binds quarks into nucleons and also nucleons into nuclei.

In 1954 Yang and Mills [9] constructed a non–Abelian gauge theory, analogous to QED, for a system in which the particle carries more than one "charge". Their generalization of two charges mediated by a vector particle resulted in a theory that was inconsistent with observation. However, with three charges mediated by vector particles obeying exact SU(3) symmetry one arrived at a theory that seemed to describe the strong interactions. It is the color charges of gluons that are represented by SU(3) symmetry. This is an essential feature of QCD and yields three and four gluon vertices. Inclusion of gauge invariance to ensure the masslessness of the gluon is the last ingredient of QCD which describes the strong interactions [10].

2.2 The Quark-Parton Model

Since the beginning of history in science, scientists have simplified the phenomena of the Nature by describing only its essential components. In order to understand, for example, e^+e^- interactions using QED, the assumption that the electron is a point-like particle with no substructure makes the theoretical prediction simpler without the loss of physical insight. As a matter of fact, many experimental attempts to find the substructure of the electron have failed, and, therefore, the electron is believed to be a point-like particle. The proton was also believed to be a point-like particle until a series of deep inelastic scattering (DIS) experiments ($e+p \rightarrow e+X$) at the Stanford Linear Accelerator (SLAC) in the late 1960s showed the proton to be made of hard point-like objects, so called, **partons**. Bjorken [11] suggested that the structure function of a proton is a function of only one variable x, parton momentum fraction, and this scaling behavior of the structure functions was dramatically confirmed by a series of experiments at SLAC. The scaling effect was found to be a result of the fact that the proton is made of point-like constituents. Expectations that the charged constituents of the proton carry spin 1/2 was also confirmed experimentally [13]. The experimental verification of Bjorken scaling and the observation of spin 1/2 constituents in deep inelastic scattering have provided the first evidence for the existence of quarks and given impetus to the intuitive picture of the **quark-parton model**.

In such a naive quark-parton model, the proton was regarded as a collection of point-like partons (or quarks) and, at high energy DIS, a virtual photon interacts with a single free quark. As soon as the naive quark-parton model was established physicists have started exploring the quark probability distributions with many DIS experiments using e, μ, and ν beams and various targets [14]. One result of these experiments was that the momentum sum of all the charged quarks inside the proton was only 50% of the total proton momentum. This indicated that a substantial fraction of the proton momentum is carried by neutral partons, but not by charged quarks. Those neutral partons were identified as gluons. In the quark-parton model, at last, the gluons are also considered as point-like partons residing inside the proton. Presently, the QCD parton model suggests that *the proton is believed to be an ensemble of point-like partons (guarks and gluons) undergoing incessant color interactions.*

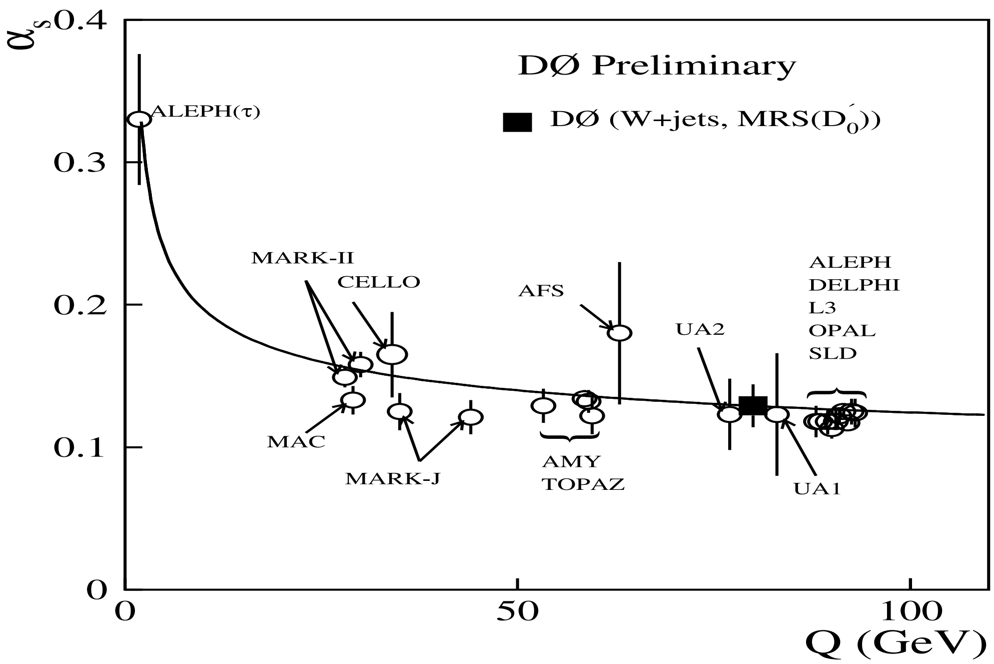

Figure 2.2: The running strong coupling constant: $\alpha_s(Q^2)$, courtesy of J. Yu. (Ph.D. thesis, New York university at Stony Brook, 1993.)

2.3 Perturbative QCD and Asymptotic Freedom

Due to the characteristics of strong interactions single quarks can not be isolated from other quarks and exist only as constituents of colorless hadrons. This confinement of quarks to colorless hadrons is a result of strong couplings between color charged particles. Despite of color confinement various QCD predictions have been calculated perturbatively and compared with experimental results.

The quark-parton model assumes the quarks behave as if they were free Dirac particles, i.e. no mutual interactions occur between them. Since Bjorken scaling [11] is relevant only at large momentum transfer ($Q^2 \to \infty$) we may infer that *over the short time scale in which the hard scattering takes place, the quarks act as free particles.* This motivated the hunt for a field theory of quarks which would describe quarks as free particles in the limit, $Q^2 \to \infty$. In other words, the effective *color charge* of quarks in an interaction vanishes as distances become smaller and smaller. This is called **Asymptotic Freedom**.

In the early of 1970s, several theorists established that non-Abelian gauge theories had the important property of *asymptotic freedom* and consequently QCD became the field theory of strong interaction. As shown in Fig. 2.2, results from many experiments now show that the QCD coupling constant α_s approaches zero in the asymptotic limit, $Q^2 \to \infty$. The small coupling at high Q^2 makes perturbative QCD (pQCD) possible and credible.

When one calculates higher order loop corrections [14] to the quark-gluon coupling, the result diverges. The renormalization procedure removes the divergence by introducing a mass scale, Λ, into the definition of the effective coupling. This prediction agrees well with many experimental results. The running QCD coupling constant at leading order is given by

$$\alpha_s(Q^2) = \frac{12\pi}{(33 - 2n_f)\log(Q^2/\Lambda^2_{QCD})} \tag{2.1}$$

where n_f is the number of quark flavors contributing in the loops and Λ^2_{QCD} is a QCD fundamental parameter which is to be determined experimentally [14]. If $Q^2 \to \Lambda^2$, the coupling constant diverges and the perturbative QCD fails. This leads to the confinement of quarks and gluons inside the proton. Thus, the parameter Λ^2 provides an approximate boundary energy scale between perturbative and the non-perturbative QCD.

2.4 Factorization Theorem

In hadron-hadron collisions, the scattering process can be factorized into two processes: a) a short-distance process, characterized by a hard scale Q, explaining the primary scattering between the partons; and, b) a long-distance region, characterized by a hadronization scale $\sim \Lambda_{QCD}$, describing how the scattering partons split

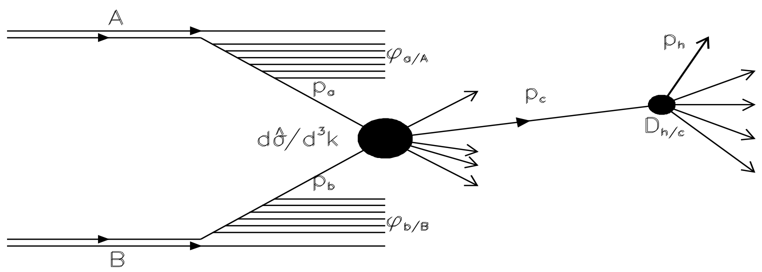

Figure 2.3: Factorization of the single hadron inclusive cross section at large p_t, See Eq.(2.2)

from the parent hadrons and how the final partons hadronize [15]. This **factorization** disentangles the complex hadron collision into several calculable or measurable parts. For example, the cross section for high p_t (large scale Q) single hadron inclusive production in hadron-hadron collisions $(A(p_a) + B(p_b) \rightarrow h(p_h) + X)$ [10] can be factorized as follows,

$$\begin{aligned} E_h \frac{d\sigma}{d^3p_h} &= \sum_{abc} \int_{x_a^{min}}^{1} dx_a \int_{x_b^{min}}^{1} dx_b \frac{dz}{z} \phi_{a/A}(x_a, \mu) \phi_{b/B}(x_b, \mu) \\ &\times \mid \vec{k}_c \mid \frac{d\hat{\sigma}}{d^3k_c} (\frac{p_c}{z\sqrt{s}}, \mu) D_{h/c}(z, \mu) \end{aligned} \tag{2.2}$$

which is also depicted in Fig. 2.3. The sum is over the various flavors of partons, i.e. quarks, antiquarks and gluons which take part in the hard scattering. The cross section is represented as a convolution of a short-distance process and two long distance processes:

a) short-distance (intermediate state): $\mid \vec{k}_c \mid \frac{d\hat{\sigma}}{d^3k_c}$ is for the hard scattering process $(a + b \rightarrow c + X)$ having a high p_t scale at the parton level. This can be calculated perturbatively due to the large p_t. The renormalization scale or factorization scale μ is arbitrary, but it is large enough for the perturbative calculation. In general, the

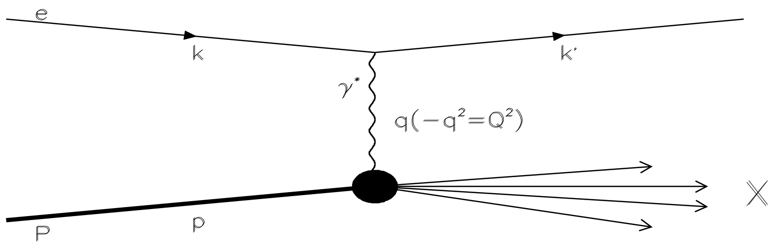

Figure 2.4: Kinematic variables for deep inelastic electron-proton scattering

scale μ is chosen near the large scale of the process, e.g. $\mu \sim p_t$.

b) long-distance (initial and final states): the parton distribution function, $\phi(x, \mu)$, is the probability density to find parton $a(b)$ having the momentum fraction $x_a(x_b)$ of the parent hadron A(B). These parton densities are to be measured experimentally in deep inelastic scattering since they are not calculable. The fragmentation function, $D_{h/c}(z, \mu)$, is the probability of finding hadron h among all the hadrons fragmented from a parton type c. The fractional momentum of the measured hadron relative to its parent parton c is z. The fragmentation is also non-perturbative process and can not be calculated theoretically.

At large p_t scales the hard process takes place over the short time scale phenomena in which the partons of the process can be considered as free particles. Therefore we may consider factorization a simple consequence of the quark-parton model. Factorization is now the basis of all applications of perturbative QCD to hard processes.

2.5 The Structure Function

As mentioned above, deep inelastic scattering plays an important role in our view of proton structure. Figure 2.4 shows a typical deep inelastic electron-proton process. With the standard notations for DIS kinematic variables, $Q^2 = -q^2$, $x = Q^2/2p \cdot q$, $y = p \cdot q/p \cdot k$ with $s = Q^2/xy$ as indicated in Fig. 2.4, the cross section for $Q^2 < 10^3 \mathrm{GeV}^2$ is given by

$$\frac{d\sigma^{ep}}{dxdQ^2} = \frac{4\pi\alpha^2}{xQ^4}(1 - y + \frac{1}{2}\frac{y^2}{1 + R(x,Q^2)})F_2(x,Q^2) \tag{2.3}$$

where F_2 is the proton structure function and is proportional to the sum of σ_T and σ_L, the transverse and longitudinal virtual photon cross sections, respectively. The theoretical value [16] $R(= \sigma_L/\sigma_T = F_2/2xF_1 - 1)$ indicates the virtuality of the photon (a real photon does not have a longitudinal polarization, therefore $\sigma_L = 0$) and the spin of the quark (a spin 0 quark can not absorb a photon of helicity $\lambda = \pm 1$, so $\sigma_T = 0$) [17]. It is straightforward to extract the structure function F_2 by measuring the electron-proton cross section as a function of x and Q^2 from Eq.(2.3). The recent results on the structure function from the ZEUS experiment [18] are shown in Fig. 2.5.

The structure function $F_2(x, Q^2)$ reflects the kaleidoscopic world of the proton and depends on the momentum of the virtual photon probe as shown in Fig. 2.6(a). Figure 2.6(a) is a magnified picture of the electron-proton scattering shown in Fig. 2.4. The proton represented as a blob in Fig. 2.4 is a system of many partons interacting with each others as shown in Fig. 2.6(a). The probe or virtual photon encounters a different environment depending on its resolving power, sometimes almost empty space, sometimes crowded space. The proton was found to be an ensemble of partons, each parton carrying some fraction x of the total momentum of its parent proton. When a probe of a fixed $Q = Q_0$ enters the proton, it has a probability to see a parton with momentum fraction x as shown in Fig. 2.5. The

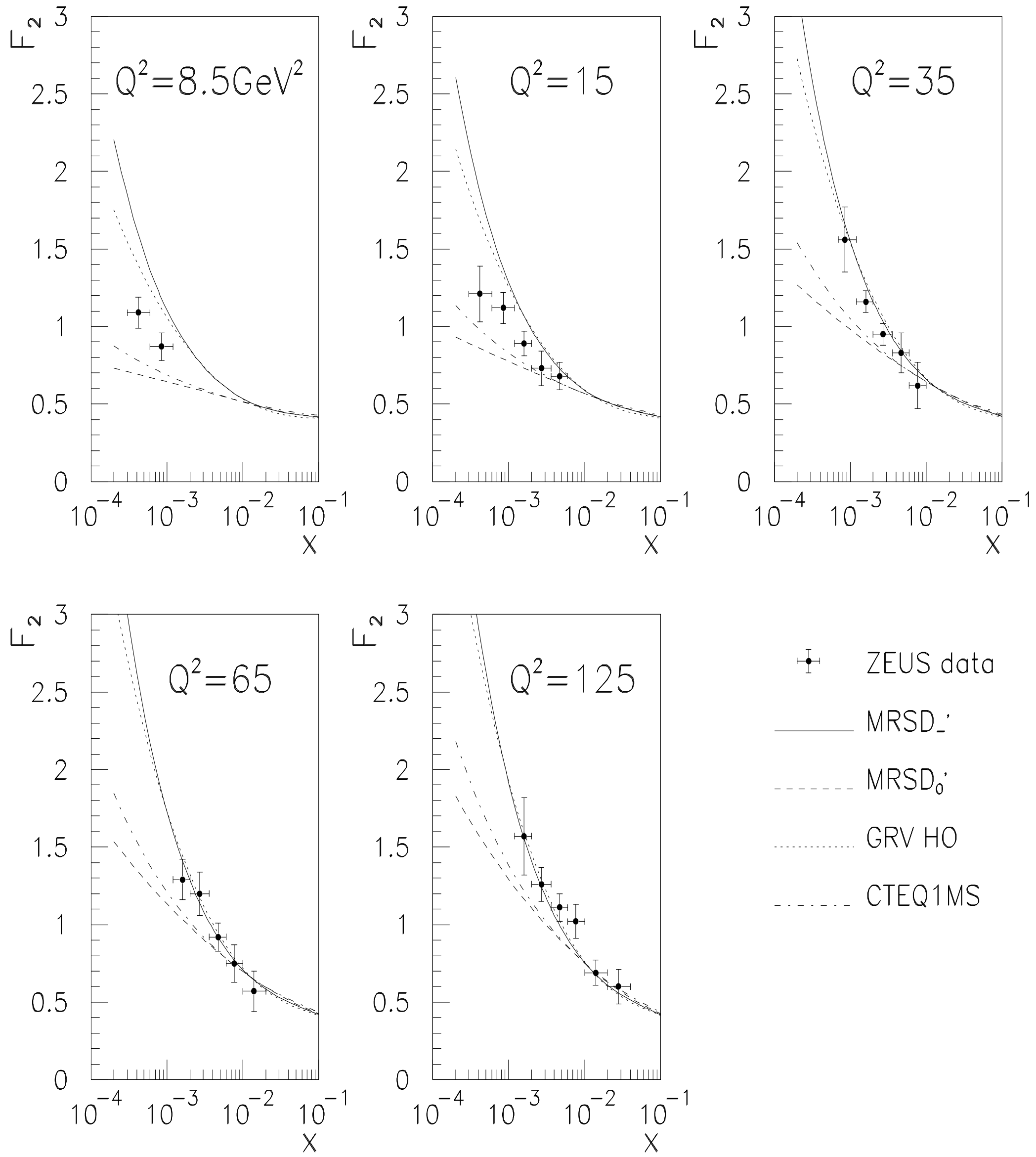

Figure 2.5: Comparison of the measured structure function $F_2(x, Q^2)$ (ZEUS data in 1993) with NLO parton densities.

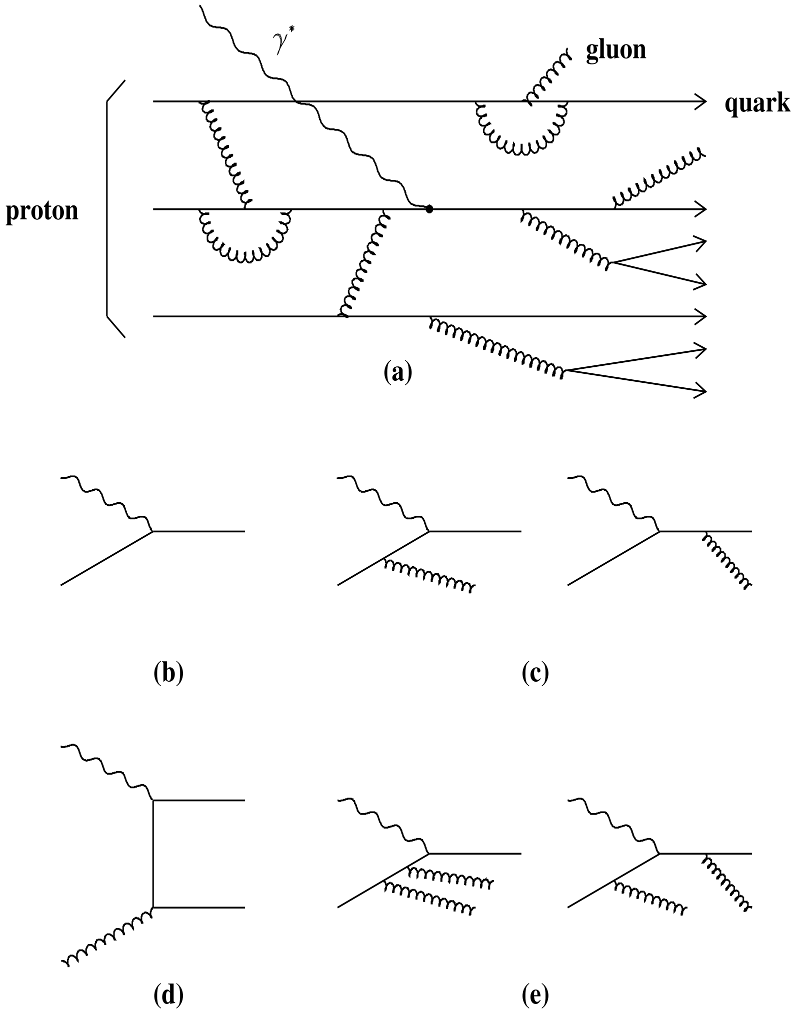

Figure 2.6: (a) the proton interacting with a virtual photon, γ^* (b) $\gamma^* q \rightarrow q, O(\alpha)$ (c) $\gamma^* q \rightarrow qg$, quark contribution at $O(\alpha\alpha_s)$ (d) $\gamma^* g \rightarrow q\bar{q}$, gluon contribution at $O(\alpha\alpha_s)$ (e) $\gamma^* q \rightarrow qgg$, quark contribution at $O(\alpha\alpha_s^2)$.

ZEUS data clearly show that $F_2(x, Q^2)$ increases very steeply at small x, and the number of partons carrying a small momentum fraction increases as Q^2 increases at a fixed $x = x_0$.

2.5.1 Parton Distributions

As mentioned in section 2.2, the proton structure function, $F_2(x, Q^2)$, consists of several parton probability densities. DIS experiments enable us to explore the different parton densities depending on the probing beams (e, μ, ν etc.) and targets particles (p, n etc.) [14]. For example, if we assume the structure function has no Q^2 dependence (Bjorken scaling), $F_2(x, Q^2)$ from the electron-proton DIS experiments is,

$$
\begin{aligned}
F_2^{ep}(x, Q^2) &= \sum_{i=1}^{N_f} e_i^2 [f_{q_i}(x) + f_{\overline{q}_i}(x)] \\
&\approx \frac{4}{9} x[u(x) + \overline{u}(x) + c(x) + \overline{c}(x)] \\
&+ \frac{1}{9} x[d(x) + \overline{d}(x) + s(x) + \overline{s}(x)] \qquad (2.4)
\end{aligned}
$$

where $f_{q_i}(x) \equiv x q_i(x)$ are the quark densities of the proton and e_i are the quark charges. For example, $u(x)$ [$\overline{u}(x)$] is the [anti] *up* quark density. In short, using DIS data one can measure the structure function, and application of the QCD parton model leads to the parton distribution functions (PDFs).

2.5.2 Evolution of Parton Distributions

We need F_2 for a wide x and Q^2 range to calculate, for example, one jet inclusive cross section from $p\bar{p}$ scattering. As mentioned in section 2.4, the one jet inclusive cross section can be factorized into two parts, the parton densities and the hard process. The parton density distributions at all x and Q^2 are necessary because the whole structure of the proton (anti-proton) is involved in jet production.

Experimentally it is next to impossible to scan all x and Q^2. In pQCD, however, $F_2(x)$ at a different Q can be surprisingly predicted by the experimental measurement of $F_2(x)$ at Q_0 when Q and Q_0 are large enough. Thus, for instance, measuring $F_2(x, Q_0)$ is enough to predict $F_2(x)$ for any Q^2. This means that even a single DIS experiment can produce the complete picture of the proton structure. This result, called the "evolution" of structure functions, is a distinct outcome of the factorization theorem. Figure 2.6(b-e) shows the Feynman diagrams that contribute to the parton distributions at $O(\alpha\alpha_s^n)$. By calculating each Feynman diagram, we can extract the following results.

In Figure (b) a virtual photon sees only a free quark as in the naive parton model. This is a pure electromagnetic interaction and describes Bjorken scaling theoretically. The result is given by,

$$\frac{F_2(x,Q^2)}{x} = \sum_i e_i^2 q_i(x) = \sum_i e_i^2 \int_x^1 \frac{dy}{y} q_i(y)\delta(1-\frac{x}{y}) \tag{2.5}$$

where i runs for all quark flavors.

In Figure (c) a virtual photon sees a quark interacting strongly through gluon emission. The outgoing quark would have some transverse momentum relative to the direction of the virtual photon. Figure(b) shows the outgoing quark collinear with the virtual photon. The transverse momentum emerging from the gluon emission provides the violation of Bjorken scaling. The violation of Bjorken scaling is an experimental signature of gluon emission. The integrated $\gamma^* - quark$ cross section is,

$$\hat{\sigma}(\gamma^* q \to qg) \simeq e_i^2 \hat{\sigma}_o \frac{\alpha_s}{2\pi} P_{qq}(z) \log \frac{Q^2}{\mu^2} \tag{2.6}$$

where $\hat{\sigma}_0 = 4\pi^2\alpha/\hat{s}$ and,

$$P_{qq}(z) = \frac{4}{3}(\frac{1+z^2}{1-z}) \tag{2.7}$$

represents the probability of a quark emitting a gluon and so becoming a quark with momentum reduced by a fraction z. The lower limit μ is a cutoff to regularize the divergence when the emitted gluon is soft ($p_t^2 \to 0$). Adding figures (b) and (c), we find gluon emission modifies Eq.(2.5) to become

$$\frac{F_2(x,Q^2)}{x} = \sum_i e_i^2 \int_x^1 \frac{dy}{y} q_i(y)(\delta(1-\frac{x}{y}) + \frac{\alpha_s}{2\pi} P_{qq}(\frac{x}{y}) \log\frac{Q^2}{\mu^2}). \tag{2.8}$$

The presence of the $\log Q^2$ factor means that the structure function describes the violation of Bjorken scaling. That is to say, in QCD F_2 is a function of Q^2 as well as of x, but the variation with Q^2 is only logarithmic.

Equation Eq.(2.8) may be regarded as the first two terms in a power series in α_s. As discussed in the section 2.3, α_s is small and a useful expansion parameter at large Q^2 since $\alpha_s \sim (\log Q^2)^{-1}$. But α_s of the second term is multiplied by $\log Q^2$, which means that perturbative expansion is not applicable since $\alpha_s \log Q^2 \sim 1$. In this form, Eq.(2.8) is not very useful. A good solution is to absorb the logarithmic term into a modified quark probability distribution. To this end, we may rewrite Eq.(2.8) in the "parton-like" form

$$\begin{aligned} \frac{F_2(x,Q^2)}{x} &\equiv \sum_i e_i^2 \int_x^1 \frac{dy}{y}(q_i(y) + \Delta q_i(y,Q^2))\delta(1-\frac{x}{y}) \\ &= \sum_i e_i^2(q_i(x) + \Delta q_i(x,Q^2)) \end{aligned} \tag{2.9}$$

where

$$\Delta q_i(x,Q^2) \equiv \frac{\alpha_s}{2\pi} \log\frac{Q^2}{\mu^2} \int_x^1 \frac{dy}{y} q_i(y) P_{qq}(\frac{x}{y}). \tag{2.10}$$

We can picture the above result as follows. At certain Q^2, the photons see the "point-like" quarks as shown in Fig. 2.6(b). If the quarks are noninteracting, no further structure would be resolved as Q^2 is increased and exact scaling would be true. The scaling is represented in the first term of Eq.(2.9). However, the second term, $\Delta q_i(y,Q^2)$ of Eq.(2.9), shows a Q^2 dependence of the structure function. As the resolving power Q^2 increases photons start to see quarks surrounded by a cloud of partons. Figure 2.6(c) and (d) represent a quark accompanied by a gluon and two gluons, respectively. The number of resolved partons increases with Q^2. But those partons have a smaller momentum fraction of the proton. In other words the larger the resolving power, the higher is the probability of finding a quark at small x and the less the chance of finding one at high x since high-momentum quarks lose momentum by radiating gluons.

The Q^2 evolution of the quark densities is calculated by QCD through Eq.(2.10). With the change in the parton density, $\Delta q_i(y, Q^2)$, and using $\Delta \log Q^2 (= \log Q^2 - \log \mu^2)$, the equation (2.10) can be written as follows;

$$\frac{d}{d \log Q^2} q_i(x, Q^2) = \frac{\alpha_s}{2\pi} \int_x^1 \frac{dy}{y} q_i(y, Q^2) P_{qq}(\frac{x}{y}). \tag{2.11}$$

It is known as "Altarelli-Parisi evolution equation" [17]. The equation shows that a quark with momentum fraction x ($q(x, Q^2)$ on the left-hand side) could have come from a parent quark with a larger momentum fraction y ($q(x, Q^2)$ on the right-hand side) which has radiated a gluon. This is an important consequence of QCD. Once we know the parton density at some reference point $q(x, Q_0^2)$, we can calculate it for any value of Q^2 using Altarelli-Parisi(AP) evolution equations.

So far the interactions of Fig. 2.6(b) and (c) are included in the evolution equation. We should also include the process $\gamma^* g \to q\overline{q}$ of Fig. 2.6(d). This represents a gluon producing a quark-antiquark pair to which the photon then couples. If we include it in the evolution of the quark density, the equation (2.11) becomes

$$\frac{dq_i(x, Q^2)}{d \log Q^2} = \frac{\alpha_s}{2\pi} \int_x^1 \frac{dy}{y} (q_i(y, Q^2) P_{qq}(\frac{x}{y}) + g(y, Q^2) P_{qg}(\frac{x}{y})). \tag{2.12}$$

where $P_{qg}(z)$ represents the probability that a gluon produces a $q\overline{q}$ pair such that the quark has a fraction z of the gluon momentum. Equation (2.12) is the evolution of the quark density.

Repeating the above argument for the gluon, we can calculate the gluon evolution equation,

$$\frac{dg(x,Q^2)}{d\log Q^2} = \frac{\alpha_s}{2\pi}\int_x^1 \frac{dy}{y}(\sum_i q_i(y,Q^2)P_{gq}(\frac{x}{y}) + g(y,Q^2)P_{gg}(\frac{x}{y})) \tag{2.13}$$

where $P_{gq}(z)$ represents the probability that a quark radiates a gluon such that the gluon has a fraction z of the quark momentum, and $P_{gg}(z)$ represents the probability that a gluon radiates another gluon such that the radiated gluon has a fraction z of parent gluon's momentum.

The evolution equation also shows the importance of the factorization theorem in QCD. The right-hand sides of Eq.(2.12) and Eq.(2.13) are divided into two parts, calculable and non-calculable. The AP equations P_{ij} are calculable using perturbative QCD. Non-calculable quantities, e.g. infrared divergence, can be included in the initial parton density, $q(x,Q^2)$ which requires a measurement. To factorize the evolution equation, we need to have a factorization scale μ_f which defines the separation of short-distance from long distance effects, as we discussed in section 2.4. Usually for convenience, we choose μ(renormalization scale) $= \mu_f = Q$.

2.5.3 GLAP and BFKL evolution

So far, we have discussed only the Q^2 evolution of the parton distribution. The parton density also depends on the parton momentum fraction x and can also evolve with x. The dominant role at small x is played by the gluon distribution, so first we consider only the gluon density which can be written as follows:

$$\begin{aligned} xg(x,Q^2) &= \sum_n C_n(Q_0^2)\alpha_s^n(L^n + a_{n-1}L^{n-1}...a_0) \\ &= C_0 + \\ &\quad C_1\alpha_s(L+a_0) + \\ &\quad C_2\alpha_s^2(L^2+a_1L+a_0) + \\ &\quad C_3\alpha_s^3(L^3+a_2L^2+a_1L+a_0) + ... \end{aligned} \tag{2.14}$$

where L is the large logarithmic factor showing up in the evolution equation [19]. The value of L depends on the process and the kinematic regions, for example,

$$\begin{array}{llll} (a)\ L = & \log Q^2 & at\ \ Q^2 \gg Q_0^2 & but\ \ x \sim 1 \\ (b)\ L = & \log Q^2 \log \frac{1}{x} & at\ \ Q^2 \gg Q_0^2 & and\ \ x \to 0 \\ (c)\ L = & \log \frac{1}{x} & at\ \ Q^2 \sim Q_0^2 & and\ \ x \to 0. \end{array} \tag{2.15}$$

The coefficients $C_n(Q_0^2)$ contain non-perturbative information and depend on the initial scale Q_0^2 of the evolution. Although the strong coupling constant α_s is small, we can not ignore the higher order terms because $\alpha_s \times L$ is not necessarily small. The first term of the right-handed side of Eq.(2.14) corresponds to the sum of those terms which contain the maximal power of logarithm L at each order of the perturbative expansion. If we consider only this leading term, it is called the Leading Log Approximation (LLA).

Figure 2.7 summarizes the characteristics of each logarithm on the evolution plane of the parton distribution of the proton. When the resolving power Q^2 of the probe increases at moderate x, it explores almost empty space or the asymptotic region of the parton distributions since the partons carrying large momentum fraction of the proton become rare. At small x with a moderate Q^2, however, the probe runs into crowded space of partons since the parton densities increase as x decreases. But the parton densities with decreasing x can not increase indefinitely due to the limited space of the proton. At some stage of x the partons start overlapping and the parton densities saturate as shown in Fig. 2.7. In case of small x and large Q^2 (see Eq.(2.15)(b)) both of large logarithms should be included in the parton evolution and the Double Leading Log Approximation (DLLA) is necessary. Two evolution equations, GLAP and BFKL, depending on the nature of the logarithms are summarized in the following [19] [4].

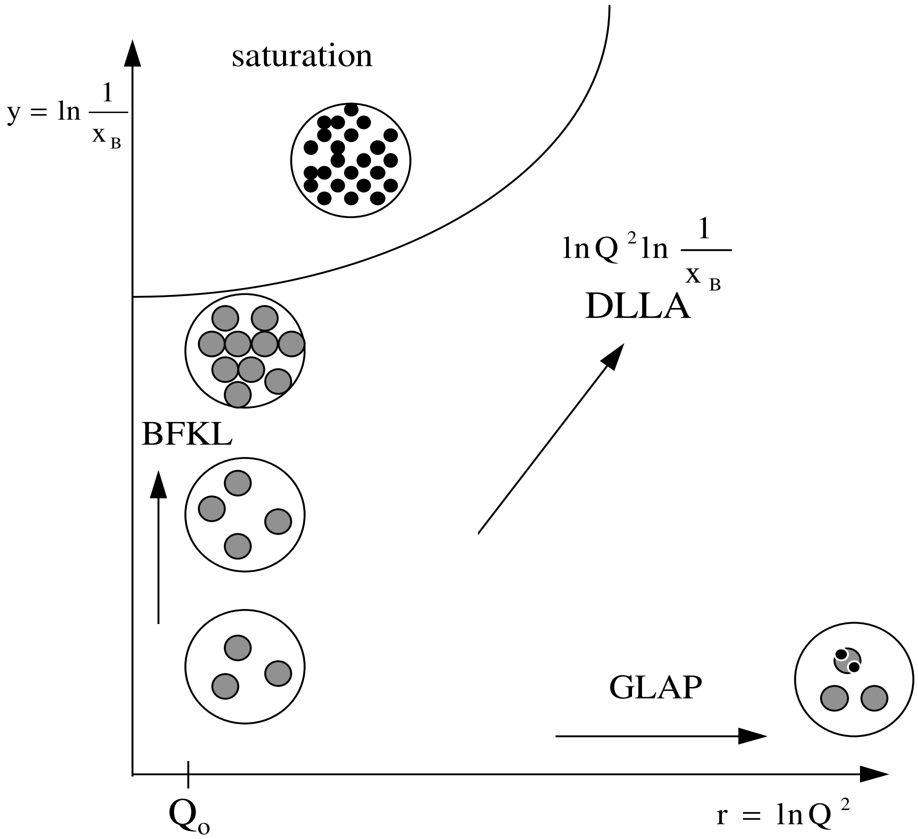

Figure 2.7: The Evolution of Parton Distributions

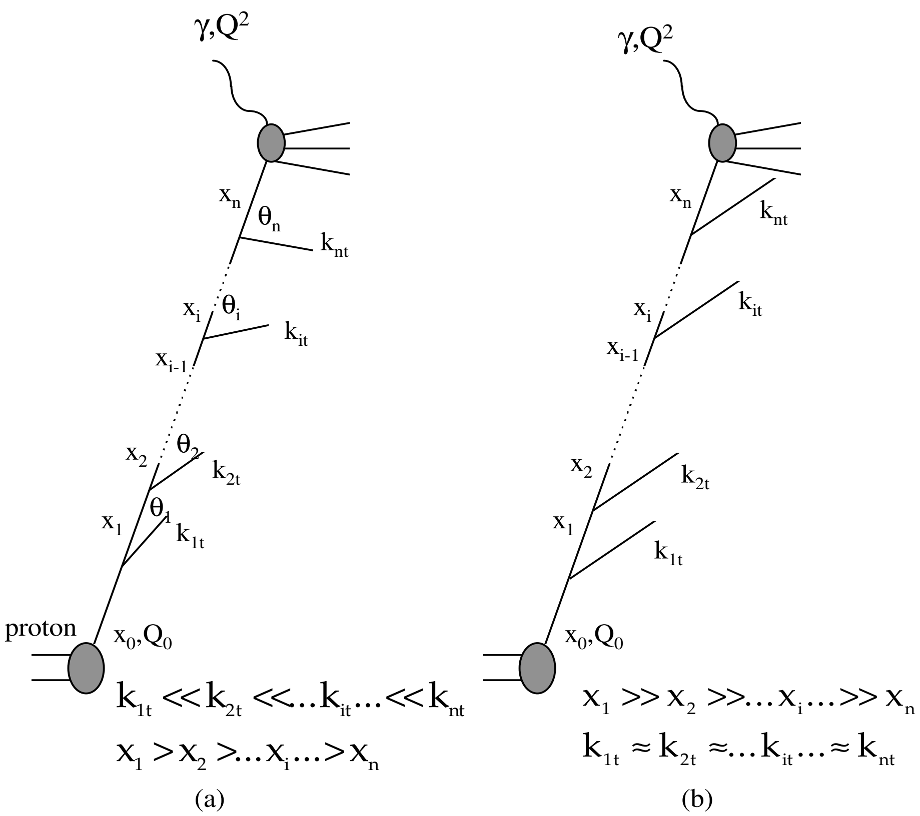

Figure 2.8: (a) GLAP and (b) BFKL evolutions ($\gamma^* q$ or $\gamma^* g$)

Gribov-Lipatov-Altarelli-Parisi **evolution**

The *Gribov-Lipatov-Altarelli-Parisi* (GLAP) equation describes the evolution of the parton density due to collinear singularities; $\log Q^2$ (see Eq.(2.15)(a)). In section 2.5.2, we have shown how to calculate the evolved parton densities with a previous parton density. It is clearly shown from Eq.(2.12) that there is large $\log Q^2$ contribution. The GLAP equation resums those contributions in the parton cascades by repeating the evolution of Eq.(2.12). The resummed evolution of the parton distribution is diagrammatically shown in Fig. 2.8(a) by repeating a single evolution similar to Fig. 2.6(c) from an initial parton state at x_0, Q_0.

The characteristics of GLAP evolution are summarized in Table 2.1. The dominant characteristic is the strong ordering in the transverse momenta of emitted partons and no strong ordering in the parton momentum fraction x. Only with such a condition does one get a $\log Q^2$ contribution for each integration over k_{it} in the parton cascade. This strong ordering means the GLAP evolution equation allows us to calculate the probability to find a parton of transverse size $r_t \approx \frac{1}{Q}$ inside the initial parton in the hadron at large x as shown in Fig. 2.7.

In the case where both Q^2 and $\frac{1}{x}$ are very large (see Eq.(2.15)(b)) the double leading–log approximation (DLLA) is required, and the resummed solution for the gluon density is given by

$$xg(x, Q^2) \sim a_0 \exp \sqrt{b_0 \log \frac{x_0}{x} \log \frac{\log \frac{Q^2}{\Lambda^2}}{\log \frac{Q_0^2}{\Lambda^2}}} \tag{2.16}$$

where Q_0 and x_0 are the initial scale of the parton cascade and $a_0(b_0)$ are constants. An example of GLAP evolution is shown in Fig. 2.9 using MRSD'$_-$ parton distributions. At moderate x the densities decrease as Q^2 increases. In other words at small x the densities increase as Q^2 increases.

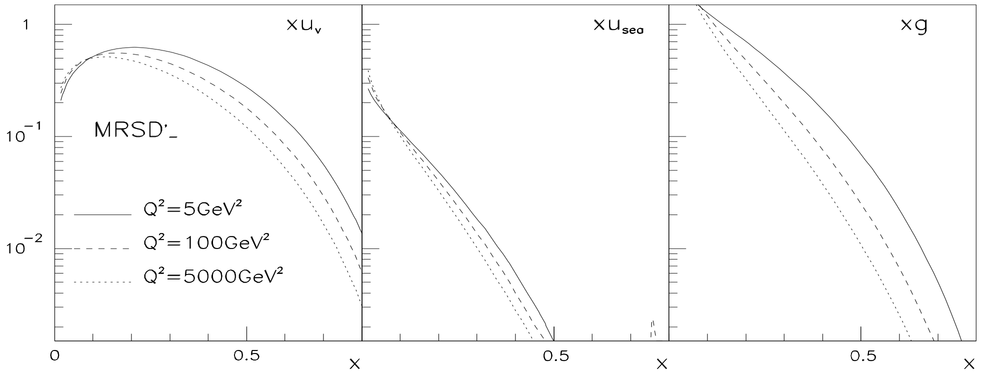

Figure 2.9: An example of GLAP evolution using MRSD'$_-$ structure function; u_v for *up valence* quark, u_{sea} for *up sea* quark, g for *gluon* as a function of momentum fraction x.

Balitski-Fadin-Kuraev-Lipatov evolution

In another extreme regime of fixed Q_0^2 and small x the behavior of the parton density may change abruptly. Here we will have the large logarithm, $L = \log \frac{1}{x}$, due to soft gluon radiation. The number of partons increases drastically in the region of small x because each parton in the branch of Fig.2.8(a) is allowed to decay into its own chain of daughters. Its simplified parton cascade process is shown in Fig.2.8(b).

The basic quantity in this approximation at small x is the unintegrated gluon distribution $f(x,k^2)$ which is related to the conventional scale dependent gluon distribution $g(x,Q^2)$ by [20]:

$$xg(x,Q^2) = \int_0^{Q^2} \frac{dk^2}{k^2} f(x,k^2) \tag{2.17}$$

In the LLA the unintegrated gluon distribution satisfies the following equation:

$$\frac{\partial f(x,k^2)}{\partial \log \frac{1}{x}} = \frac{3\alpha_s(k^2)}{\pi} k^2 \int_{k_0^2}^{\infty} \frac{dk'^2}{k'^2} [\frac{f(x,k'^2) - f(x,k^2)}{\mid k'^2 - k^2 \mid} + \frac{f(x,k^2)}{\sqrt{4k'^4 + k^4}}] \tag{2.18}$$

GLAP	BFKL
$\log Q^2$	$\log \frac{1}{x}$
$x_1 > x_2 ... > x_2 > ... > x_n = x$	$x_1 \gg x_2 ... \gg x_2 \gg ... \gg x_n = x$
$Q_0^2 \ll k_{1t}^2 ... \ll k_{it}^2 \ll ... \ll Q^2$	no k_t ordering

Table 2.1: Comparison of GLAP and BFKL evolution

which is called the *Balitski-Fadin-Kuraev-Lipatov* (BFKL) [4] equation. This equation resums the large leading $\log \frac{1}{x}$ contributions which arise from the sum of the gluon emission diagrams of the type shown in Fig.2.8(b). The logarithm in the denominator on the left-hand side indicates that the evolution is in $\log \frac{1}{x}$, not $\log Q^2$. This represents a strong ordering of the emitted gluons in x or rapidity, but with comparable momenta. The characteristics of these two evolutions are summarized in Table 2.1. The GLAP evolution related to large logarithms of Q^2 shows a strong ordering of emitted gluons in transverse momentum. On the other hand, the BFKL evolution of $\log \frac{1}{x}$ shows a strong ordering of emitted gluons in x.

2.5.4 Application of the GLAP Evolution

For high energy processes the most relevant range of x values is given by $x \sim Q/\sqrt{s}$ where Q is a typical momentum scale and $\sqrt{s}$ is the center-of-mass energy. At future high energy colliders where $\sqrt{s}$ will be still larger, many interesting physical processes taking place at moderate values of Q, e.g. 5-50 GeV, will probe parton distributions and interactions at very low values of x. In hadron-hadron interactions the production of minijets (jets with moderate p_t) is an example of such a process [21]. In oder to make precise prediction for such processes, the behavior of the parton distribution in this region must be understood.

To begin with it might be useful to perform a quantitative comparison between

HERA data and pQCD predictions in the parton distributions. For clarity we consider some of the next-to-leading order (NLO) parton density predictions that were available before HERA began operation. These parton densities are calculated by evolving an input distribution according to the GLAP equation at NLO. The input parton densities at scale Q_0^2 are fixed by fitting pre-HERA data [22]. Since pre-HERA data represent only the high-x region ($x > 10^{-2}$) the input gluon f_g and sea-quark distributions f_{sea} are unconstrained for x smaller than 10^{-2}, so the NLO predictions differ depending on the assumption of the input densities at small x.

GRV: The GRV parton distributions [23] are calculated by starting the evolution at very low input scale $Q_0^2 = 0.3$ GeV^2. At this scale the input distribution is assumed to vanish as $x \rightarrow 0$: $f_g(x) \sim x^2, f_{sea}(x) \sim x^{0.7}$. Because of this "valence-like" input, the steeper behavior at high Q^2 as shown in Fig. 2.5 is entirely generated by a very long Q^2 evolution (started at small input scale).

MRS: The MRS [24] analysis used the input scale $Q_0^2 = 4$ GeV^2, much higher than the one for GRV. They provided two representative sets of parton densities. Set D'$_0$ is obtained using flat input density at small x, $f_g(x) \sim f_{sea}(x) \sim const.$ Set D'$_-$ is calculated using very steep input $f_g(x) \sim f_{sea}(x) \sim x^{-0.5}$. The results are shown in Fig. 2.5.

CTEQ: The CTEQ collaboration [25] also starts the perturbative evolution at $Q_0^2 = 4$ GeV^2. CTEQ1MS, one of the sets they considered, has the the steepest input densities, $f_g(x) \sim x^{-0.38}\log(1/x)^{0.09}, f_{sea}(x) \sim x^{-0.27}$ and the result is compared with the others in Fig. 2.5.

The HERA data seem to be favored by the MRSD'$_-$ and GRV parton distributions. In the case of the MRS and CTEQ parton distributions calculated by the NLO Altarelli-Parisi perturbative evolution with the starting scale $Q_0^2 = 4$ GeV^2 the differences for F_2 at small x are entirely due to the different input densities. The input density $x^{-0.5}$ for MRSD'$_-$ was motivated by the BFKL formalism [22] [26] although its evolution followed the AP equation.

Since HERA started operation in 1990, the data at $10^{-4} < x < 10^{-2}$ produced new parton distribution functions(PDF's), e.g. CTEQ2M set, CTEQ3M set, MRSA set [26, 27]. Furthermore the steep increase of F_2 at small $x \leq 10^{-2}$ caused much debate as to whether it results from conventional GLAP evolution of the parton density or whether it is from a new regime where the dynamics is described by the BFKL evolution equation. As mentioned above the latter QCD evolution equation is expected to be suitable for the study of the small x region since it resums all leading $\log(1/x)$ terms in the perturbative expansion. As shown in Fig. 2.5 the measured proton structure function F_2 is well described by the GLAP evolution equation. A hybrid fit using the BFKL equation for the evolution of the increasing gluon density at small x and the GLAP equation elsewhere is also attempted and is found to describe the data equally well [26, 28]. On the other hand one tries to get the unified evolution equation carrying both characteristics [29].

2.5.5 Application of the BFKL Evolution

Precision tests of perturbative QCD and searches for new physics within or beyond the standard model have been performed at hadron colliders. The recent development of next-to-leading-order (NLO) predictions for high p_t jet production [30, 31, 32] is a milestone in the progress of pQCD, and compared favorable with experimental data [1] [2] [33]. Along with these advances in pQCD at large p_t scale, the higher energy colliders such as the Fermilab Tevatron($p\bar{p}$) and HERA(ep) opened up a new era of pQCD including diffractive physics [34], rapidity gap physics [35] and small-x physics (hadron structure functions at small x) [22].

Many of attempts to understand these new processes are based on "Pomeron" exchange [19] (The Pomeron was named after a Russian physicist Pomeranchuk who

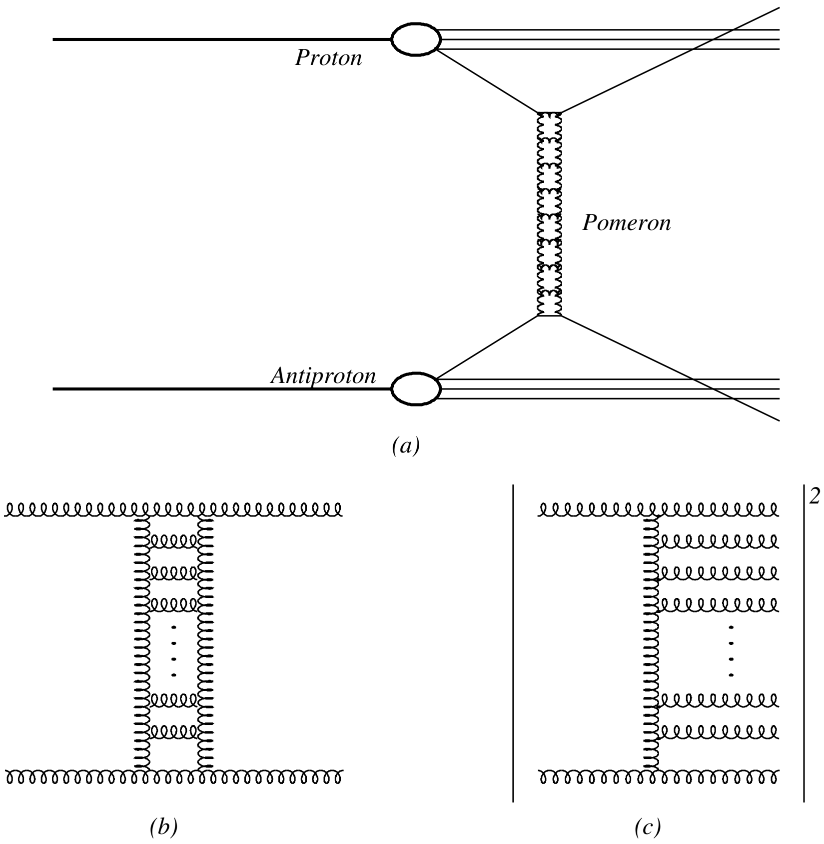

Figure 2.10: (a) Pomeron exchange in double diffractive $p\bar{p}$ scattering, (b) Feynman Ladder diagram for colorless two gluon exchange, Pomeron, (c) Scattering amplitude for t channel jet production. The scattering amplitude (c) is the same as (b).

did pioneering work on the subjects). The concept of the Pomeron has been developed within the framework of Regge theory [36]. In the early 1960s, Regge theory described the energy dependence of hadronic total cross sections. The total cross section which first decreased with increasing center of mass energy $\sqrt{s}$ started rising, which requires the existence of a phenomenological objet, or Pomeron, mediating elastic scattering [37]. As with mesons in the Regge trajectory [37] the Pomeron has vacuum quantum numbers. This describes elastic or diffractive scattering which does not change the quantum numbers of the proton or antiproton. It is a colorless object (color singlet). In several perturbative models [38, 4] the Pomeron is pictured as a colorless two-gluon bound state shown in Fig. 2.10(a,b).

In the limit of large partonic center of mass energy $\sqrt{\hat{s}}$ and fixed momentum transfer Q, the scattering amplitude for rapidity gap production can be calculated using a BFKL model [4] which resums the leading logarithms $(\log(\hat{s}/Q))$ to all orders in α_s [39]. Since it is hard to observe the distinctive feature of the Pomeron experimentally Mueller and Navelet proposed [21] measuring the two-jet inclusive cross section as a function of the rapidity interval between two tagging jets. Since the scattering amplitude of the dijet inclusive cross section contains the same Feynman diagram of the Pomeron as described in Fig. 2.10 BFKL formalism can be applied to Mueller and Navelet's dijet production. We shall discuss the phenomenology of dijet production in detail.

Chapter 3

Dijet Production

3.1 Kinematics

At hadron-hadron colliders, most commonly chosen coordinates are: rapidity y, transverse momentum p_t, and azimuthal angle ϕ, since they satisfy simple transformation under the Lorentz boost. For example, the Lorentz Invariant Phase Space (LIPS) is

$$\begin{aligned} d\mathbf{LIPS} \equiv \frac{d^3p}{E} &= \frac{dp_x dp_y dp_z}{E} \\ &= \frac{p^2 dp d\phi d(\cos\theta)}{E} \\ &= \frac{p_t dp_t dy d\phi}{E} \end{aligned} \tag{3.1}$$

where (E, p_x, p_y, p_z) is the 4-momentum of a particle. Rapidity is defined by

$$y \equiv \frac{1}{2}\log_e \frac{E+p_z}{E-p_z}. \tag{3.2}$$

A boost along the z direction changes the rapidity y by

$$y \rightarrow y + y_{boost} \tag{3.3}$$

where y_{boost} is a constant. Transverse momentum p_t and azimuthal angle ϕ are invariant under longitudinal Lorentz boost. Therefore, the last equation of Eq.(3.1) has a simple transformation under the boost.

In a detector which measures only energy it is often difficult to determine the true rapidity of a particle or a jet. So we define the "pseudo-rapidity" η as the rapidity of a particle or a jet with zero mass as follows.

$$\eta \equiv \frac{1}{2}\log_e \frac{1+\cos\theta}{1-\cos\theta} = -\log_e \tan\frac{\theta}{2} \tag{3.4}$$

Rapidity and pseudorapidity are almost equal to each other. So one can use η in place of y for most calculations [40].

3.2 The definition of a Jet

When hard scattering does occur in hadron-hadron collision the final state is most often characterized by collimated sprays of large p_t hadrons or jets. At lowest order a jet is a single parton, a quark or gluon, that is isolated in momentum space just after scattering and its perturbative description is unambiguous since the partons are well separated. However, the experimental situation is not as simple due to all orders of emission and the remnants of the partons in the detector [41].

Figure 3.1 shows how partons, quarks or gluons, are associated with the final state hadrons or the signals measured in a detector. A jet in a calorimeter is seen as a localized peak of hadronic energy in a small group of adjacent calorimeter cells. This calorimeter jet is expected to be matched with a parton originating from the hard scattering. In reality, however, we are confronted with several ambiguities. First, when one imagines a hard scattering having three partons in the final state and two of the three partons are near each other the final state could be a two jet event or a three jet event depending on the distance between the two partons and the resolution of the detector. This ambiguity also appears in theoretical calculations at $O(\alpha_s^3)$ when a parton is very soft or two partons are very near to each other.

Hard Scattering

$\downarrow$

Hard partons

$\downarrow$ $\leftarrow$ parton showering

Soft partons

$\downarrow$ $\leftarrow$ hadronization

Hadrons

$\downarrow$ $\leftarrow$ shower in calorimeter

Calorimeter Signal

Figure 3.1: Evolution of a jet

Second, partons are connected by color strings and thus a single parton does not evolve into an isolated jet of hadrons. That is, the fragmentation process involves the collective action of several partons. Hence, except for large p_t hadrons, there can be no unique experimental definition of which hadrons are to be associated with which jet. Therefore we could say that a jet is not well defined or a jet can be defined in many different ways which hinders the direct comparison of jet cross sections in hadron collisions due to the difference in jet definition adopted by various experiments [42].

At the 1990 Snowmass Workshop, a standardized jet definition was adopted based on a cone definition of jets and specified the main features of the algorithm [43]. In the definition we want to maintain the invariance appropriate for hadron colliders under azimuthal rotations and longitudinal Lorentz boost. Thus particles are described by their transverse momentum p_t, azimuthal angles ϕ and rapidities η. The main feature of the cone definition is that a jet consists of particles (cells in a calorimeter) whose momentum vectors lie in a cone in $\eta \times \phi$ space. The cone consists of a circle of radius $R = \sqrt{(\Delta\phi)^2 + (\Delta\eta)^2}$ and the standard radius is 0.7 which is large enough to contain most of the energy of a jet. This definition is quite simple and natural. However, when two jet cones overlap, a further specification for the merging and splitting of jets is to be required. This will be discussed later for the DØ jet definition.

3.3 Dijet production with BFKL

Perturbative QCD calculations of jet production rates in hadron-hadron collisions involve several different scales, Λ_{QCD}, the center of mass energy $\sqrt{s}$, the center of mass energy of the hard process $\sqrt{\hat{s}}$ and the momentum transfer Q which is of the order of the transverse momentum of jets in the hard scattering. The conventional approach to these calculations is to work at fixed order in the coupling constant α_s, assuming that $\sqrt{s}$, $\sqrt{\hat{s}}$ and Q are of comparable size, so that there are no large logarithms involved. The results up to next-to-leading order (NLO) [31, 32] are quite successful in the description of one or two jet inclusive distributions from hadron-hadron colliders [33].

As the energy of hadron-hadron colliders (the Fermilab Tevatron or future hadron colliders) increases, the detection of hard processes involving partons of small momentum fractions of their parent hadrons will be possible. There may then be some kinematic regions where one cannot ignore the large ratio of these kinematic scales. In the semi-hard region defined as $\Lambda_{QCD}^2 \ll Q^2 \ll s$ the calculation of jet cross sections would be characterized by the large logarithms of the kinematic scales. If $\sqrt{\hat{s}} = \sqrt{x_A x_B s}$ is the center of mass energy of the hard process the large logarithm in the semi-hard region can be written as follows.

$$\log\frac{s}{Q^2} = \log\frac{1}{x_A} + \log\frac{\hat{s}}{Q^2} + \log\frac{1}{x_B}. \tag{3.5}$$

Following the factorization theorem the logarithms $\log\frac{1}{x}$ appear in the evolution of the parton densities and $\log\frac{\hat{s}}{Q^2}$ parameterizes in the hard process $\hat{\sigma}$. Jet production in the semi-hard region carries large logarithmic terms which must be resummed either in the parton structure function or in the partonic cross section.

If no restrictions are made on $\sqrt{\hat{s}} = \sqrt{x_A x_B s}$ jet or dijet production in the semi-hard region can be represented as a convolution of the parton structure function at small x and the hard process cross section. As mentioned in section 2.4 the higher parton density at small x contributes to an increase of the cross section. In this case it is rather difficult to separate the hard process and the parton density contribution to the cross section. Furthermore, if BFKL evolution is important the parton structure function itself at small x requires more sophisticated analysis than in the usual GLAP evolution. With the experimental uncertainty in the structure function at small x it is not easy to make predictions in this kinematic region.

One way to minimize the complexity of the calculations is to restrict the kinematic range of the process. In the case of dijet production, if the transverse momenta of the two tagging jets at the *extremes of the rapidity interval* are required to be larger than some cutoff $p_{\perp min}$ the parton momentum fractions, x_A, x_B, are large enough so that there are no large logarithm, $\log 1/x$, in the evolution of the parton distribution. Thus the parton densities evolve according to the usual GLAP equation.

However, large logarithms ($\log Q^2$) still remain in the partonic cross section and we need to resum them as we did for the evolution of the structure function. As it will be shown in the next section this logarithm is the size of the rapidity interval. To investigate the large logarithm effect Mueller and Navelet proposed [21] to measure two-jet inclusive cross section and measure the growth of the cross section as the rapidity interval between the tagging jets grows with the center of mass energy. To deal with the large logarithms, they used the BFKL [4] theory which resums the leading logarithms by using a multigluon amplitude with gluons uniformly filling the rapidity interval between the tagging jets as shown in Fig. 3.2. This study has been extended by Stirling [44], Del Duca and Schmidt [45] independently.

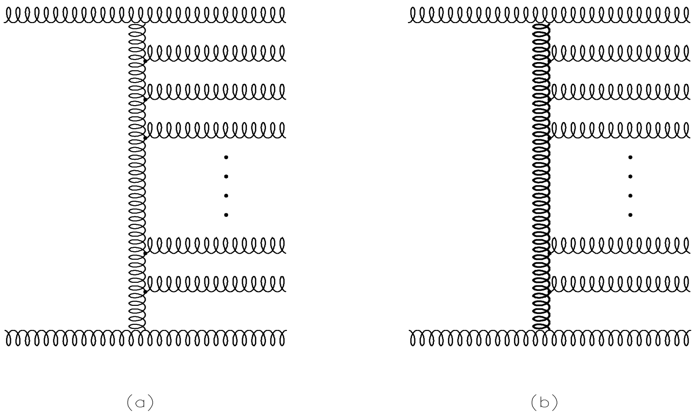

Figure 3.2: Multigluon amplitude a) at tree level b) with the virtual radiative corrections, represented by the thicker gluon line.

3.3.1 Dijet inclusive cross section

We are now ready to calculate the dijet-inclusive process $p\bar{p} \to 2jets + X$ in the semi-hard regime defined by $\hat{s} \gg Q^2$. A typical momentum scale is $Q^2(\approx p_{1\perp}p_{2\perp})$ in the event. If we tag two jets with large rapidity interval $\Delta\eta = \eta_1 - \eta_2$, we have the following relations using $x \approx (p_\perp/\sqrt{s})e^{\pm\eta}$ at large rapidity, η.

$$\begin{aligned}\Delta\eta = \eta_1 - \eta_2 &\approx \log\frac{x_1\sqrt{s}}{p_{1\perp}} + \log\frac{x_2\sqrt{s}}{p_{2\perp}} \\ &= \log\frac{x_1 x_2 s}{p_{1\perp}p_{2\perp}} \\ &\approx \log\frac{\hat{s}}{Q^2} \qquad (3.6)\end{aligned}$$

where $Q^2 \approx p_{1\perp}p_{2\perp}$ and $\hat{s} = x_1 x_2 s$. Other relevant parameters are the relative azimuthal angle $\Delta\phi$ and the rapidity boost $\overline{\eta} = (\eta_1 + \eta_2)/2$ of the two jets. In the semi-hard and large $\Delta\eta$ regime we can write the cross section at fixed x;

$$\frac{d\sigma}{dp_{1\perp}^2 dp_{2\perp}^2 d\Delta\phi d\Delta\eta d\overline{\eta}} = \sum_{ij} x_1 x_2 f_{i/A}(x_1,\mu^2) f_{j/B}(x_2,\mu^2) \frac{d\hat{\sigma}_{ij}}{dp_{1\perp}^2 dp_{2\perp}^2 d\Delta\phi} \tag{3.7}$$

where $f_{i(j)}$ is the parton distribution function of flavor $i(j) = q, \overline{q}$ and g inside the initial hadron A(B). The partonic cross section $\frac{d\hat{\sigma}_{ij}}{dp_{1\perp}^2 dp_{2\perp}^2 d\Delta\phi}$ contains the information about the hard scattering. and is separated from the parton distribution functions by the factorization theorem.

Born Level Cross section

At the Born level, only two partonic jets are produced back-to-back and the cross section is,

$$\frac{d\hat{\sigma}_{ij}}{dp_{1\perp}^2 dp_{2\perp}^2 d\Delta\phi} \to \frac{d\hat{\sigma}_{ij}}{d\hat{t}} \delta(p_{1\perp}^2 - p_{2\perp}^2)\delta(\Delta\phi - \pi) \tag{3.8}$$

where

$$\begin{aligned}
p_\perp &= p_{1\perp} = p_{2\perp} \\
\Delta\eta &= \eta_1 - \eta_2 \ \ (\eta_1 > \eta_2) \\
x_1 &= \frac{p_\perp e^{\eta_1} + p_\perp e^{-\eta_2}}{\sqrt{s}} = \frac{2p_\perp e^{\overline{\eta}}}{\sqrt{s}} \cosh(\frac{\Delta\eta}{2}) \\
x_2 &= \frac{p_\perp e^{-\eta_1} + p_\perp e^{\eta_2}}{\sqrt{s}} = \frac{2p_\perp e^{-\overline{\eta}}}{\sqrt{s}} \cosh(\frac{\Delta\eta}{2}) \\
\hat{s} &= x_1 x_2 s = 2p_\perp^2(1 + \cosh(\Delta\eta)) \\
\hat{t} &= -p_\perp^2(1 + e^{-\Delta\eta}) \\
\hat{u} &= -p_\perp^2(1 + e^{\Delta\eta}).
\end{aligned} \tag{3.9}$$

The Mandelstam variables $\hat{s}, \hat{t}, \hat{u}$ do not depend on the rapidity boost $\overline{\eta}$. The lowest order parton cross sections are well known and can be found in reference [46].

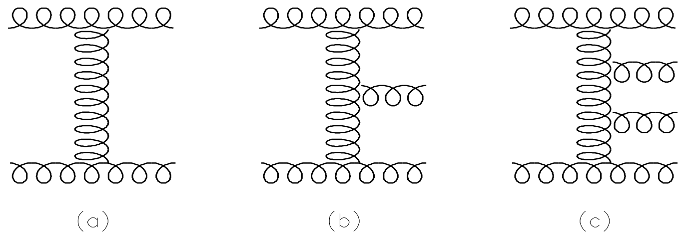

Figure 3.3: Feynman diagrams for a) $gg \to gg, O(\alpha_s^2)$ b) $gg \to ggg, O(\alpha_s^3)$ c) $gg \to gggg, O(\alpha_s^4)$.

Born Level Cross section at Large $\Delta\eta$

We shall now approximate the lowest order cross section for large $\Delta\eta$. At large $\Delta\eta$, the lowest order amplitude is dominated by the gluon exchange, t-channel diagrams, $gg \to gg, qg \to qg, qq \to qq$. Figure 3.3(a) shows the leading order $gg \to gg$ process. The hard cross section for $gg \to gg$ is given by

$$\frac{d\hat{\sigma}_{gg}}{d\hat{t}} = \frac{\pi C_A^2 \alpha_s^2}{2p_\perp^4} \tag{3.10}$$

with the Casimir operator $C_A = N_c = 3$. Similarly we find

$$\frac{d\hat{\sigma}_{qq}}{d\hat{t}} = \frac{C_F}{C_A}\frac{d\hat{\sigma}_{qg}}{d\hat{t}} = \frac{C_F^2}{C_A^2}\frac{d\hat{\sigma}_{gg}}{d\hat{t}} \tag{3.11}$$

with the Casimir operator $C_F = 4/3$. Thus it is possible to consider only $gg \to gg$ and put the other subprocesses into the effective parton distribution density[47],

$$f_{eff}(x,\mu^2) = G(x,\mu^2) + \frac{C_F}{C_A}\sum_f [Q_f(x,\mu^2) + \overline{Q_f}(x,\mu^2)] \tag{3.12}$$

where the sum is over quark flavors. Then the cross section (3.7) can be rewritten as follows.

$$\frac{d\sigma}{dp_{1\perp}^2 dp_{2\perp}^2 d\Delta\phi d\Delta\eta d\overline{\eta}} = x_1 x_2 f_{eff}(x_1,\mu^2) f_{eff}(x_2,\mu^2) \frac{d\hat{\sigma}_{gg}}{dp_{1\perp}^2 dp_{2\perp}^2 d\Delta\phi} \tag{3.13}$$

where only the $gg \to gg$ process is factorized into the partonic cross section.

Minijet corrected cross section

Figure 3.2 shows a hard process with multiple parton emission. As mentioned above, this process in the semihard region involves a large logarithmic term $\log \hat{s}/Q^2$. The BFKL theory systematically resums the leading logarithmic term $\log \hat{s}/Q^2$ by using multigluon amplitude where the rapidity interval between the tagging jets is filled with gluons, strongly ordered in rapidity. The approximate cross section is

$$\begin{aligned} \frac{d\hat{\sigma}_{gg}}{dp_{1\perp}^2 dp_{2\perp}^2 d\Delta\phi} &= \frac{C_A^2 \alpha_s^2}{8 p_{1\perp}^3 p_{2\perp}^3} \frac{e^{A\Delta\eta}}{\sqrt{B\pi\Delta\eta}} e^{-\frac{\log^2(p_{1\perp}^2/p_{2\perp}^2)}{4B\Delta\eta}} \\ &\propto e^{A\Delta\eta} \end{aligned} \tag{3.14}$$

where A, B are constants. The exponential growth of the cross section with the rapidity interval $\Delta\eta$ is due to the production of the minijets.

3.3.2 The Results

We examine the effect of soft gluon radiation between two tagging jets at the Tevatron with center of mass energy $\sqrt{s} = 1.8$ TeV. With a minimum transverse momentum the rapidity boost $\overline{\eta}$ is chosen to be zero, such that neither x_i in Eq.(3.9) can become small. We also name the leading jet in rapidity jet 1 and the last jet jet 2.

From Eq.(3.14) the exponential growth of partonic cross section as a function of rapidity interval must be an observable signal for enhanced soft radiation between the two jets. However, the minijet cross section does not show any great increase at large rapidity since the cross section is a convolution of the partonic cross section and the parton structure function. The parton structure function $f(x, \mu^2)$ decreases as rapidity increases and confronts a cutoff since the parton momentum fraction

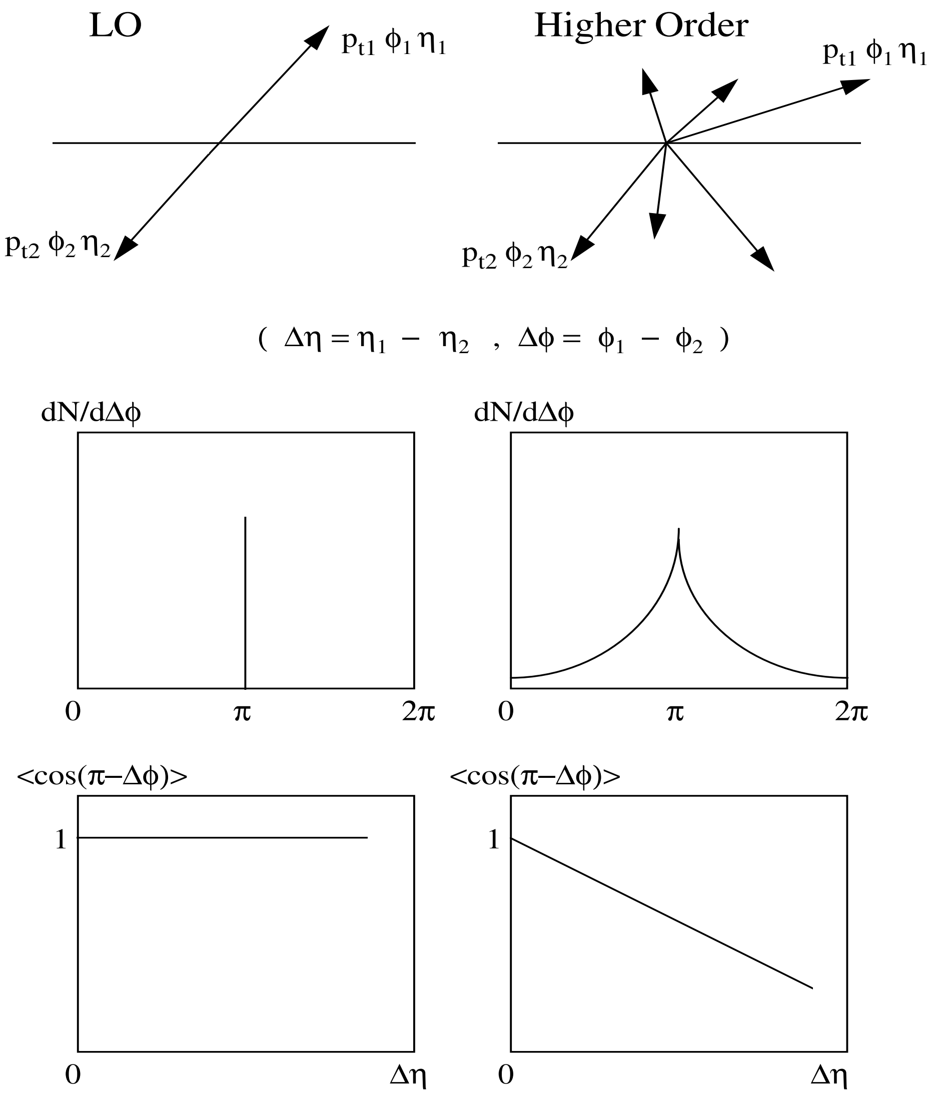

Figure 3.4: A comparison between leading order and higher order effect in $\Delta\phi$ and $< \cos(\pi - \Delta\phi) >$ distributions.

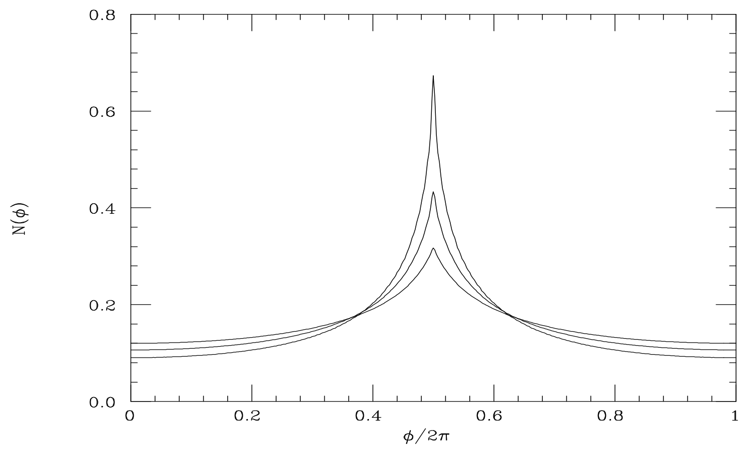

Figure 3.5: From top to bottom, relative to the peak, the solid lines are the normalized $\Delta\phi$ distributions at $\Delta\eta = 5$, 6 and 7. (Here, $\phi = \Delta\phi$)

$x \approx (p_\perp^{min}/\sqrt{s})e^{\pm\eta}$ is a function of rapidity with fixed $p_\perp^{min}$ and $\sqrt{s}$, and should be less than one.

Thus, at the Tevatron energy we must look elsewhere for the effects of enhanced radiation. As indicated in Eq.(3.8) the decrease of transverse momentum (p_t) or azimuthal angle (ϕ) correlation as rapidity interval increases must be sufficient to show the effect of enhanced radiation. Since the momentum resolution is not good enough to study the transverse momentum correlation we have studied the azimuthal angle correlation between the two jets with the largest rapidity separation.

As shown in Fig. 3.4 we expect the p_t and ϕ correlations between two jets decrease as more jets are involved in a partonic subprocess. At LO two jets are back-to-back in $x \times y$ plane and a sharp peak is expected at π in the number of events vs. $\Delta\phi$ plot. At higher order, however, two jets are not in back-to-back correlation and a wide $\Delta\phi$ distribution is expected. In order to express these correlation effects quantitatively we have used $\cos(\pi - \Delta\phi)$, and calculate its average as a function of $\Delta\eta$. At LO the average of $\cos(\pi - \Delta\phi)$ would be one. At higher order the average value would decrease as the number of jets in the partonic subprocess increases.

For example, Figure 3.5 shows the distribution of $\Delta\phi$ calculated by Del Duca and Schmidt using BFKL resummation with $\bar{\eta} = 0$ and $p_t^{min} = 20$ GeV [45]. The solid lines are the normalized $\Delta\phi$ distributions at $\Delta\eta = 5$, 6 and 7. The decreasing peaks represent the decrease of correlation between the two jets as the rapidity interval increases.

Chapter 4

The DØ Detector

The DØ detector was constructed to study proton-antiproton collisions at $\sqrt{s} =$ 1.8 TeV in the Fermilab Tevatron collider [5]. Since the Tevatron collider provides the highest beam energy in the world, the prime physics goal of the DØ experiment is new particle searches, e.g. the study of the high mass states and large p_t physics. These include the search for the top quark, precision tests of W and Z bosons to test the standard model, perturbative QCD, production of b-quark hadrons and searches for new phenomena beyond the standard model.

4.1 Detector Overview

The DØ detector consists of three major sub-systems: the central detector, the calorimeter and the muon system, as shown in Fig. 4.1. The detector design was optimized to produce 1) excellent identification and measurement of electrons and muons, 2) good measurement of jets at large p_t through finely segmented calorimetry with excellent energy resolution, 3) and a well-controlled measurement of missing transverse energy ($\not{E}_T$) to identify neutrinos and other non-interacting particles. A right-handed coordinate system is adopted with the z-axis along the proton direction and the y-axis upward. The angles ϕ and θ are the azimuthal and polar angles (θ=0

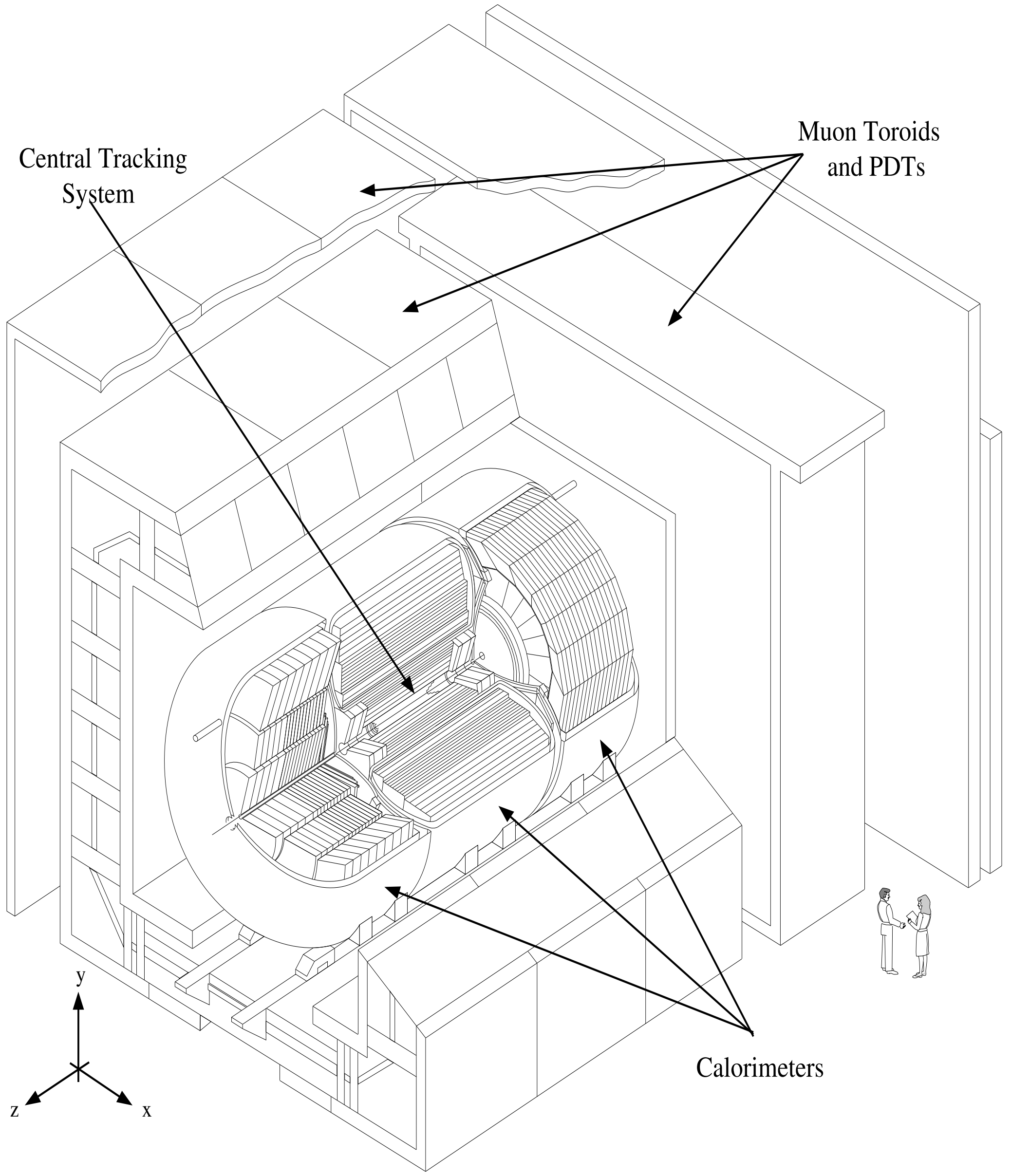

Figure 4.1: The DØ Detector

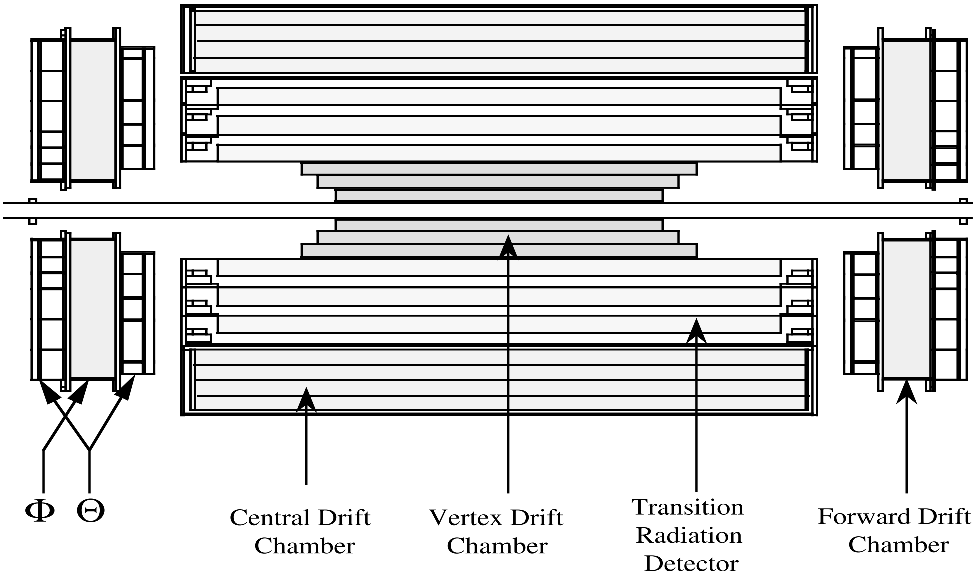

Figure 4.2: The DØ tracking system

along z-axis) respectively. The r-coordinate indicates the perpendicular distance from the beam axis.

4.2 The Central Detector

The central detector (CD) is a non-magnetic tracking system and consists of the vertex drift chamber (VTX), the transition radiation detector (TRD), the central drift chamber(CDC) and two forward drift chambers (FDC) as shown in Fig. 4.2. The VTX, TRD and CDC are concentric with the beam pipe and cover a large angular region. The FDCs are oriented perpendicular to the beam axis. All central detectors are located within the boundary, r=78 cm and z =$\pm$135 cm, which is restricted by the inner radius of the calorimeter.

A momentum measurement of charged particles is not possible due to the absence of the magnetic field. Therefore, the prime considerations for tracking are good two-track resolving power and high tracking efficiency. Good ionization energy measurement is required in order to distinguish single electrons from converted pairs. In order to obtain good z resolution in the large angle chambers, different measurement methods are used for each sub-system. They utilize charge division (VTX), helical cathode pads (TRD) and delay lines (CDC) [48]. The tracking system can determine the primary z-vertex to within 1 cm. The characteristics of each sub-system are described below and summarized in Table 4.1.

The Vertex Detector

The VTX chamber is the innermost tracking detector which has an inner radius of 3.7 cm and an outer active radius of 16.2 cm. It consists of three independent concentric layers of cells mounted on carbon fiber tubes. The innermost layer has 16 cells in azimuth; the outer two layers have 32 cells. The sense wires provide a measurement of the z-coordinate from readout at both ends. The electrostatic properties of the cell are determined by the grounded planes of grid-wire, sense wire planes and the cathode field wire planes. To obtain good spatial resolution and track pair resolving power, a gas mixture of CO_2(95%)-ethane(5%), at 1 atm with a small admixture of H_2O was chosen. Test beam results under normal DØ operating conditions showed good drift time-distance correlation with an average drift velocity of 7.3 μm/ns at $< E > \approx 1$ kV/cm [5].

The Transition Radiation Detector

The TRD is located between the VTX and the CDC, and provides independent electron/pion separation in addition to that given by the calorimeter. Transition radiation x-rays are produced when highly relativistic charged particles ($\gamma > 10^3$) traverse boundaries between media with different dielectric constants [49]. The energies of radiated x-rays depend on the mass of a charged particle since the velocities of particles in media depend on its mass. The TRD consists of three separated units, each containing a radiator and an x-ray detection chamber. The energy spectrum of

VTX	Sense wire resolution	60 μm
	Charge division resolution	1 cm
	Pair resolution	0.7 mm
TRD	e/π discrimination	
	at 90% efficiency	50:1
CDC	Sense wire resolution	200 μm
	Delay line resolution	2 mm
	Pair resolution	2 mm
FDC	Sense wire resolution	200 μm
	Delay line resolution	4mm(Θ), 20mm(Φ module)
	Pair resolution	2 mm

Table 4.1: Characteristics of the Central Detector

the x-rays, determined by the thickness of the radiator foils and the gaps between the foils, peaks at 8 KeV and is mainly contained below 30 KeV. A two-stage proportional wire chamber (PWC) is mounted just after the radiator for the detection of x-rays. The x-rays convert mainly in the first stage of the chamber and the resulting charge drifts radially outward to the sense wires. The average collected charges for 5 GeV electrons and pions in a test beam showed good separation between electrons and pions as a function of arrival time [5].

The Central Drift Chamber

The CDC is located just after the TRD and just before the inner cylinder of the calorimeter. It consists of four concentric layers of drift chambers and each layer has 32 azimuthal cells. Each cell contains seven sense wires with its readout on one end and two delay lines with their readout on both ends. The delay lines propagate the signals induced from the nearest neighboring anode wire; the difference of the arrival times at both ends provides the z-coordinate of the track. The CDC is operated with $Ar(92.5\%)CH_4(4\%)CO_2(3\%)$ gas with 0.5% H_2O. With a drift field of 620 V/cm, the drift velocity is about 34 μm/ns.

The Forward Drift Chambers

The FDCs extend the tracking coverage out to $|\eta_d| \approx 3$ (η_d represents detector η, calculated by drawing a ray from z =0). They are positioned at both ends of the concentric barrels of the VTX, TRD and CDC as shown in Fig. 4.2. Each FDC consists of three separate chambers, Φ module and two Θ modules, which provide the ϕ and θ-coordinates depending on the directions of their sense wires. Resolutions are listed in Table 4.1.

4.3 The Calorimeter

The DØ calorimeter is a sampling calorimeter using liquid argon and depleted uranium as active and passive materials, respectively. It consists of three cryostat systems, a central calorimeter (CC) and two end-cap calorimeters (EC), as shown in Fig. 4.3. Since there is no central magnetic field the DØ calorimeter plays important roles in the identification of high p_t objects, electrons, photons, jets and muons, and providing the missing transverse energy using transverse energy balance in an event.

Each cryostat calorimeter consists of three distinct types of calorimeter modules: an electromagnetic section (EM) with relatively thin uranium absorber plates, a fine hadronic section (FH) with thicker uranium plates and a coarse hadronic section (CH) with thick copper (CC) or stainless plates (EC). These calorimeter modules have **Projective Tower Structure** with **Fine Segmentation**, 0.1×0.1 in $\eta \times \phi$ space, as shown in Fig. 4.4. There are 72×64 towers in $\eta \times \phi$ space which cover the pseudorapidity region up to $|\eta_d| \leq 4.5$. Only hadronic modules cover the region

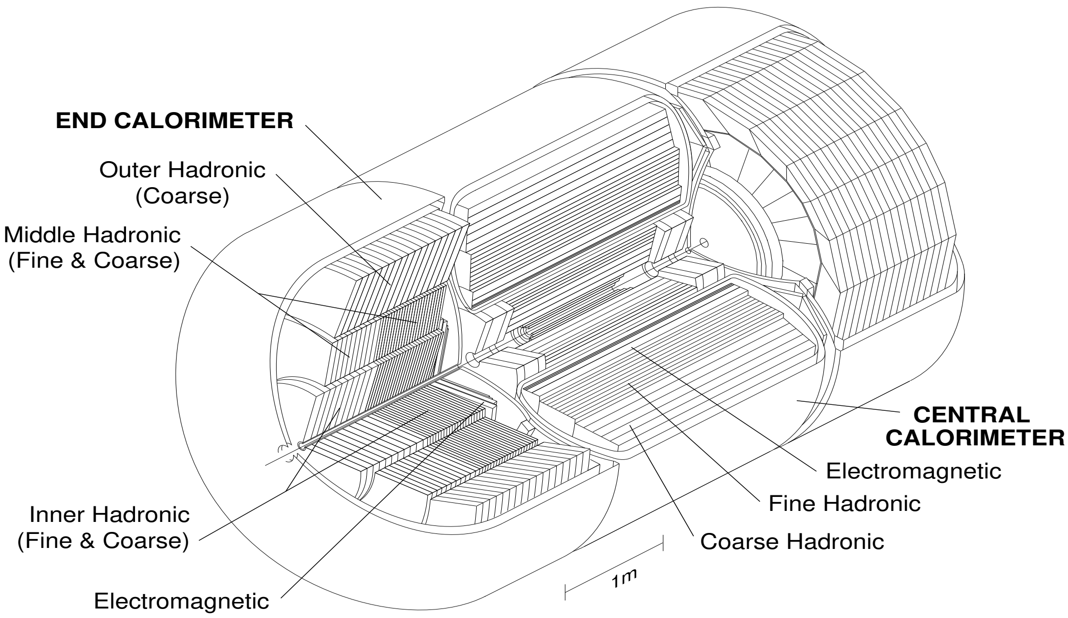

Figure 4.3: The DØ Calorimeter

for $4.1 \leq |\eta_d| \leq 4.5$ due to the restricted space.

The transverse size of the cells, $\Delta\eta \times \Delta\phi = 0.1 \times 0.1$, was chosen to be comparable to the transverse size of showers: $\sim$ 1-2 cm for EM showers and $\sim$ 10 cm for hadronic showers. This fine segmentation provides the opportunity to study the jet shape since the typical transverse size of jets is much bigger. Longitudinal subdivisions within EM, FH and CH are also useful since the longitudinal shower profiles help distinguish electrons and hadrons. These three types of calorimeter modules have the following characteristics.

- **Electromagnetic Section (EM)**: The EM section is the innermost structure of the calorimeter and located just outside the tracking system. It consists of nearly pure depleted uranium plates of 3-4 mm thickness. As shown in Fig. 4.5, there are four separate layers with 2, 2, 7 and 10 radiation lengths (X_0) in thickness respectively. The first two layers provide the longitudinal shower profile near the beginning of the showers in which photons and pions differ

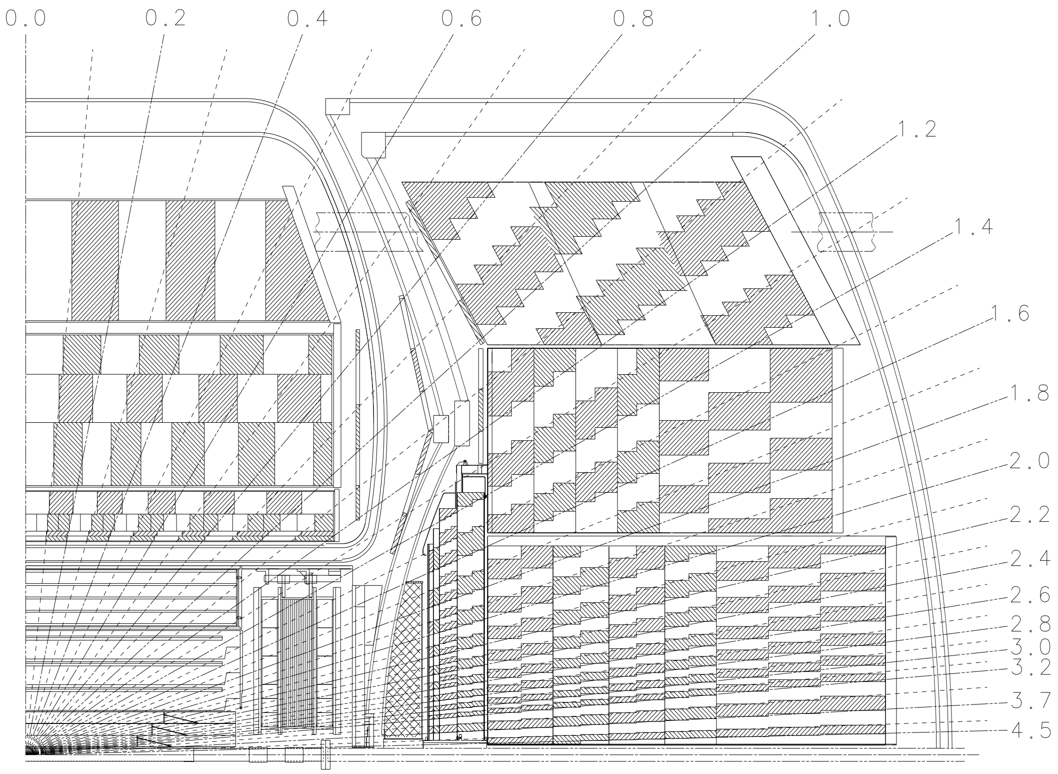

Figure 4.4: A cross section of the calorimeter

statistically. The third layer has smaller transverse size, $\Delta\eta \times \Delta\phi = 0.05 \times 0.05$, and spans the EM shower maximum region. This gives a better measure of an EM shower centroid. The fourth layer ($X_0 = 10$) is thick enough to contain all the EM shower energy penetrating the first three layers.

- **Fine Hadronic Section (FH)**: The FH section is located outside the EM section and inside the CH section and has three or four longitudinal layers with 1.3, 1.0 and 0.9 interaction lengths (λ_I) in thickness as shown in Fig. 4.5. This section is made of 6 mm thick uranium-niobium (2%) alloy, and the transverse segmentation is 0.1×0.1 in $\Delta\eta \times \Delta\phi$. The FH modules were designed to contain most of the energy deposited by an hadronic shower.

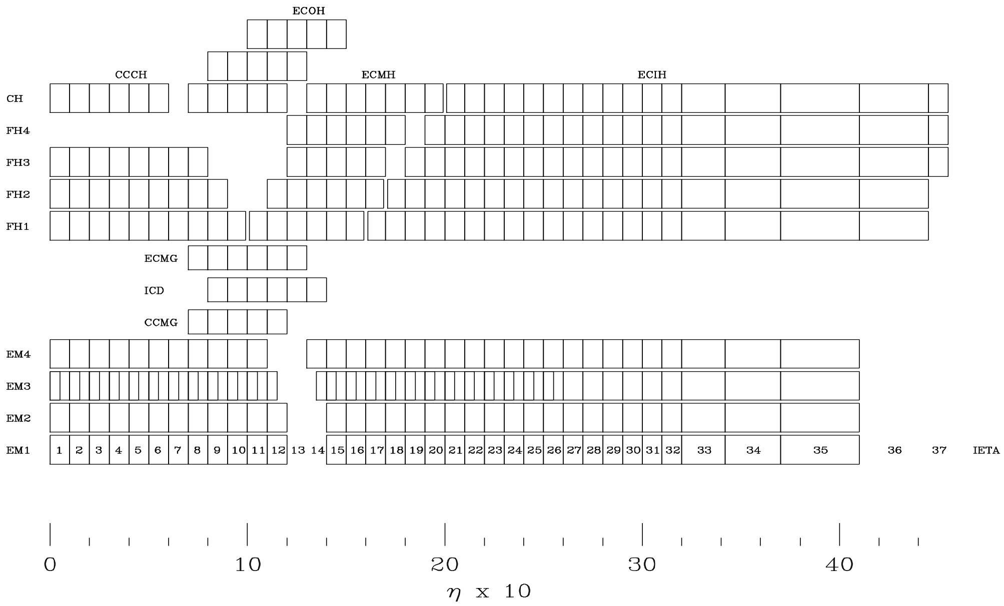

Figure 4.5: The layer structure of the DØ calorimeter

- **Coarse Hadronic Section (CH)**: The CH section has just one longitudinal segment of either thick copper (CC) or stainless absorber plates (EC) with 0.1×0.1 segmentation. The thickness of the section is $3 \sim 4$ λ_I depending on the location of the incident particle. The modules contain hadronic shower energy leaking from the EM and FH sections. The typical module resolutions are listed in the table 4.2 [5].

4.3.1 Operation Principles

The DØ calorimeter is a sampling calorimeter using depleted uranium as the passive material (absorber) and liquid argon (LAr) as the active material. A typical unit cell of the calorimeter consists of a uranium plate and a readout board submerged in LAr as shown in Fig. 4.6. The readout board consists of two separate 0.5 mm thick G-10 boards, one side of which is coated with a high resistivity epoxy. One of the inner surfaces is bare G-10; the other inner surface is copper-coated. These two

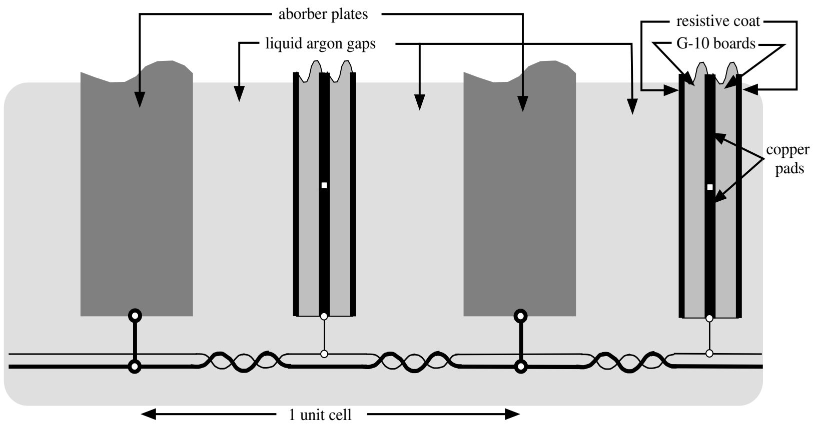

Figure 4.6: A typical unit cell of the calorimeter

G-10 boards were laminated with the resistance coats facing outward. An electric field is formed by grounding the metal absorber plate and connecting the resistive surfaces of the readout board to a positive high voltage (2.0-2.5 kV). Thus the resistive surfaces act as an anode and the readout board operates as a capacitor.

When a high energy particle goes through dense material, e.g. uranium, a shower of particles occurs via various electromagnetic and hadronic interactions. These particles ionize the active material, e.g. LAr, via electromagnetic interactions. These ionized particles, e.g. electrons, drift to the anode under the influence of the electric field and induce an image charge on the inner copper surface. This charge is routed to external charge-sensitive preamplifiers and subsequently to baseline subtracters (BLS) which are shaping and sampling hybrid circuits. The signal shaping is described by a 430 ns integration time and a 33 μs differentiation time. The shaped signal has a relatively broad maximum at around 2.2 μs. At the input to the BLS a portion of the signal is extracted and added into trigger towers of $\Delta\eta\times\Delta\phi = 0.2\times0.2$ for early event selection (see sec. 4.5). The baseline and the peak (at 2.2 μs) of the signal are sampled in the circuit and their difference is sent to an analog-digital converter (ADC), the output of which is brought to a computer. If signal values are within a given range ($\pm 2\sigma$) of their pedestal values, their channels are suppressed to reduce the quantity of the output data (zero suppression).

4.3.2 Massless Gap and InterCryostat Detectors

In order to improve particle detection in the gap between cryostats ($0.8 \lesssim |\eta_d| \lesssim 1.4$), intercryostat detectors (ICD) were built and mounted on the front surface of the ECs as shown in Fig. 4.4. Each ICD consists of 384 scintillator tiles of size 0.1×0.1 in $\eta \times \phi$, exactly matching the liquid argon calorimeter cells. In addition, massless gap (MG) detectors are installed in both CC and EC calorimeters as shown in Fig. 4.4. Massless gap detectors consists of read-out cells in which the uranium is replace by a G-10 board with resistive coating. The ICD and the MG provide a good approximation to the standard DØ sampling of EM showers.

4.3.3 Calorimeter Performance

The DØ calorimeter has been tested and calibrated using test beams [50] and collider data, such as $Z \rightarrow e^+e^-$ samples. Electron and pion beams with energies between 2 and 150 GeV have been used to test various sections of the calorimeter. Test beam studies include uniformity, linearity of response, energy resolution and position resolution.

- **Linearity**: Calorimeter linearity and resolution tests have been performed on the EM and IH (inner hadronic, see Fig. 4.5) sections of the end-cap calorimeter. The calorimeter response was linear to within 1% for electrons above $\sim$ 10 GeV and charged pions above $\sim$20 GeV [51]. However, it is known that the non-linear response of low energy particles invokes significant effects on jet energy resolution [52].

Energy resolution - electromagnetic	$15\%/\sqrt{E}(\mathrm{GeV}) + 0.3\%$
Energy resolution - hadronic	$50\%/\sqrt{E}(\mathrm{GeV}) + 4\%$
Position resolution(EM)	$2\mathrm{cm}/\sqrt{E}(\mathrm{GeV})$

Table 4.2: The performance of the DØ calorimeter

- **Uniformity**: At low energies, where radiative process is not significant, one could use the muon (15 GeV/c) signal to study the uniformity of the calorimeter modules. The uniformity in depth has been studied by comparing the muon signal on individual layers of ECEM and ECIH modules. Excellent uniformity in the response, better than 1%, was obtained [50].

- **Energy resolution**: Energy resolution for electrons and pions was obtained after subtraction of pedestals and corrections for gain variations. The results were fully consistent with expectations and are listed in Table 4.2. It was also found that the noise contribution was predominantly due to uranium radioactivity. The jet resolution determined in simulation is approximately $85\%/\sqrt{E}$. This concurs with recent studies done with collider data [53].

- **Position resolution**: The calorimeter position resolution is important for identification of electron background from near-overlap of photons and charged particles. With the EM section a position resolution of $2\mathrm{cm}/\sqrt{E}$ was obtained for electrons.

The resolution and linearity of a calorimeter is closely related to the ratio of response of electrons and pions (e/π) [54]. For the DØ calorimeter the e/π ratio falls from about 1.11 at 10 GeV to about 1.04 at 150 GeV. The higher electromagnetic response at low energy affects the jet energy resolution significantly.

4.4 The Muon System

The DØ muon detection system consists of solid-iron toroidal magnets and three layers of proportional drift tube chambers (PDTs). One layer of PDT chambers inside the toroidal magnets has four drift planes. The other two layers have three planes respectively and are located outside the magnet. The purpose of this system is to identify muons produced in proton-antiproton collisions and to measure their momenta using trajectories before and after they pass through the magnets. The incident direction is determined from a combination of the primary interaction point, the track matched in the CD and the first muon chamber track vectors. The determination of the outgoing direction depends on the track vector from the outside two PDT layers.

The muon system is divided into two sub-systems, wide angle muon chambers (WAMUS) covering the central region ($|\eta_d| < 2.5$) and small angle muon chambers (SAMUS) with forward and backward coverage ($2.5 < |\eta_d| < 3.6$). The toroidal magnets are also separated into three parts: a central toroid covering the region $|\eta_d| < 1.0$, two end toroids for $1 < |\eta_d| < 2.5$ and two SAMUS toroids covering $2.5 < |\eta_d| < 3.6$. Since a muon must traverse the calorimeter and the thick toroidal magnet, it requires a minimum momentum of 3.5GeV/c at $\eta = 0$ and 5GeV/c at $\eta = 2$. The muon momentum resolution is $\sigma(1/p) = 0.18(p-2)/p^2 \oplus 0.008$ with p in GeV/c.

4.5 The Trigger system

The DØ trigger has three levels in order to select and record interesting physics and calibration events. The Level 0 scintillation counters indicate the occurrence of an inelastic collision. At a luminosity of $L = 5 \times 10^{30}$ cm^{-2}s^{-1}, the Level 0 rate is about 150 kHz. The Level 1 trigger is a collection of hardware trigger elements using signals from all sub-detectors. Most of the Level 1 hardware triggers operate within the 3.5 μs time interval between beam crossings and do not contribute deadtime. Some of the Level 1 triggers require longer operation time and are referred as Level 1.5 triggers. The Level 1 trigger rate is around 200 Hz. After Level 1 (or 1.5), the data are brought to a farm of microprocessors through the standard DØ data acquisition pathways. The farm of microprocessors, Level 2, reconstructs the data and selects event to reduce the event rate to about 2 Hz. These trigger levels are described below.

Level 0:

The Level 0 trigger utilizes the coincidence signal of two scintillation hodoscopes which are located on the front surfaces (140 cm from the center of the detector) of the end calorimeters. These hodoscopes have partial azimuthal coverage for 1.9 $< |\eta_d| < 4.3$ and nearly full coverage for $2.3 < |\eta_d| < 3.9$. The rapidity coverage was determined by requiring that a coincidence of both scintillation hodoscopes should be $\geq 99\%$ efficient in detecting non-diffractive inelastic collisions. In addition, the Level 0 provides the z-coordinate of the primary collision vertex and serves as a luminosity monitoring device. The z-coordinate is determined from the difference in the arrival time for the particles hitting the two hodoscopes. A cut on the z-coordinate of the primary vertex ($|z| \leq 10.5$cm) is applied to all the jet event triggers except the highest E_t trigger. In the case of multiple interactions the Level 0 time difference is ambiguous and is used to set a flag identifying these events. Level 0 is also used to veto events which happen to have beam coincidentally in the Main-Ring passing through the DØ coarse hadronic calorimeter.

Level 1 for Jet Trigger:

The Level 1 calorimeter trigger is used to tag jets in events. Each trigger tower sums all the energy deposited in $\eta \times \phi = 0.2 \times 0.2$. The trigger coverage is $|\eta_d| \leq 3.2$. The number of trigger towers which have transverse momenta above a specified threshold is used to define different sets of the jet triggers as listed in Table 4.3.

Level 2 for Jet Trigger:

The Level 2 trigger is also called a Level 2 filter since it does software selection. It performs a fast event reconstruction of the calorimeter region adjacent to the Level 1 trigger towers (E_t > 3GeV) using a cone algorithm with a radius $R = \sqrt{\Delta\eta^2 + \Delta\phi^2} = 0.7$ to find jets. Like the Level 1, the minimum number of jets above a certain E_t threshold defines several sets of the filters as shown in the table 4.3. The whole operation takes about 200 ms.

Trigger Name	Level 0	Level 1	Level 2
JET_MIN	LØ(10.5)	JT(1,3)	L2JT(1,20)
JET_LOW	LØ(10.5)	JT(1,7)	L2JT(1,30)
JET_MEDIUM	LØ(10.5)	JT(2,7)	L2JT(1,50)
JET_HIGH	LØ(10.5)	JT(3,7)	L2JT(1,85)
JET_MAX		JT(4,5)	L2JT(1,118)

Table 4.3: The jet triggers. The z-vertex position is given in cm and E_t thresholds in GeV. The z-vertex is not always applied to JET_HIGH. JT(n,E_t) means that at least **n** trigger towers had transverse momentum greater than the minimum E_t. L2JT(n,E_t) is for jets, not for trigger tower, and means that at least **n** jets had transverse momentum greater than E_t.

Chapter 5

Jet Reconstruction

A quark or gluon produced in a hard scattering is characterized by a collimated spray of large p_t hadrons or a jet. Such a jet in the DØ calorimeter is identified as a localized peak of hadronic energy in a group of adjacent calorimeter cells or towers. The DØ experiment has adopted a cone algorithm to reconstruct jets from the calorimeter cells [55]. In this Chapter we shall discuss the jet algorithm, energy correction, energy and position resolutions.

5.1 DØ Cone Algorithm

The DØ experiment has developed a fixed cone algorithm for the jet reconstruction which is similar to the Snowmass jet algorithm mentioned in section 3.2. If the energy E_i in each calorimeter cell i is the energy of a "massless" particle the momentum vector of a calorimeter cell is given by,

$$\vec{E}_i = \hat{n} E_i \tag{5.1}$$

where $\vec{E}_i \equiv \vec{P}_i$ and $\hat{n}$ is a unit vector pointing from the primary interaction vertex to the geometrical center of each cell i. The primary interaction vertex is determined by using the tracks reconstructed in the central tracking system, CDC or FDC, with resolution around 1-2 cm in z for typical high-p_t events [56]. The momentum of a projective tower k is defined as a vector sum of the momenta of all cells in the tower:

$$\vec{E}^k = \sum_i^{all\ cells} \vec{E}_i^k. \tag{5.2}$$

The energy, transverse momentum and position of a tower are defined as follows.

$$\begin{aligned}
E^k &= \sum_i^{all\ cells} E_i^k \\
E_T^k &= \sqrt{(E_x^k)^2 + (E_y^k)^2} \\
\phi^k &= \tan^{-1} \frac{E_y^k}{E_x^k} \\
\theta^k &= \cos^{-1} \frac{E_z^k}{\sqrt{(E_x^k)^2 + (E_y^k)^2 + (E_z^k)^2}} \\
\eta^k &= -\log(\tan(\frac{\theta^k}{2})).
\end{aligned} \tag{5.3}$$

The DØ jet reconstruction starts from the above projective tower quantities. In the fixed cone algorithm a jet consists of towers in the calorimeter with momentum vectors located in a cone of radius $R = \sqrt{(\Delta\eta)^2 + (\Delta\phi)^2}$.

The DØ jet algorithm can be divided into three distinct steps:

- **Preclustering :** First, towers with $E_T \geq 1$ GeV are selected and registered as *seed* towers in descending order of E_T. The highest E_T tower is singled out as the first precluster *seed*. The first precluster is formed by adding neighboring towers ($E_T \geq 1$) within a square of ± 0.3 in $\eta \times \phi$ space to the seed tower. The towers included in the precluster are removed from the seed list and the highest E_T tower among the rest of the towers is used as the next seed for the next precluster. This preclustering is repeated until all towers with $E_T \geq 1$ GeV are assigned to a precluster.

- **Cone Clustering :** Cone clustering begins with the above preclusters. The E_T weighted centroid (η_0, ϕ_0) of a precluster is calculated and considered as the center of a jet. This jet is formed with all towers located within a cone of radius $R = \sqrt{(\eta - \eta_0)^2 + (\phi - \phi_0)^2} = 0.7$. The centroid of the jet is reassigned using the E_T weighted method as follows:

$$\begin{aligned}
\eta_{jet} &= \frac{\sum_i^{towers} \eta_i E_{Ti}}{\sum_i^{towers} E_{Ti}} \\
\phi_{jet} &= \frac{\sum_i^{towers} \phi_i E_{Ti}}{\sum_i^{towers} E_{Ti}}
\end{aligned} \tag{5.4}$$

This process is iterated until the new centroid (η_{jet}, ϕ_{jet}) is within the distance of 0.0001 in $\eta \times \phi$ space from the previous jet centroid. Once the centroid stabilizes the transverse momentum and position of the jet are recalculated using the DØ algorithm:

$$\begin{aligned}
\theta_{jet} &= \cos^{-1} \frac{E_z}{\sqrt{(E_x)^2 + (E_y)^2 + (E_z)^2}} \\
\eta_{jet} &= -\log(\tan(\frac{\theta_{jet}}{2})) \\
\phi_{jet} &= \tan^{-1} \frac{E_y}{E_x}
\end{aligned} \tag{5.5}$$

where

$$E_j = \sum_i^{towers} E_{ji} \quad for \quad j = x, y, z$$

The energy (transverse energy) of the jet is defined as the scalar sum of the energy (transverse energy) of each tower within the jet cone.

$$\begin{aligned}
E_{jet} &= \sum_i^{towers} E_i \\
E_{T jet} &= \sum_i^{towers} E_{Ti}
\end{aligned} \tag{5.6}$$

If the transverse energy E_T of this reconstructed jet is greater than 8 GeV the jet is retained for further consideration. This cone clustering process moves on to the next precluster and is repeated for all preclusters.

- **Splitting/Merging :** The reconstructed jet cones can overlap and share some part of their energy. In this case one needs to define a criterion to split or merge those overlapping jets. If the shared E_T is more than 50% of the jet with the smaller E_T the jets are merged into a new jet. On the other hand if the shared E_T fraction is less than 50% the jets are split by assigning each shared cell to the jet whose center is nearest that cell. In either case, E, E_T and positions of those jets are recalculated using Eqs.(5.5) and (5.6). This procedure is repeated until there are no overlapping jets.

5.2 Jet Energy Scale Correction

As previously mentioned jets appear as localized peaks of hadronic energy in a group of adjacent calorimeter cells or towers. In order to reconstruct the correct jet energies one needs to consider several factors contributing to jet energy response: non-uniformity and non-linear response of the calorimeter, noise due to the radioactivity of uranium, zero suppression and energy from the underlying events which are the interactions of the spectator partons in $p\bar{p}$ collisions.

For a 50 GeV jet, approximately 67% of the total jet energy comes from particles with energies below 5 GeV [57]. According to test beam results the response of the calorimeter to these low energy particles, electrons or pions, is lower than that predicted from the response to higher energy particles [57]. Thus the abundance of low energy hadrons in a jet becomes a dominate barrier to the accuracy of the jet energy scale correction.

A jet consists of the calorimeter towers inside a cone of $R = \sqrt{(\Delta\eta)^2 + (\Delta\phi)^2} = 0.7$ and the measured jet energy E_{cal} is the sum of the observed energy in those towers. The true energy, E_{true}, of the jet is the sum of the energy of all particles within the same cone assuming no instrumental losses. The relation between the measured energy and the true energy of a jet is,

$$E_{cal} = E_{true} R_{had}(E, \eta)[1 + C(E, \eta)] + U + N \tag{5.7}$$

where R_{had} is the overall hadronic response of the calorimeter which depends on the energy and pseudorapidity of a jet, C is an algorithm correction for the losses, particularly unclustered energy, caused by the broad showering of jets in the calorimeter. The last two terms represent corrections for the underlying events, noise, and zero suppression.

- **EM energy scale**

  The response of the EM calorimeter to electrons or photons is relatively stable compared to the response to hadrons. The EM sections of the calorimeter are calibrated using the invariant mass peak of Z$\rightarrow$ ee production and the central Z mass (M_Z) from LEP experiments[58]. By requiring both electrons to be in a single calorimeter cryostat the absolute EM scale for each cryostat was obtained. Also low mass resonances ($\pi^0 \rightarrow \gamma\gamma, J/\psi \rightarrow ee$) were used to check the EM scale at different energies[59].

- **Central Jet Energy Scale**

  We have used direct photon events to calibrate jet energy in the central region ($|\eta| < 0.7$) with the the missing transverse energy projection fraction (MPF) method introduced by the CDF collaboration[60]. At leading order a direct photon event includes a jet balanced in E_T. After the EM energy scale correction any missing E_T in this event is assumed due to the mismeasurement of jet E_T in the detector. The photon and the jet are required to be in the central region $|\eta| < 0.7$ and the MPF is defined as follows,

$$MPF = -\frac{\vec{\not{E}}_T \cdot \hat{n}^\gamma}{E_T^\gamma} \tag{5.8}$$

where $\vec{\not{E}}_T$ is the missing transverse momentum vector, E_T^γ is the transverse momentum of the photon and $\hat{n}^\gamma$ is a unit vector in the direction of the photon. The missing transverse momentum $\not{E}_T$ is defined as

$$\not{E}_T = \sqrt{\not{E}_x{}^2 + \not{E}_y{}^2} \tag{5.9}$$

where

$$\begin{aligned} \not{E}_x &= \sum_i^{all\ cells} E_i \sin\theta_i \cos\phi_i \\ \not{E}_y &= \sum_i^{all\ cells} E_i \sin\theta_i \sin\phi_i \end{aligned} \tag{5.10}$$

The sum is over all calorimeter cells. The MPF reflects the amount of missing transverse momentum due to mismeasurement of the jet E_T in the calorimeter.

The ratio of the hadronic response to the EM response R_{had} is defined as

$$R_{had}(E_{jet}) = 1 + MPF \tag{5.11}$$

where $E_{jet} = E_T^\gamma \cosh\eta_{jet}$ is equal to the true jet energy in a $2 \rightarrow 2$ process. The correction scale to a jet is calculated by the average of the measured jet energy for each $E_T^\gamma \cosh\eta_{jet}$ bin.

The MPF method assumes that the missing transverse energy in the direction opposite the photon is due to a mismeasurement of the jet transverse energy. However there are many factors which produce the missing transverse momentum. For example if there are other jets unreconstructed due to their low E_T or fluctuations in the sampling calorimeter the MPF method will be biased. In order to minimize the bias events with a back-to-back topology only in ϕ are used.

- **Forward Jet Energy Scale**

  Due to the shortage of the statistics of direct photon events in the forward region we can not apply the above method for forward jet calibration. Thus for the calibration of forward jets we have used dijet events which have at least one central jet ($|\eta| < 0.7$) satisfying the trigger conditions. The other jet, the probe jet, is allowed to be at any place in the calorimeter. Since the central jets are calibrated the trigger jet takes the place of the photon in the Eq.(5.8).

  $$MPF = -\frac{\vec{\not{E}}_T \cdot \hat{n}^{trigger}}{E_T^{trigger}} \tag{5.12}$$

  One can get the energy scale as a function of the pseudorapidity of the probing jets using Eq.(5.12)

- **Algorithm Correction**

  Due to the out-of-cone showering in the calorimeter the algorithm correction is necessary to compensate for the loss caused by the finite cone size. Central jets ($|\eta| < 0.7$) are generated with the HERWIG Monte Carlo at various energies. The calorimeter response to the Monte Carlo generated jets is simulated substituting the test beam data of electrons and pions for the hadrons and photons in the Monte Carlo jets. The shower profile of the test beam was used to mimic showered jets in the calorimeter cells. By applying the cone algorithm for the unshowered jets and the showered jets, the loss due to the out-of-cone showering was extracted.

- **Underlying Events and Noise**

  The energy of jets reconstructed by the cone algorithm includes the energy from the underlying event (spectator interactions) and uranium noise. These external contributions to the jet energy are determined from events selected by a minimum bias trigger. The minimum bias trigger in the DØ experiment requires only the coincidence of the forward and backward hodoscopes. The E_T

distribution of minimum bias events is expected to be flat in pseudorapidity[40] and can be extracted using the differences between single and double interaction events among minimum bias events. We expect that double interaction events have twice the contribution from underlying events as do single interaction events.

Since the DØ calorimeter has almost a constant number of channels per pseudorapidity interval, the energy contribution from uranium noise is also expected to be a fairly constant as a function of pseudorapidity and the same for single or multiple interaction events. This implies that its E_T distribution falls off as a function of $\sin\theta$. The transverse momentum density from minimum bias events is then parameterized as follow.

$$U + N = 0.6 + 1.2\sin\theta \ (\mathrm{GeV/rad}/\eta) \tag{5.13}$$

We can here presume that 0.6 GeV/rad/η is from the underlying events and $1.2\sin\theta$ GeV/rad/η from uranium noise.

With the MPF methods the overall hadronic response R_{had} was obtained. The algorithm correction C was calculated using HERWIG Monte Carlo and test beam data and the contribution from the underlying events and noise was obtained using minimum bias events. The final correction factors E_{true}/E_{cal} are shown in Fig. 5.1. The hadronic response is flat above 60 GeV. The energy scale curve below 20 GeV decreases sharply because of the reconstruction threshold of 8 GeV and the at least one jet requirement in the MPF method. Low E_T jets occasionally fluctuate to higher E_T to satisfy those cuts and hence the bins near the 8 GeV threshold tend to be biased. The second plot of Fig. 5.1 shows a slight increase in the energy scale since the forward region consists of much smaller towers in physical size which enhance the out-of-cone showering effect, an algorithm dependent losses.

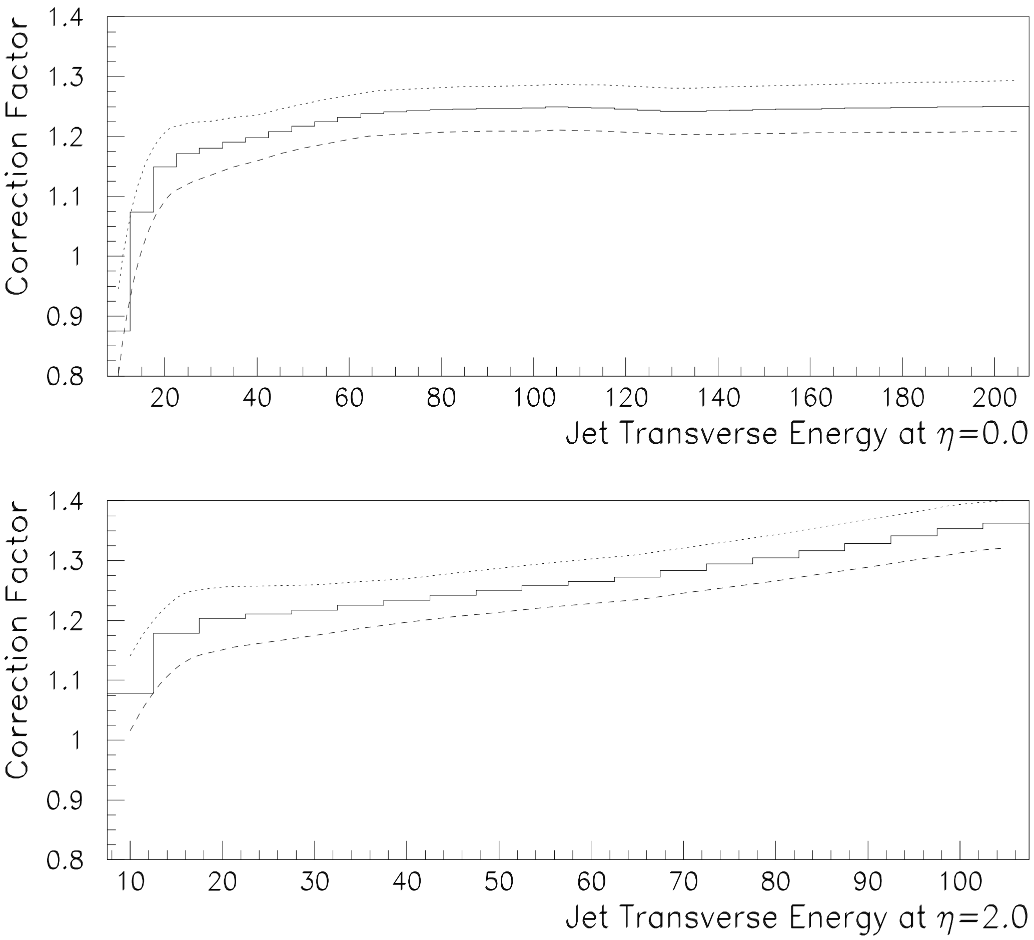

Figure 5.1: Jet Energy Scale Correction Version 4.2: The top plot shows the jet energy scale as a function of jet E_T at $\eta = 0.0$, and the bottom at $\eta = 2.0$. The dotted and dashed lines represent $\pm 1\sigma$ uncertainty.

5.3 Energy Resolution

The abundance of low energy hadrons in a jet dominates the jet resolution as well as the jet response. The jet energy scale correction is performed for the average response of a jet. As shown in Fig. 5.1 a jet of 100 GeV in the central region needs around 20% correction on average. The energy resolution study has been performed after the jet energy scale correction.

The determination of jet energy resolution is based on the momentum conservation in the transverse plane between the leading two jets in a event. Thus, the events are selected very carefully to minimize the effect of additional low E_T jets and contamination of the sample [53]. The following cuts are applied to select clean dijet events.

- The z-coordinate of the vertex must be within ± 100cm of the center of the detector.
- The two leading jets must have $E_T > 15$GeV and be back–to–back in ϕ within 25^0. If there are other jets in the events they should have $E_T < 10$GeV.
- All the jets must satisfy the jet quality cuts [61].
- The two leading jets must be in the same η region so that their resolutions are approximately equal. In addition, the jet pseudorapidity is corrected for a jet reconstruction bias which will be discussed in the next section.

Jet energy resolution is determined by using the dijet asymmetry variable A, defined as:

$$A \equiv \frac{E_{T_1} - E_{T_2}}{E_{T_1} + E_{T_2}} \tag{5.14}$$

where E_{T_1} and E_{T_2} are the transverse energies of the two leading jets. The variance of the asymmetry A is

$$\sigma_A^2 = \left(\left| \frac{\partial A}{\partial E_{T_1}} \right| \sigma_{E_{T_1}} \right)^2 + \left(\left| \frac{\partial A}{\partial E_{T_2}} \right| \sigma_{E_{T_2}} \right)^2 \tag{5.15}$$

Assuming $E_{T_1} \sim E_{T_2} \equiv E_T$ and $\sigma_{E_{T_1}} \sim \sigma_{E_{T_2}} \equiv \sigma_{E_T}$ the jet energy resolution can be written as:

$$\left(\frac{\sigma_{E_T}}{E_T} \right) = \sqrt{2}\sigma_A \tag{5.16}$$

With the energy corrected jets the jet energy resolution have been calculated as a function of the average E_T of the two leading jets for five different regions of pseudo-rapidity: $|\eta| < 0.5, 0.5 < |\eta| < 1.0, 1.0 < |\eta| < 1.5, 1.5 < |\eta| < 2.0, 2.0 < |\eta| < 3.0$. Since the resolution uncertainty due to angular smearing is almost negligible we can assume $\sigma_{E_T}/E_T = \sigma_E/E$. The results, shown in Fig. 5.2, are fit to the following function:

$$\left(\frac{\sigma_E}{E} \right)^2 = \left(\frac{N}{E} \right)^2 + \left(\frac{S}{\sqrt{E}} \right)^2 + C^2 \tag{5.17}$$

The fit parameters are listed in Table 5.1.

In case of a single particle the three coefficients in the above equation have the following meaning: the first term N represents the contribution from uranium noise. This contribution is independent of the particle energy E and dominates at low energy. The sampling term S depends on the number of electrons or photons in a shower process and is the most important term in the resolution parameterization. The constant term C represents contributions from calibration uncertainties, non-linear and non-uniform response, and leakage out of the calorimeter. This term is proportional to the energy E of the incident particle and dominates at high energy.

Since a jet consists of many particles at different energies the above interpretation for a single particle may not be appropriate for jet energy resolution. If we presume,

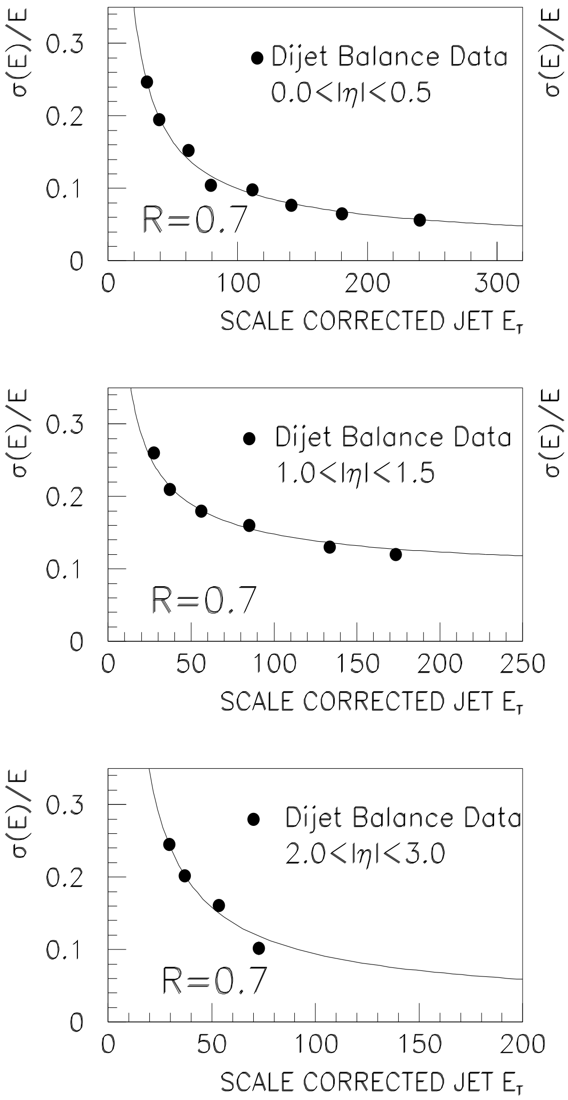

Figure 5.2: Jet Energy Resolution as a function of Scale Corrected Jet E_T in all η regions for R = 0.7 cone jets.

η Region	Noise Term (N)	Sampling Term (S)	Constant Term (C)
$\|\eta\| < 0.5$	5.97 ± 0.12	0.80 ± 0.02	0.00 ± 0.01
$0.5 < \|\eta\| < 1.0$	6.61 ± 0.19	0.68 ± 0.06	0.00 ± 0.01
$1.0 < \|\eta\| < 1.5$	1.83 ± 2.34	1.14 ± 0.13	0.05 ± 0.01
$1.5 < \|\eta\| < 2.0$	7.17 ± 0.35	0.56 ± 0.12	0.09 ± 0.04
$2.0 < \|\eta\| < 3.0$	6.09 ± 0.23	0.71 ± 0.06	0.00 ± 0.07

Table 5.1: Jet energy resolution as a function of pseudorapidity interval.

however, that the sampling fluctuation from low energy particles dominates, the above data show $\sim 80\%$ of the jet energy resolution. As we expected, this is higher than a single pion resolution, $\sim 50\%$.

5.4 Position Bias Corrections and Position Resolution

Any bias in jet position determination is expected to depend on the jet shape which is strongly related to hadronization and showering in the calorimeter [62]. We have used the parton shower Monte Carlo HERWIG 4.6 [63] to model the hadronization, and DØ GEANT [64], the full DØ detector simulator, to simulate the interactions and showering of particles in the calorimeter. This process provides jets with a realistic shape[65]. Jets at the parton and particle level (PJET) were reconstructed using a package called PJETS [66] with a cone of radius $R(=\sqrt{\Delta\eta^2 + \Delta\phi^2}) = 0.7$ and a minimum transverse energy of $E_T^{min} = 10\text{GeV}$. PJETS mimics the real jet reconstruction except that it uses parton or particle energies rather than calorimeter tower energies to compute the fair momenta of the reconstructed jets. We perform only one iteration and no splitting/merging for PJETS. Jets at the calorimeter level (CAJET) are reconstructed using the DØ standard reconstruction algorithm with a cone of radius $R = 0.7$ and $E_T^{min} = 8$GeV. QCD $2 \rightarrow 2$ parton event samples are generated at the vertex position $z = 0$, so the detector pseudorapidity η_d is the same as the physics η. Assuming perfect position resolution η of a jet would be:

$$\eta_d^{parton} = \eta_d^{reco} + \delta(E_{jet}^{reco}, \eta_d^{reco}) \tag{5.18}$$

where η_d^{reco} is the reconstructed calorimeter jet η and δ is the bias which may be extracted from Monte Carlo. $\delta(E_{jet}^{reco}, \eta_d^{reco})$ is the average of $\eta_d^{parton} - \eta_d^{reco}$ where a matching condition is used to associate parton jets with reconstructed jets. The two jets are matched if a single reconstructed jet is within a cone of 0.7 around a parton jet. If there are two jets in the cone the matching cone size is reduced to 0.5. If there is only one reconstructed jet in that reduced cone the jets are matched. If there are still two jets, the reconstructed jet with E_T closest to the parton jet E_T is selected. If no jet is found in the cone there is no matching. Only isolated calorimeter jets are used by requiring the merge/split flag to be zero. If any of the calorimeter jets in an event is merged or split the event is skipped. In other words only simple jets are used to avoid any bias due to merged or split jets.

5.4.1 η Bias

The physical tower size in the calorimeter is a function of pseudorapidity. Since the central calorimeter towers are physically larger than their forward counterparts more energy may be deposited in jet towers at smaller η than at high η. Since the transverse momentum and pseudorapidity of each tower are used to calculate the centroid of a jet it is natural that the center of the jet shifts toward the smaller η. In other words, the pseudorapidity dependence of the physical calorimeter tower

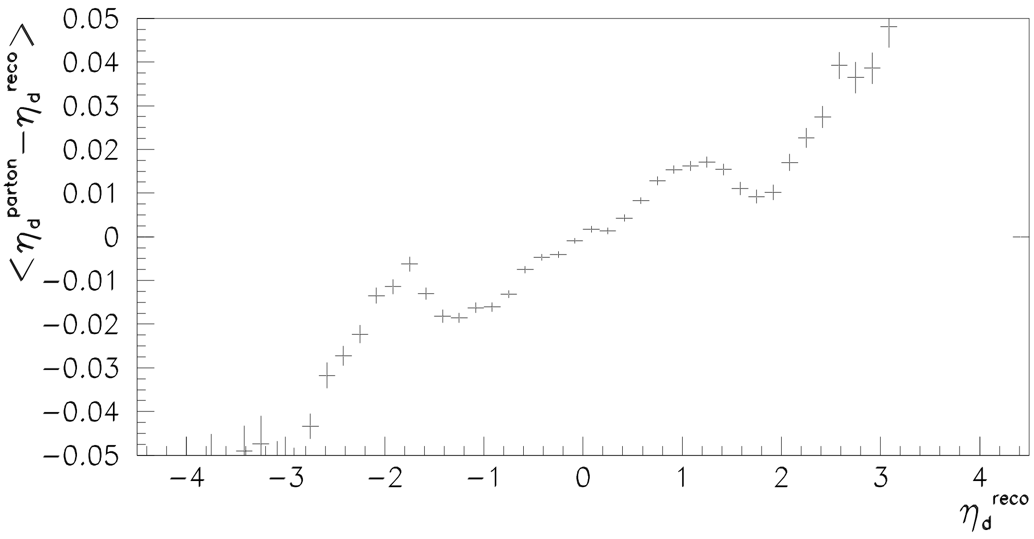

Figure 5.3: HERWIG Monte Carlo simulation of the η bias for all jet energies(GeV) as a function of η_d^{reco}.

size together with the jet algorithm are mainly responsible for a tendency to shift the reconstructed jet η toward the central region. The average of $\eta_d^{parton} - \eta_d^{reco}$ as a function of η_d^{reco} for all energies is shown in Fig. 5.3. Figure 5.4 shows the same quantity in various energy bins. The bias in $|\eta_d| \in [1.0,1.6]$ might be due to lower energy response in the IC region. The increase in the bias for $|\eta_d| > 2.0$ might be due to the rapidly increasing physical size ratio between two neighboring towers as a function of η. More energetic jets have less bias. This may be due to the fact that higher energy jets are collimated and central.

The η bias between a parton jet and the matching particle jet was extracted in the same way and is shown in Fig. 5.5. Since there is no detector showering simulation this represents only the effects due to the DØ jet reconstruction algorithm involved in particle jet reconstruction. As one may notice there is a little bias due to the particle spread during the hadronization. There is no IC region bump as we saw in the detector simulation.

5.4.2 η bias correction

We have used the methodology of reference [67] to determine the correction function for the η bias. Since the bias appears to be symmetric in η the bias from the negative side was projected onto the positive side with a reversed sign to minimize the statistical uncertainty. The sample was divided into 6 energy bins as shown in Fig. 5.4. A third degree polynomial was used to fit the range $|\eta_d| \in$ [0.,1.8] for each histogram. A quadratic function was used for the range $|\eta_d| \in$ [1.8,3.0] and a third degree polynomial for the region $|\eta_d| > 2.4$. The parameterization functions are as follows.

$$\begin{aligned}
\delta(E_{jet}^{reco}, \eta_d^{reco}) &= A + Bx + Cx^2 + Dx^3 \quad for\, |\eta_d| \in [0.1, 1.8] && (5.19)\\
&= A + Bx + Cx^2 \quad for\, |\eta_d| \in [1.8, 3.0] && (5.20)\\
&= A + Bx + Cx^2 + Dx^3 \quad for\, |\eta_d| > 2.4 && (5.21)
\end{aligned}$$

A, B, C and D are the coefficients for the parameterization. They are shown in Table 5.2, 5.3 and 5.4. The overlap between $|\eta_d| \in$ [1.8,3.0] and $|\eta_d| > 2.4$ was used to guarantee the continuity of the parameterization. To cross check the correction parameterization we have applied this correction to the reconstructed jets. Solid crosses in Fig. 5.4 show the bias before the correction whereas the dashed crosses indicate the bias after the correction. No distinct η bias has been observed after the correction was applied.

5.4.3 ϕ Bias

An azimuthal angle bias study was conducted in the same way as in the η study. There is no reason to expect a bias in the azimuthal angle since the calorimeter tower structure is symmetric in ϕ. The average of $\phi^{parton} - \phi^{reco}$ as a function of η_d

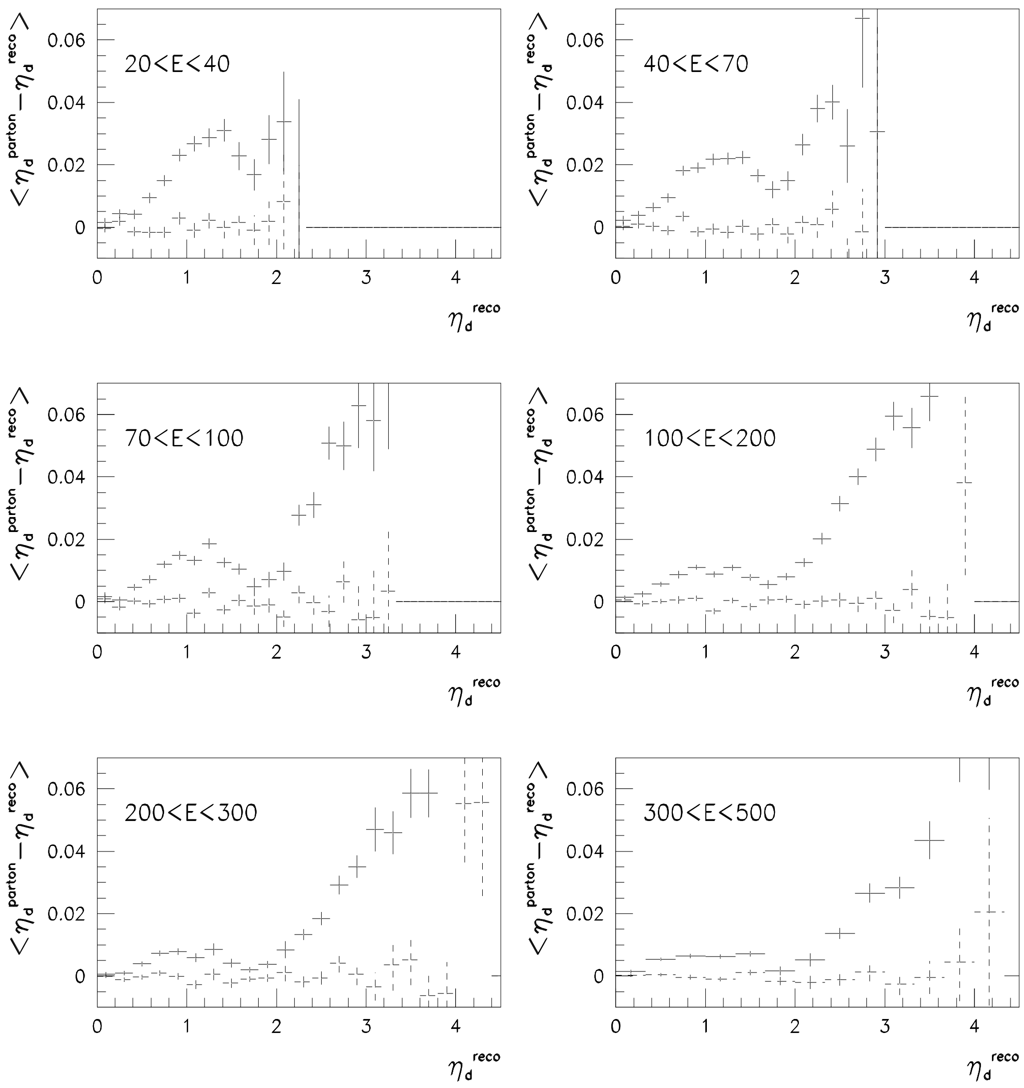

Figure 5.4: HERWIG Monte Carlo simulation of the η bias. $< \delta(E_{jet}^{reco}, \eta_d^{reco}) >$ before the correction are plotted as solid crosses. The dotted crosses represent the bias after the correction.

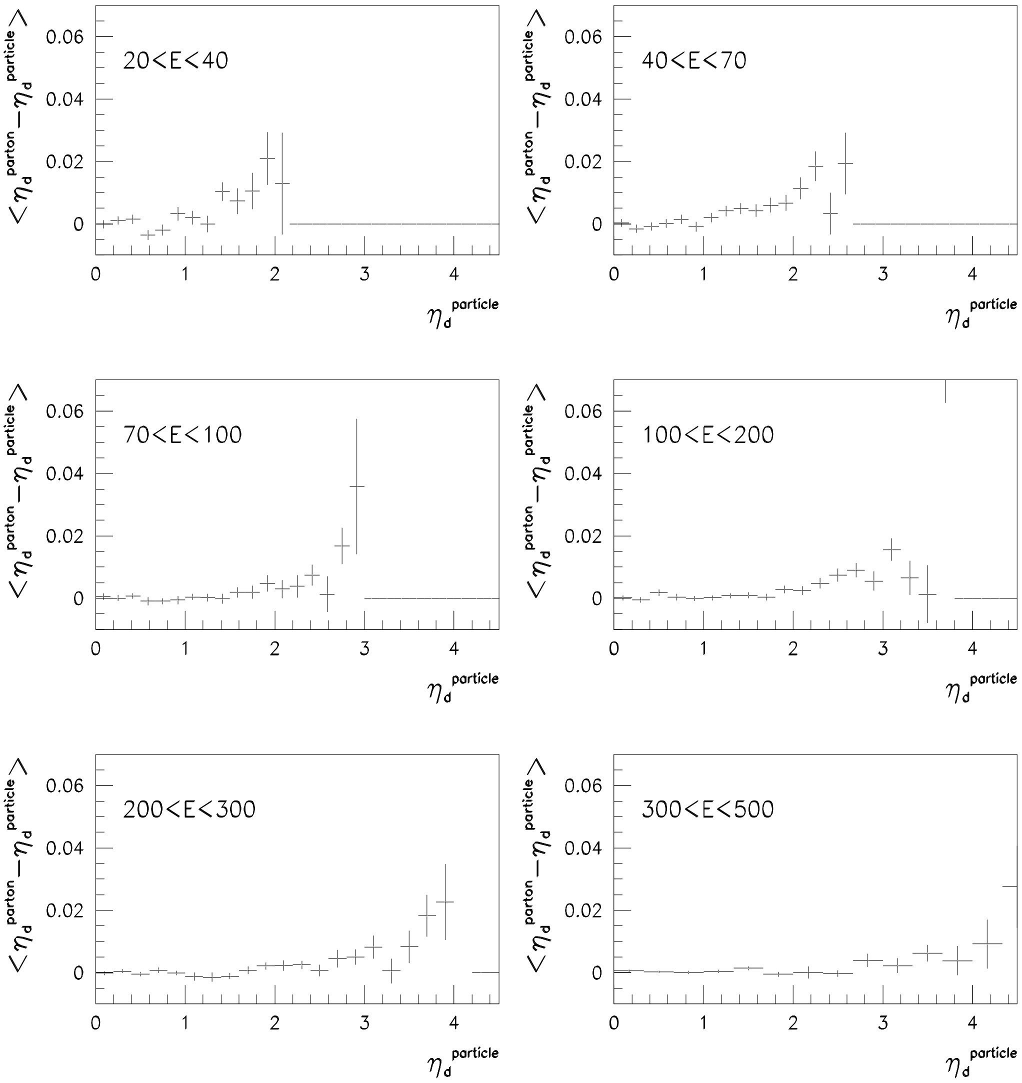

Figure 5.5: HERWIG Monte Carlo simulation of the η bias between parton jets and particle jets as a function of $\eta_d^{particle}$ and energies (GeV)

as shown in Fig. 5.6 indicates the overall shift toward negative $< \phi^{parton} - \phi^{reco} >$ for both positive and negative η_d and that the size of the shift is on the order of -0.01 radian. This distinct bias was not seen between a parton and the matching particle jet. Any bias introduced by this effect will be small for the physics analysis because all jets are systematically shifted in the same direction. For example, the relative angle between 2 jets will be useful for the physics analysis rather than the ϕ position itself of a jet. Therefore any δ_ϕ correction is assumed to be zero.

5.4.4 Position Resolution

Once the bias is parameterized the η_d of the calorimeter jet can be corrected to the initial parton jet η_d value. Although the average of $\eta_d^{parton} - \eta_d^{reco}$ is zero, the overall distribution follows a gaussian distribution due to the finite calorimeter position resolution. The variance $\sigma_\eta(E_{jet}^{parton}, \eta)$ of the gaussian distribution was taken as the jet η resolution. The data was binned with energy boundaries at 20, 40, 70, 100, 200, 300 and 400 GeV. In Figs. 5.7 and 5.8 we plot the η and ϕ resolutions as a function of the average energy in each bin. As can be seen the nominal resolution varies from 0.01 to 0.05. The quantity $\sigma_\eta(E_{jet}^{parton}, \eta)$ was obtained in seven η bins and was parameterized as a function of jet energy as follows.

$$\sigma_\eta(E, \eta) = A + \frac{B}{E} + \frac{C}{E^2} \tag{5.22}$$

The same method is applied to the ϕ resolution study. The parameterization coefficients are listed in Table 5.5 and 5.6 for η and ϕ.

5.5 Reconstruction Efficiency

Although a jet may form an energy cluster in the calorimeter the DØ jet algorithm may not reconstruct the jet. This may happen to broadly distributed and low E_T jets which do not deposit large amounts of energy in a single calorimeter towers.

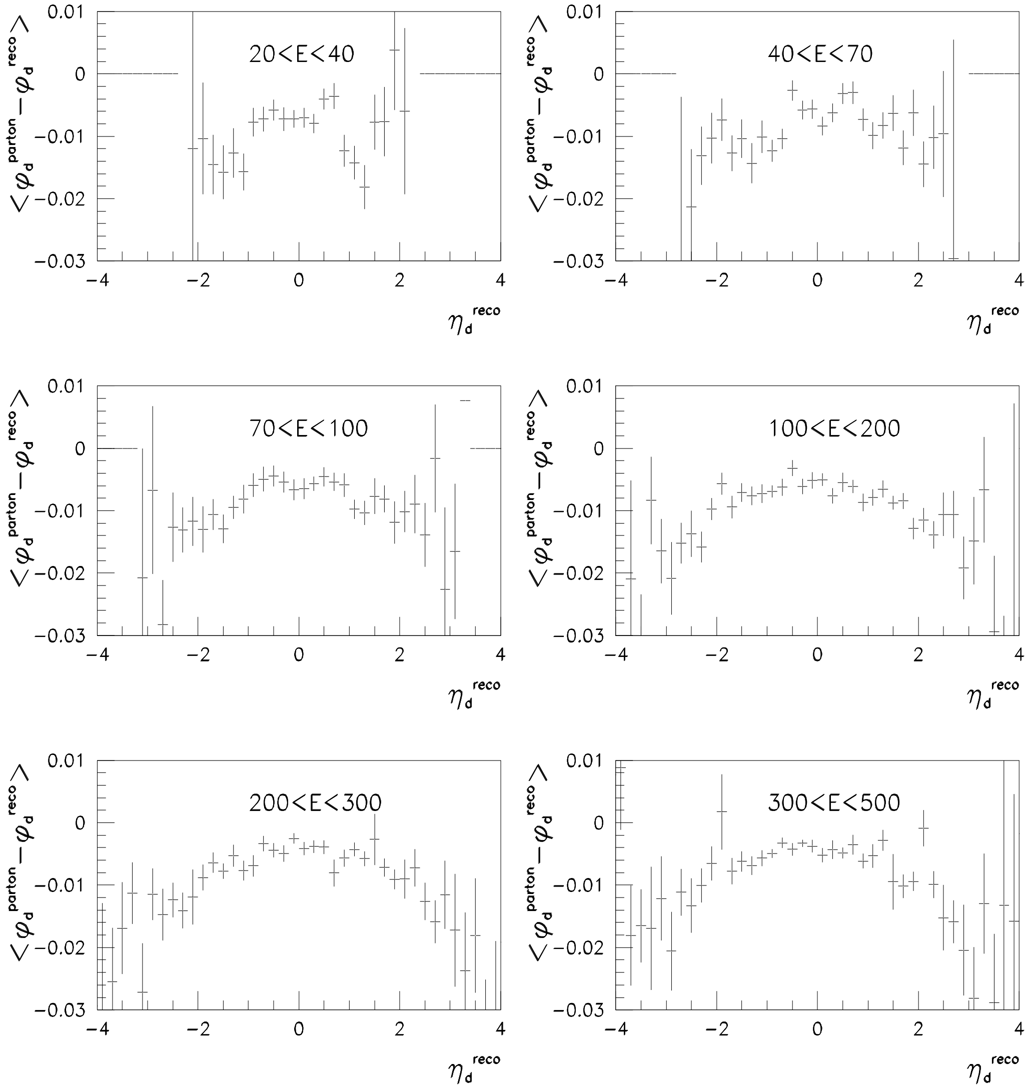

Figure 5.6: HERWIG Monte Carlo simulation of the ϕ bias between parton jets and calorimeter jets as a function of η_d^{reco} and energies (GeV).

	20-40(GeV)	40-70	70-100	100-200	200-300	300-500
A	0.00300	0.00161	0.000469	0.00065	-0.000952	-0.000939
B	-0.0214	-0.00109	-0.00356	0.00737	0.00685	0.0162
C	0.0791	0.0426	0.0385	0.00953	0.0101	-0.00858
D	-0.0359	-0.0224	-0.0205	-0.00722	-0.00765	0.000533

Table 5.2: η bias parameterization for $|\eta_d| \in [0.1,1.8]$.

	20-40(GeV)	40-70	70-100	100-200	200-300	300-500
A	-0.0591	-0.0717	0.0464	0.00553	0.0123	0.00592
B	0.0436	0.0470	-0.0770	-0.0257	-0.0266	-0.0188
C	0.	0.	0.0295	0.0141	0.0117	0.00888

Table 5.3: η bias parameterization for $|\eta_d| \in [1.8,3.0]$.

	20-40(GeV)	40-70	70-100	100-200	200-300	300-500
A	0.0	0.0	-1.09	-0.770	-1.89	-1.04
B	0.0	0.0	1.15	0.760	1.86	1.02
C	0.0	0.0	-0.398	-0.244	-0.605	-0.333
D	0.0	0.0	0.0473	0.0272	0.0662	0.0369

Table 5.4: η bias parameterization for $|\eta_d| > 2.4$.

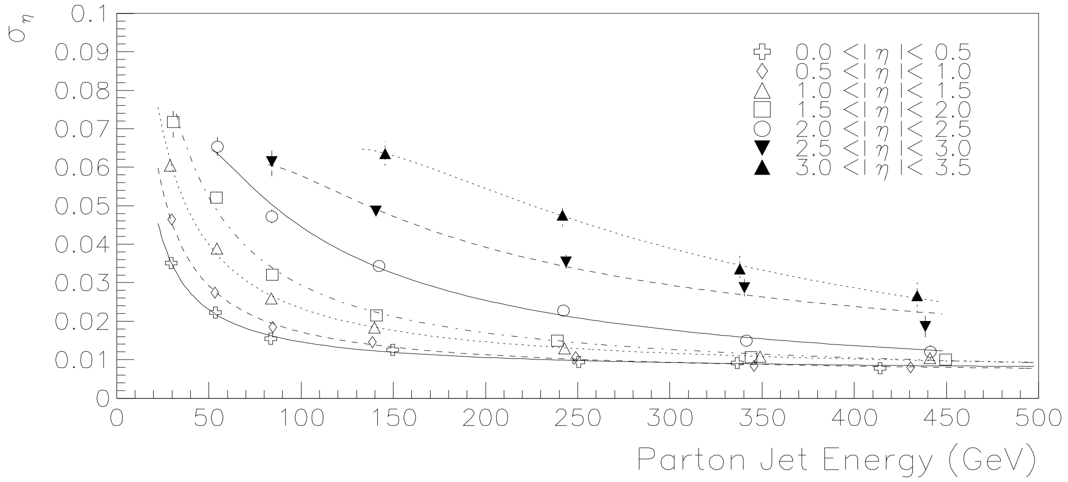

Figure 5.7: The η resolution from a HERWIG Monte Carlo simulation.

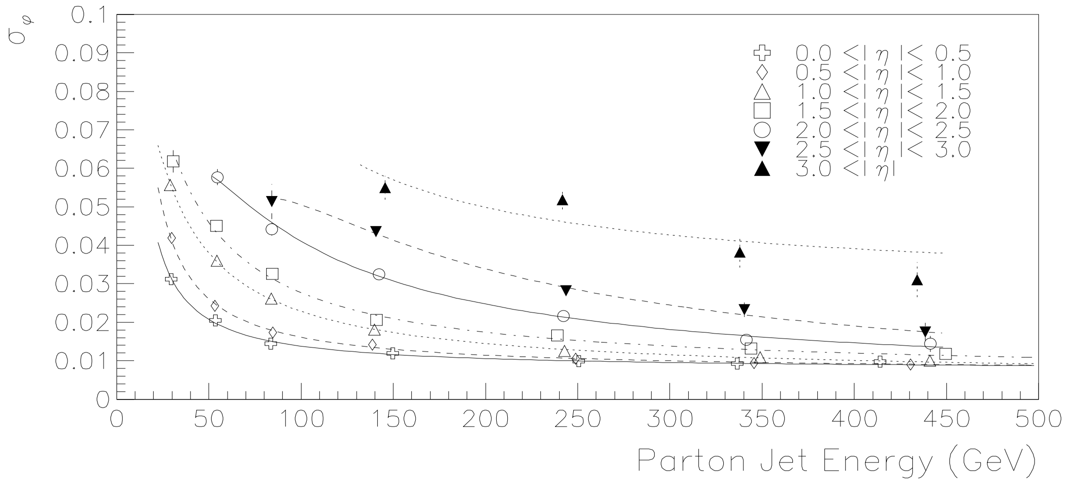

Figure 5.8: The ϕ resolution from a HERWIG Monte Carlo simulation.

η	A	B	C
0.0-0.5	0.006663	0.7727	2.130
0.5-1.0	0.005418	1.164	1.230
1.0-1.5	0.005667	1.826	-5.847
1.5-2.0	0.003866	2.693	-13.84
2.0-2.5	0.0004306	5.578	-116.2
2.5-3.0	0.004273	8.637	-328.4
3.0-3.5	-0.01897	19.64	-1241.

Table 5.5: Parameterization of the jet η resolution.

η	A	B	C
0.0-0.5	0.007554	0.5897	3.452
0.5-1.0	0.007105	0.8484	5.042
1.0-1.5	0.005567	1.836	-10.80
1.5-2.0	0.006334	2.296	-15.85
2.0-2.5	0.003316	4.787	-101.4
2.5-3.0	-0.001437	8.534	-346.7
3.0-	-0.01897	26.59	-2301.

Table 5.6: Parameterization of the jet ϕ resolution.

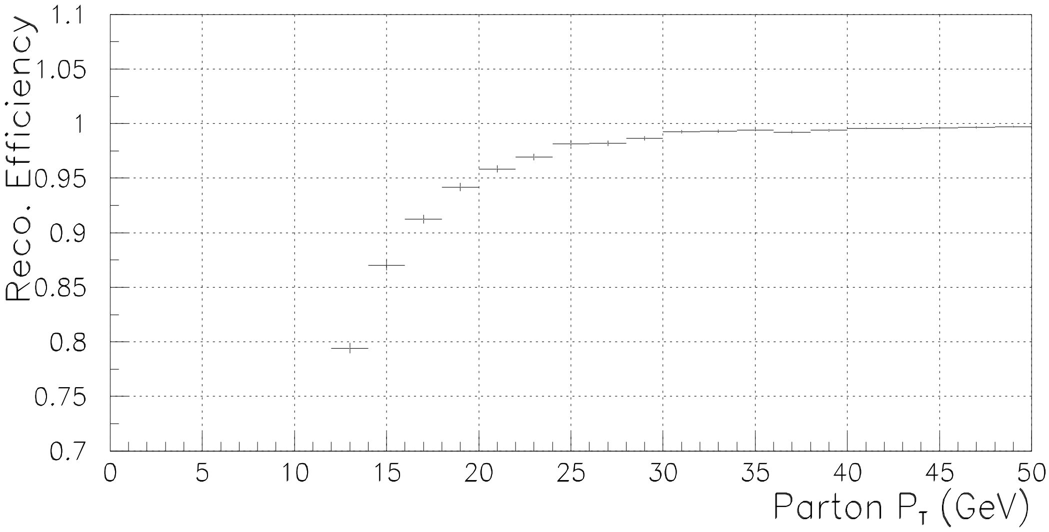

Figure 5.9: Jet reconstruction efficiency as a function of parton jet E_T using HERWIG4.6 and DØ GEANT.

Additionally reconstructed jets are not considered in the DØ jet algorithm if the reconstructed E_T is less than a threshold, 8 GeV. Since the reconstruction efficiency for the forward η region is important for this analysis the HERWIG 5.8 Monte Carlo sample generated for the forward jet statistics was used.

For the purpose of studying the reconstruction efficiency the matching method in the previous section was utilized with the matching cone size R=0.7. In other words, a parton jet (PJET) was defined to be reconstructed if a calorimeter jet was found within a cone of 0.7 around the parton jet.

The efficiency of the jet algorithm is around 95% at 20 GeV and almost 100% at 30 GeV as shown in Fig. 5.9. Other studies using the ISAJET Monte Carlo[57] and data-based analyses[68] showed slightly better efficiency but were consistent with this result. The reconstruction efficiency as a function of pseudorapidity was also obtained for two transverse momentum ranges, $E_T > 20$ GeV and 15 GeV $< E_T <$

25 GeV. As shown in Fig. 5.10 the efficiency is almost constant over all η and $\sim$ 99% for $E_T > 20$ GeV and $\sim$ 95% for 15 GeV $< E_T <$ 25 GeV.

Since splitting/merging was not applied in shaping parton jets (PJETs) we studied the reconstruction efficiency with the selected Monte Carlo events required to have no split or merged CAJETs. These requirements provided somewhat isolated PJETs and CAJETs which are immune to the bias from the PJETS algorithm and the splitting/merging between the overlapping jets. These results were consistent with the above results to within a few percent.

5.6 Trigger Efficiency

There are five different inclusive jet triggers: JET_MIN, JET_LOW, JET_MEDIUM, JET_HIGH, and JET_MAX. For this analysis we have used the JET_LOW trigger which requires at least one trigger tower(0.2×0.2) with $E_T > 7$ GeV at Level 1(L1) and at least one jet with a cone of $R = 0.7$ above 30 GeV in E_T at Level 2(L2).

The efficiency of Level 0(L0) has been calculated to be above 97% [69]. In order to determine the L1 and L2 trigger efficiencies a set of special QCD *Mark-and-Pass*(QPM) runs were taken. In a *Mark-and-Pass* run every event which passed L1 was recorded with a flag indicating the outcome of the L2 trigger decision. The trigger efficiency of JET_LOW was obtained using *Mark-and-Pass* runs for three different η regions: $0.0 < |\eta| < 0.6, 0.6 < |\eta| < 1.6$, and $1.6 < |\eta| < 4.0$[70]. The results in Fig 5.11 show that the combined L1 and L2 triggers for JET_LOW are $\sim$ 90% efficient at $E_T^{uncorrected} = 40$ GeV for all three η regions. The central region and forward regions (Fig.5.11(a)(c)) are $\sim$ 95% efficient while the intercryostat region (Fig.5.11(b)) has a slightly lower efficiency, $\sim$ 90% at $E_T^{uncorrected} = 40$ GeV.

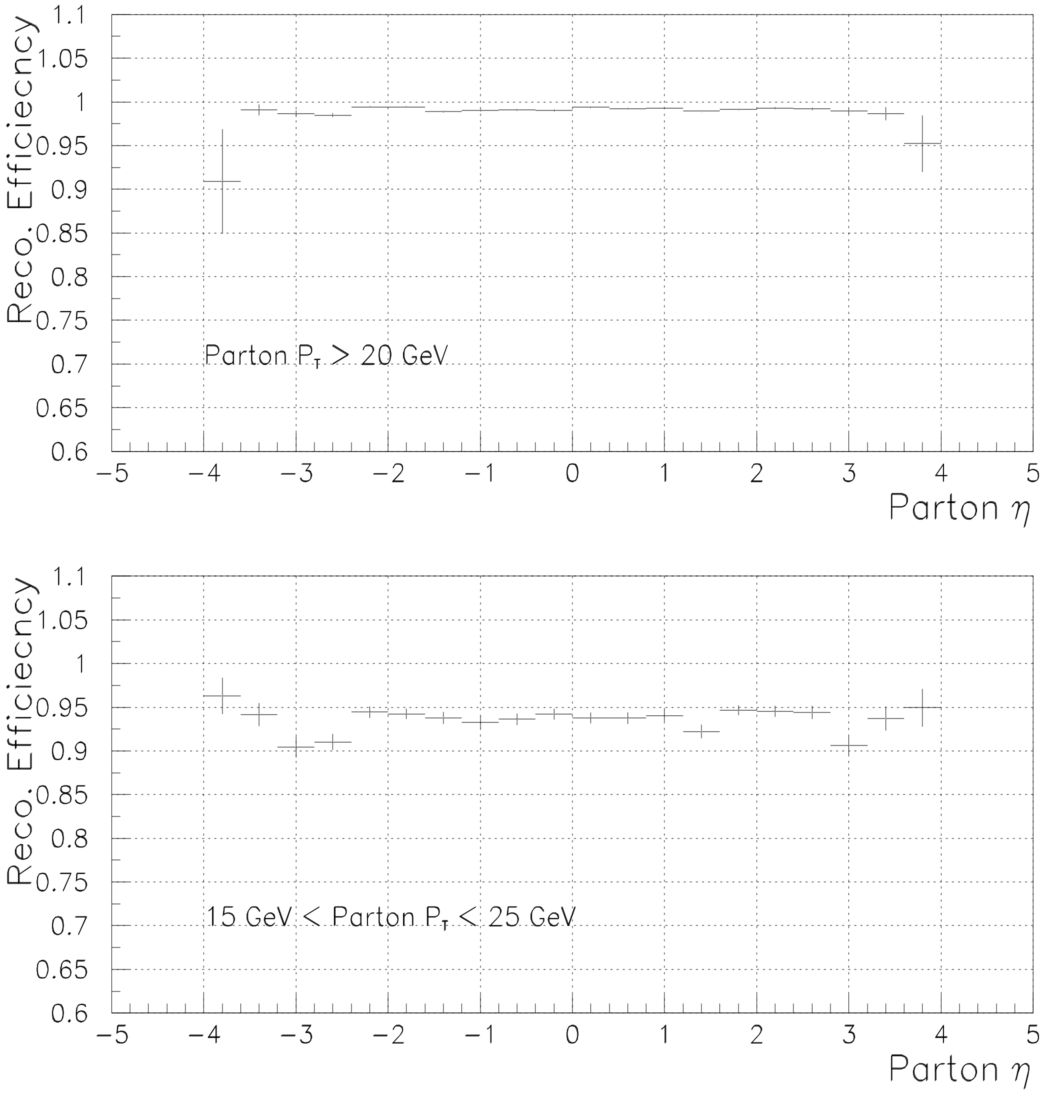

Figure 5.10: Jet reconstruction efficiency as a function of pseudorapidity using HERWIG5.8 and DØ GEANT.

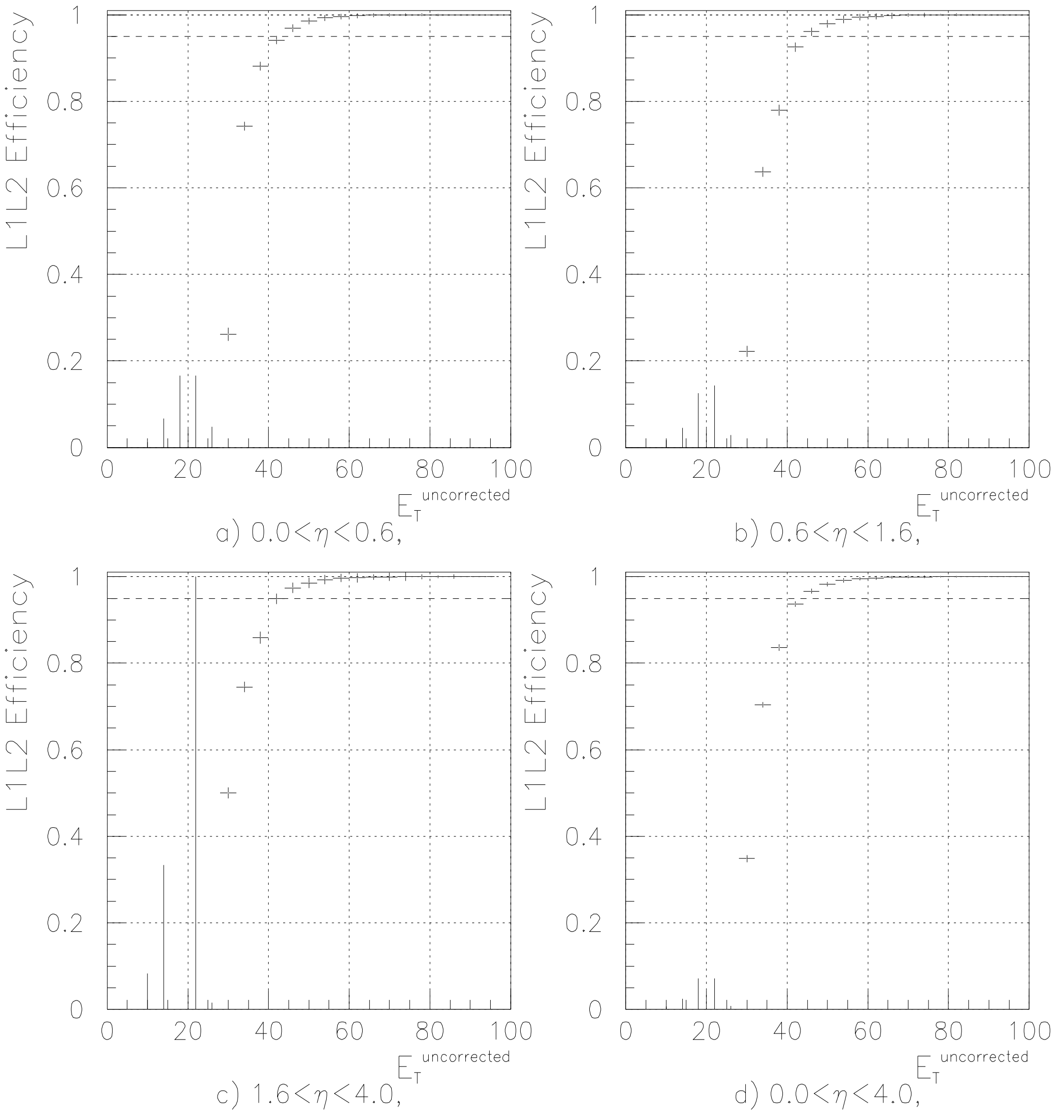

Figure 5.11: Total L1L2 event efficiency for JET_LOW: a) $0.0 < |\eta| < 0.6$, b) $0.6 < |\eta| < 1.6$, c) $1.6 < |\eta| < 4.0$, d) $0.0 < |\eta| < 4.0$.

Chapter 6

Data Selection and Analysis

The data used in this analysis have been taken during the 1992-1993 Tevatron collider run (Run 1A) at $\sqrt{s} = 1.8$ TeV. With instantaneous luminosities ranging from 0.5×10^{30} cm^{-2}s^{-1} to 8.7×10^{30} cm^{-2}s^{-1} the accelerator delivered an integrated luminosity of 27.7 pb^{-1}. Data for 14.9 pb^{-1} have been recorded by the DØ experiment to tape. We have used the JET_LOW trigger for this analysis corresponding to a luminosity of 83 nb^{-1}.

6.1 Luminosity

The DØ integrated luminosity L is obtained by measuring non-diffractive inelastic collisions. With a beam crossing every 3.5 μs, the level Ø hodoscopes were used to select inelastic collisions and monitor the instantaneous luminosity. The calculation of integrated luminosity depends on the beam status and the specific trigger conditions. During normal operations there were six bunches of protons and antiprotons in the Tevatron. Since each bunch had different intensities the six possible beam crossings were treated independently. In addition experimental dead time, prescales, multiple interactions, main ring veto configurations and beam related Level 1 trigger conditions were considered in the calculation of the integrated luminosity. Further corrections for lost events during the offline reconstruction were also performed [71].

- Instantaneous luminosity:

  The instantaneous luminosity $\mathcal{L}$ is simply related to the counting rate $N_{L\emptyset}$ in the level Ø counters by:
  $$\mathcal{L} = \frac{N_{L\emptyset}}{\sigma_{L\emptyset}} \tag{6.1}$$
  where $\sigma_{L\emptyset}$ is the acceptance corrected cross section covered by these counters. Strictly speaking this is true if the instantaneous luminosity is low enough so that the counting rate corresponds to the interaction rate. As the luminosity rises the probability for multiple interactions in a single bunch crossing increases. In this case the counting rate is less than the interaction rate, since the multiple interactions are counted only once. The multiple interaction loss correction is based on Poisson statistics for the average number of interactions per crossing [69].

- The Level Ø monitor constant:

  Since the uncertainty of the monitor constant $\sigma_{L\emptyset}$ is directly related to the luminosity uncertainty the monitor constant should be treated very carefully. The total, elastic and single diffractive cross sections from the E710 [72] and CDF [73] experiments were used in the calculation of the world average cross sections. The inelastic collisions counted by the LØ counters include hard core, single diffractive and double diffractive scattering. The acceptance of the LØ counters for each process was obtained using a zero bias run and the MBR and DTUJET [69] Monte Carlos. The observable cross section for the LØ counters was calculated to be $\sigma_{L\emptyset} = 46.7 \pm 2.5$mb.

- Integrated Luminosity:

  The integrated luminosity L is calculated by integrating the instantaneous luminosity over a period of live time corrected for dead time. The dead time can be caused by many factors, e.g., main ring veto (see section 4.5), DAQ failure and the level 1 prescale for each trigger. Since the instantaneous luminosity varies slowly with time the integration must be performed over sufficiently small time periods during the run. The integrated luminosities were stored into a database for each run. The final value of the integrated luminosity took into account the loss of the data due to reconstruction errors, failure to read events from tapes, etc.

During Run 1A, DØ was able to record a total of 14.9 pb^{-1} out of 27.7 pb^{-1} delivered by the accelerator. The overall efficiency was 54% and the uncertainty of the measured luminosity 5.4%. The main reason for the low efficiency was the main ring veto. For the JET_LOW trigger 82.6 nb^{-1} was accumulated during Run 1A.

6.2 Data Sample

The efficiency of the JET_LOW trigger was greater than 95% for events with at least one jet above E_T=50 GeV [70]. After the offline reconstruction a total of 480,000 events remained. The reconstruction program version 10 was used for this analysis. This data sample included spurious events containing fake jets caused by detector noise and accelerator background. In order to eliminate these fake jets or bad events the jets, events and runs were closely examined as follows.

6.2.1 Bad Data Runs

Data runs between 51132 and 65429 were used for this analysis. A small portion of these runs had systematic failures in the data acquisition system or the detector, e.g., level 2 node problem, BLS problem (see section 4.3.1), etc. Some of the data runs were taken under bad beam environments of the accelerator. Since the occurrence of these problems during data taking could affect the vertex determination from the central detectors or the quality of the calorimeter data, these problematic runs have been removed from the data sample. The special runs for other purposes have also been singled out.

6.2.2 Multiple Interactions

In any beam crossing more than one interaction can occur. The probability of a multiple interaction increases with instantaneous luminosity. At low luminosity the probability of having two hard interactions in a single beam crossing is very small, so most multiple interactions consist of a soft (minimum bias) and a hard scattering. Soft scatterings generate only low E_t jets which do not affect vertex finding. If a distinct primary vertex is reconstructed offline soft scatterings will not change the momenta and positions of jets. Thus soft scatterings are not to be concerned at moderate luminosity. At high luminosity, however, the probability of two hard interactions is not small and it is necessary to eliminate multiple interaction events.

Since the longitudinal size of beam bunches in the Tevatron is 50 cm there is a spread in the time and position of each interaction with respect to the nominal crossing time and the center of the detector. Therefore particles from multiple interactions will have an increased spread in arrival times at the level 0 counters. The standard deviation of the arrival time distribution in each counter was measured and added in quadrature to obtain a total deviation σ_{total}. Depending on the size of this total deviation four multiple interaction flags (MUL_INTF) are defined as follows [74]:

flag 1 :	most likely a single interaction ($\sigma_{total} < 0.4ns$)
flag 2 :	likely a single interaction ($\sigma_{total} < 0.6ns$)
flag 3 :	likely a multiple interaction ($\sigma_{total} > 0.6ns$)
flag 4 :	most likely a multiple interaction ($\sigma_{total} > 1.0ns$)

It was found that the fractional number of events with flag=2 increases with luminosity. It represents that the fraction of multiple interaction events in the combined flag=1 and 2 sample rises with luminosity. In particular, the deviation of the

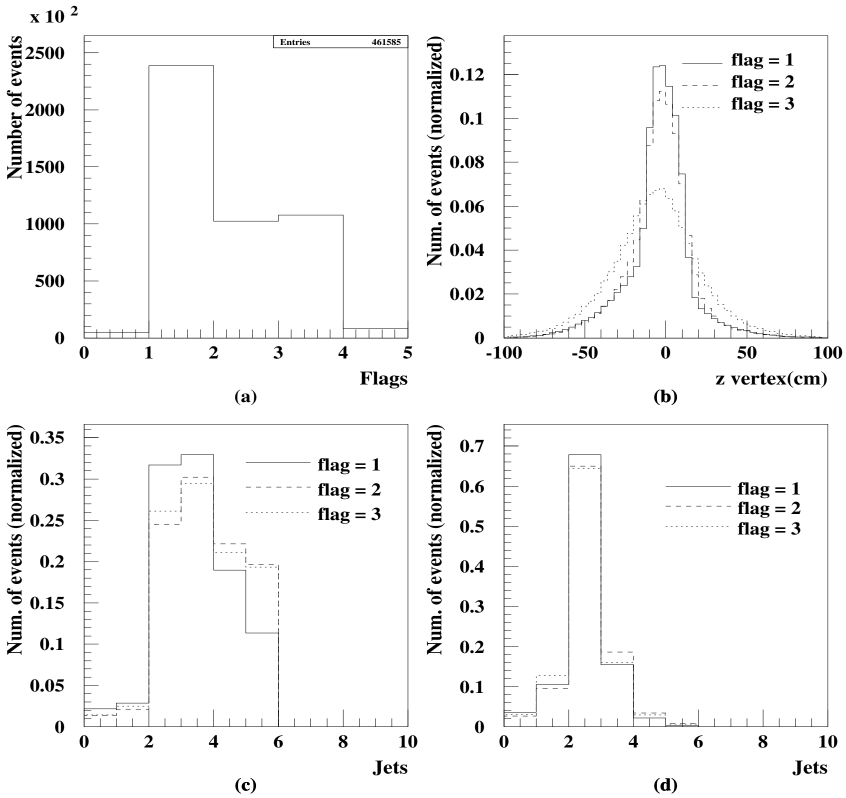

Figure 6.1: (a) Multiple interaction flag (MUL_INTF) distributions for JET_LOW, (b) longitudinal vertex distributions for each flag, (c) number of jets for each flag with $P_T^{min} = 8\text{GeV}$, (d) number of jets for each flag with $P_T^{min} = 20\text{GeV}$.

measured fraction of single interaction events from the expected fraction of single interaction events based on Poisson statistics is noticeable at a luminosity of 5×10^{30} $\text{cm}^{-2}\text{s}^{-1}$ [75].

The multiple interaction tool (MI_TOOL) was designed to improve the efficiency of the multiple interaction flags (MUL_INTF). Instead of using only level 0 information the multiple interaction tool results were determined using the level 0 multiple interaction flag, the level 0 vertex position, the central detectors' vertex determination and the total energy in the calorimeter. The significance of the MI_TOOL flags is identical to that of the multiple interaction flags. This multiple interaction tool has shown reasonable agreement with estimated multiple interaction rates based on Poisson statistics [75].

The average number of interactions per beam crossing depends on the inelastic cross section ($\sigma \sim 47$ mb), beam crossing time (3.5 μs) and instantaneous luminosity as follows:

$$\begin{aligned} \bar{n} &= \mathcal{L}\sigma\tau \\ &= \mathcal{L} \times 0.164 \times 10^{-30}(\mathrm{cm}^2\mathrm{sec}) \end{aligned} \tag{6.2}$$

The typical instantaneous luminosity for the JET_LOW trigger was lower than $\sim 4 \times 10^{30}\mathrm{cm}^{-2}\mathrm{sec}^{-1}$. At this luminosity the average number of interactions is 0.66 which is less than a single interaction. The multiple interaction flag distribution is shown in Fig. 6.1 (a). Approximately 50% of the data is "most likely a single interaction", and 25% is "likely a single interaction". The longitudinal vertex distribution of Fig. 6.1 (b) shows MUL_INTF=1 and 2 have similar vertex position distributions, MUL_INTF=3 has wider vertex distribution. If this wider vertex distribution is due to multiple interactions the distribution for MUL_INTF=2 might have small contamination from multiple interactions as well. The average number of jets ($E_T >$ 8 GeV) increases with MUL_INTF as shown in Fig. 6.1 (c). When 20 GeV minimum transverse momentum is required, however, the average number of jets are similar as shown in Fig. 6.1 (d). It suggests that events containing multiple interactions produce extra low p_t jets, but not high p_t jets. For this analysis only MUL_INTF=1 and 2 events are used.

6.2.3 η Bias Correction

The results of the pseudorapidity bias study described in section 5.4.1 are used to correct the measured pseudorapidity of jets. This pseudorapidity correction, as well as azimuthal angle shift, will be discussed in the section on systematic errors.

6.2.4 Good Jet Quality Cuts

The energy in the calorimeter cells does not always originate from $p\bar{p}$ inelastic scattering. Spurious energy depositions not associated with inelastic scattering can have several origins, e.g. noisy calorimeter cells, electronic noise and main ring energy deposits. The jet trigger and subsequent jet reconstruction algorithm can misidentify this spurious energy as a real jet.

Several cuts have been developed to remove spurious jets [76]. The "fake" jets generally have very different shower shapes or energy profiles in the calorimeter compared to real jets. Several factors related to shower shape are utilized to define good jets:

- **Electromagnetic Fraction Cut (EMF) :** The electromagnetic fraction of a jet is defined as the fraction of jet energy deposited in the electromagnetic calorimeter. The EMF is required to be between 0.05 and 0.95 for good jets in the central and forward region. The upper limit, 0.95, removes misidentified electromagnetic objects, electrons or photons, as well as fake jets due to noisy cells in the electromagnetic calorimeter. The lower limit, 0.05, removes fake jets from noisy cells in the hadronic calorimeter. Since no electromagnetic section was instrumented in the intercryostat region ($1.0 < \eta < 1.6$), the lower EMF cut, 0.05, was not used for the jets in the ICR. The cut efficiency for jets with $E_T = 20$GeV is greater than 99% [77].

- **Hot Cell Fraction Cut (HCF) :** The hot cell fraction is defined as the ratio of the energy between the second most energetic cell of a jet and the most energetic cell. The HCF for good jets is required to be greater than 0.1. This cut was designed to remove fake jets originating in a very energetic noisy cell (hot cell). In the central and forward region, the HCF cut efficiency for jets with $E_T = 20$GeV is greater than 97%. In the intercryostat region it is greater than 95% [77].

- **Coarse Hadronic Fraction Cut (CHF) :** The coarse hadronic fraction is defined as the fraction of jet energy deposited in the coarse hadronic calorimeter. In general most of the energy of a jet is deposited in the electromagnetic and fine hadronic calorimeters. Due to the inefficiencies of the main ring veto counters, however, particles from the main ring can deposit a fair amount of energy in the coarse hadronic calorimeter. This cut is utilized to remove fake jets arising from these main ring particles. The CHF for good jets is defined to be less than 0.4. The cut efficiency for jets with E_T = 20GeV is greater than 99% for all regions [77].

These standard good jet quality cuts remove more than 90% of the fake jets [78] and have a combined efficiency of $\sim$ 97% for central and forward jets with E_T = 20GeV. In the intercryostat region the combined efficiency is around 95% [77].

6.2.5 Energy Scale Correction

After removing spurious jets the jet energies were corrected using the DØ standard jet energy scale correction, version 4.0, as mentioned in section 5.2 which increases jet energy by approximately 15-25%. The overall uncertainty of the energy scale is around 5%. We have also applied the updated energy scale, version 4.2, to the same data samples and checked the effects of different energy scale versions. This will be discussed later.

6.3 Analysis

Before the application of analysis cuts it is worth considering the characteristics of QCD multi-jet events. First, in order to minimize any bias from jet reconstruction inefficiency we have selected jets with E_T greater than 20 GeV. Figure 6.2 (a) is a scatter plot of jets in η and ϕ space. After arranging jets in descending order of transverse energy, the transverse energy, pseudorapidity and azimuthal angle of the first, second and third leading jets are plotted in Fig.6.2 (b), (c), and (d). Leading jets are required to have a minimum transverse energy 50 GeV to remove any trigger bias. The transverse energy distribution of the second leading jets for $E_T > 50$ GeV is similar to that of the leading jets in shape. Since the intercryostat region has poor resolution resulting in more jets around that region the pseudorapidity distribution of leading jets shows bumps in the ICD region. The second and third leading jets show wider pseudorapidity distributions than the leading jets because they have smaller transverse energies.

6.3.1 Analysis Cuts

In QCD physics jets are usually ordered by the magnitude of their transverse energies. In this analysis, however, we ordered jets by pseudorapidity. We start with the clean jet, energy corrected event samples and apply the following conditions:

- $\boldsymbol{E_T^{minimum}} = \mathbf{20\ GeV}$ **:** Jets are required to have a minimum E_T of 20 GeV. This threshold is the lowest transverse energy accessible without any reconstruction inefficiency (or bias).

- $\boldsymbol{|\eta_d^{jet}| < 3.0}$ **:** Since trigger towers were implemented for $|\eta_d| \leq 3.2$, jets of $|\eta_d| < 3.0$ are selected to remove any trigger edge effect. (η_d is the pseudorapidity defined in the detector units.)

- $\boldsymbol{\eta}$ **ordering :** After the above cuts are applied, we select events consisting of at least two jets and order those jets in pseudorapidity. Then we tag two jets with the largest pseudorapidity separation. For convenience we name these tagging jets : **jet 1** and **jet 2** referring to the **most forward** and the **most backward** jets in pseudorapidity.

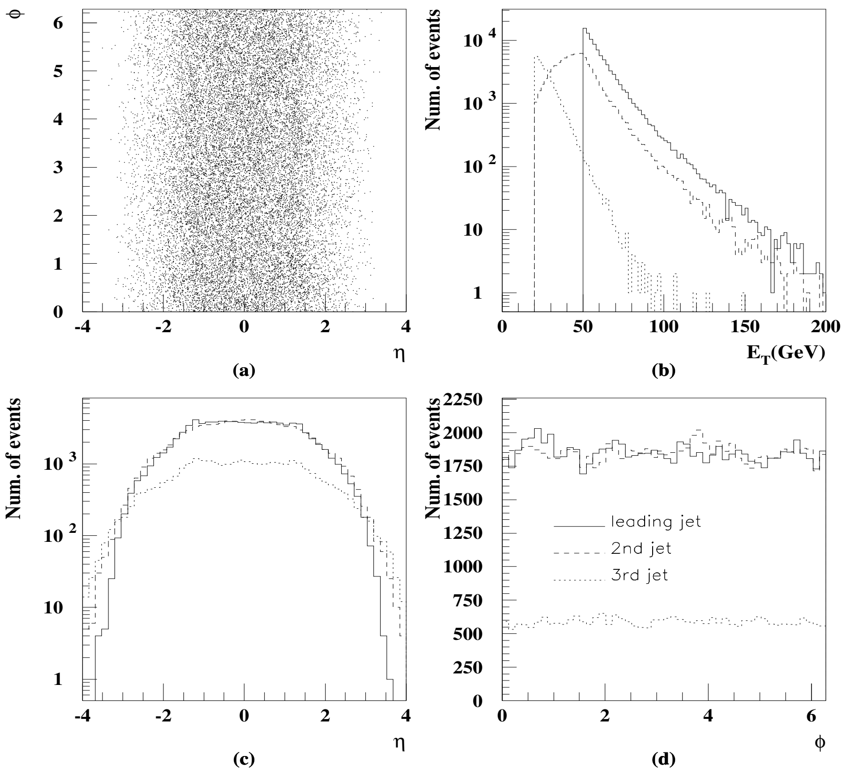

Figure 6.2: (a) The distribution of jets in η and ϕ space, (b) transverse energy, (c) pseudorapidity, (d) azimuthal angle distributions of the leading, 2nd, and 3rd jets after ordering in E_T.

- $\boldsymbol{E_T^{forward} > 50}$ **GeV or** $\boldsymbol{E_T^{backward} > 50}$ **GeV :** One of the two tagging jets must satisfy the JET_LOW trigger condition E_T >50 GeV to avoid any trigger bias.

Using the two tagged jets we defined two variables, the rapidity interval $\Delta\eta$ and the azimuthal angle difference $\Delta\phi$ as follows:

$$\Delta\eta = \eta_{forward} - \eta_{backward} \tag{6.3}$$

$$\Delta\phi = \phi_{forward} - \phi_{backward} \tag{6.4}$$

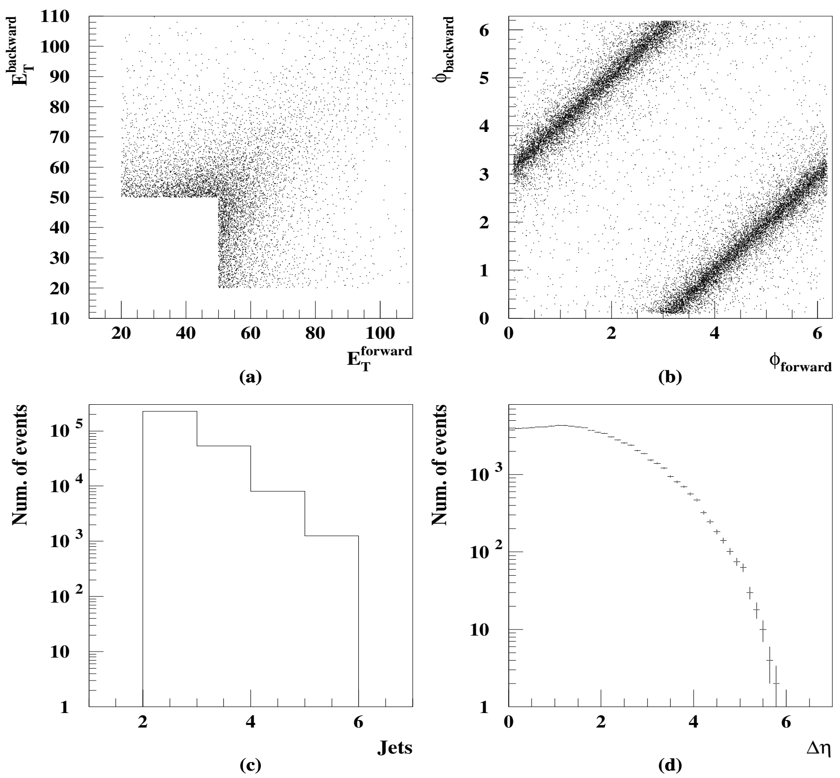

Figure 6.3: (a) The scatter plot of the two tagging jets for E_T and b) for azimuthal angle ϕ, c) jet multiplicity distribution, d) the distribution of rapidity interval ($\Delta\eta = \eta_{forward} - \eta_{backward}$) between the two tagging jets.

By definition, $\Delta\eta$ is always greater than zero.

The transverse momenta of the two tagging jets are plotted in Fig. 6.3 (a) in which the boundaries at the minimum transverse momentum, 20 GeV, and trigger threshold, 50 GeV, are clearly shown. The azimuthal angle distribution of the two tagging jets is plotted in Fig. 6.3 (b). The two dark strips show that most of the tagged jets are back-to-back in the transverse plane. The jet multiplicity is plotted in Fig 6.3 (c). The distribution of the rapidity interval $\Delta\eta$ shown in Fig. 6.3 demonstrates the wide coverage of the DØ calorimeter which extends to $\Delta\eta$=6.

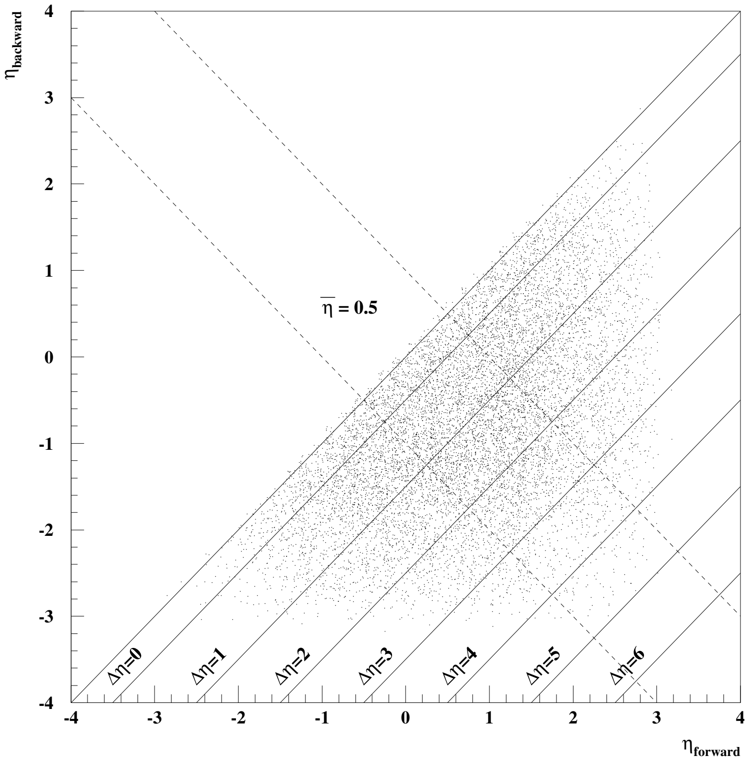

Figure 6.4: The scatter plot of the two tagging jets in η space.

As shown in Fig. 6.4 the $\Delta\eta = 0$ bin is defined to be $0 < \Delta\eta < 0.5$ and the $\Delta\eta = 1$ bin to be $0.5 < \Delta\eta < 1.5$ and so on. Due to the detector pseudorapidity cut, $|\eta_d^{jet}| < 3.0$, there are few events in $\Delta\eta = 6$ bin. The dashed lines represent the boundaries for the pseudorapidity boost $\bar{\eta} = 0.5$ where pseudorapidity boost is defined as follows:

$$\bar{\eta} = \left|\frac{\eta_1 + \eta_2}{2}\right| \tag{6.5}$$

The jet cross sections are the convolution of the matrix elements and the parton distribution functions which are not well known in the region where parton momentum fraction x is small. In order to minimize the effect from the uncertainty of the parton distribution functions in the small x region and to improve theoretical predictions, the boost cut, $\bar{\eta} \leq 0.5$, is theoretically motivated. This cut forces the parton momentum fraction, $x = \frac{2P_T}{\sqrt{s}} \cosh(\eta)$, to be large such that the parton distribution function is described by the standard DGLAP evolution [45].

However, the smallest x available with our event configuration, $E_T > 20$ GeV and $|\eta| < 3.0$, is 0.0019 which is not exceedingly small. Therefore the rapidity boost cut is not necessary for the present event configuration. If a smaller transverse energy threshold or wider pseudorapidity region is used the small $x(< 10^{-4})$ region in the parton distribution functions is accessible and the rapidity boost cut is necessary to obtain a valid prediction. Even though we do not use the boost cut for the final conclusion we will show the effect of the rapidity boost cut on this analysis since the rapidity boost cut is important for future analysis with wider rapidity coverage and lower minimum transverse momentum.

6.3.2 Characteristics of two tagged jets

The data were divided into six subsets from $\Delta\eta = 0$ to 5. The last bin $\Delta\eta$=5 ($4.5 < \Delta\eta < 5.5$) contains 518 events. The jet multiplicities in each subset are plotted in Fig. 6.5. As the rapidity interval increases there is more phase space for extra radiation and it is natural for the average jet multiplicity to increase. It seems there is linear relationship between rapidity interval and the average jet multiplicity as shown in Fig. 6.6 (a). An increase of approximately 0.2 jets per rapidity interval can be observed for $1 < \Delta\eta < 4$.

Figure 6.6 (c) shows a similar increase in the average multiplicity when the $\bar{\eta} = 0.5$ cut is applied. The average jet multiplicity is independent of the $\bar{\eta}$ cut. The forward jet E_T distributions for $\Delta\eta$=1, 3 and 5 bins are shown in Fig. 6.6 (b) and (d) with and without the $\bar{\eta}$ cut. The E_T distributions above the trigger threshold, 50 GeV, are typical and fall quickly as the rapidity interval increases. The error bars indicate statistical errors only.

The rapidity distributions of the two tagging jets are shown in Fig. 6.7 as a

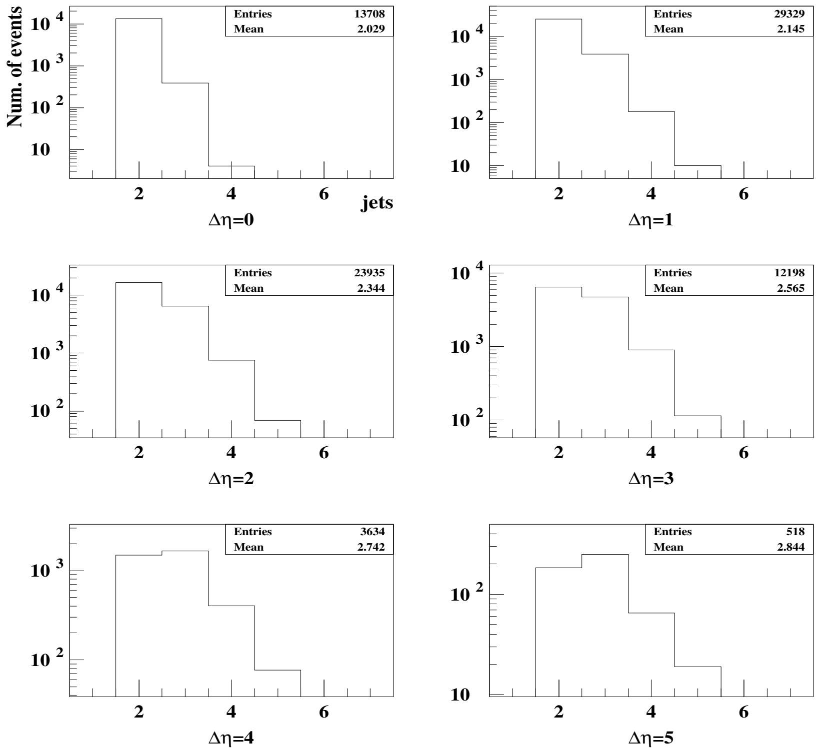

Figure 6.5: Jet multiplicity distribution for various bins of rapidity interval (no $\bar{\eta}$ cut is applied).

function of the rapidity interval. The solid lines represent the two tagging jets without the $\bar{\eta}$ cut and the dotted lines with the $\bar{\eta}$ cut. Jet 1 is the forward jet and jet 2 the backward jet. As can be seen the $\bar{\eta}$ cut removes many events with high rapidity jets in small rapidity intervals. However, in bins sensitive to statistics, for instance $\Delta\eta$=5, only 14% of the data were removed by the $\bar{\eta}$ cut.

6.3.3 $< \cos[n(\pi - \Delta\phi)] >$

Since the asymmetric nature of the E_T cuts on the two tagging jets (20 GeV and 50 GeV) tends to increase the probability of at least one additional radiation, the

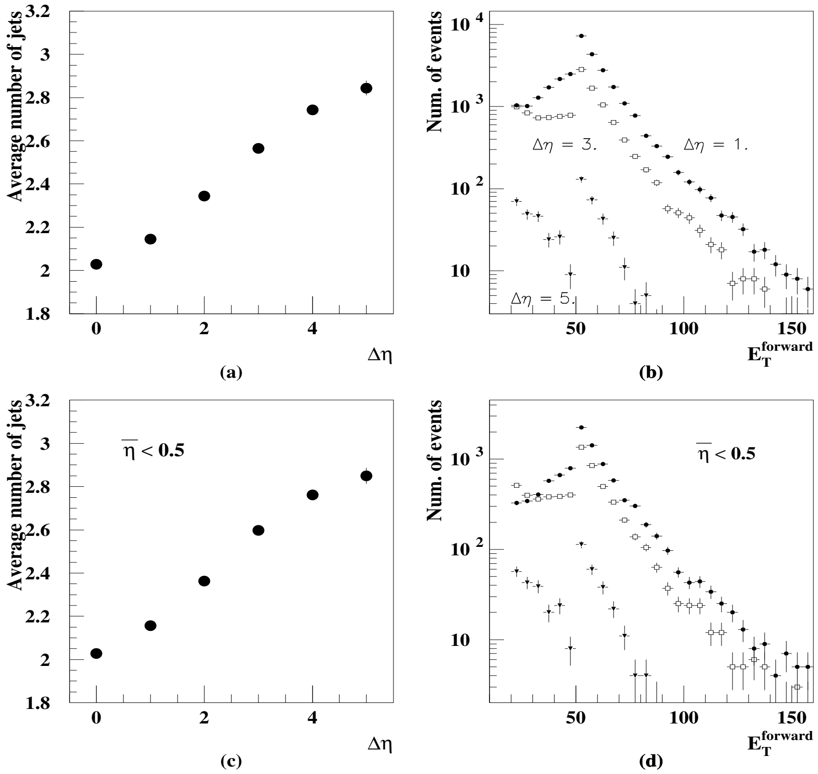

Figure 6.6: (a) Average jet multiplicity distribution, (b) forward jet E_T distributions for $\Delta\eta = 1$, 3, and 5 bins. (c) Average jet multiplicity distribution, (d) forward jet E_T distributions for $\Delta\eta = 1$, 3, and 5 bins with $\bar{\eta} \leq 0.5$.

decorrelation between the two tagging jets would be enhanced by this cut as well as any minijet activity. However, due to trigger bias no symmetric E_T cut is possible, so we can not isolate the effect of this asymmetry E_T cut. This asymmetric effect will be discussed in detail in the Monte Carlo section.

The azimuthal angle differences $\Delta\phi$ are plotted in Fig. 6.8 (a) which shows normalized $\Delta\phi$ distributions for $\Delta\eta$=1, 3 and 5. The sharp peaks at $\Delta\phi = \pi$ indicate that the two jets most separated in pseudorapidity are highly correlated with each other. As the rapidity separation between the two jets increases, however,

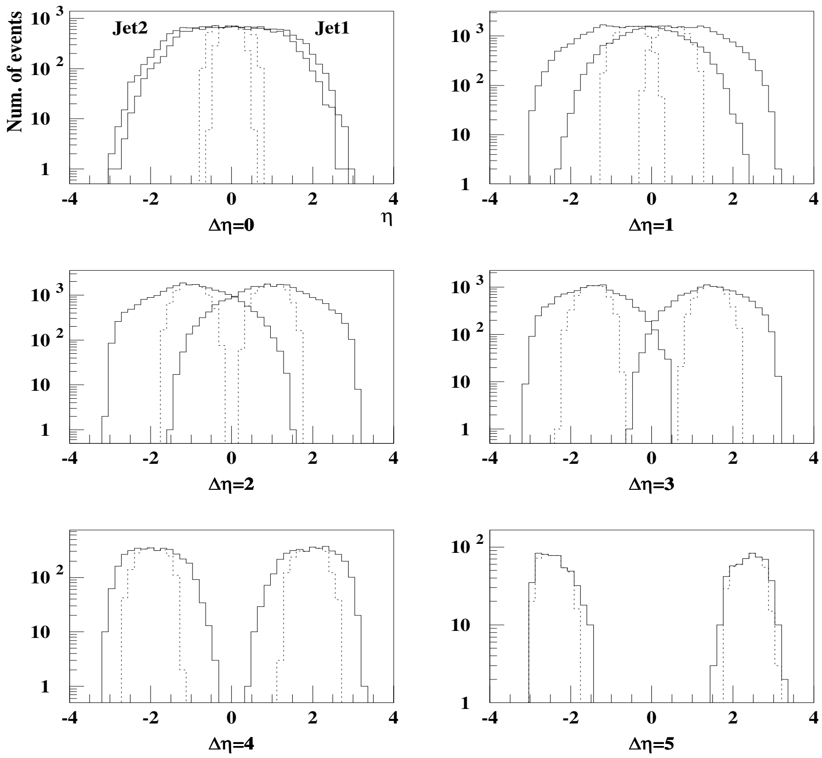

Figure 6.7: Pseudorapidity distributions of the two tagging jets, forward jet (jet 1) and backward jet (jet 2), as a function of rapidity intervals: Solid lines are for no rapidity boost cut and the dotted lines for rapidity boost cut.

the peaks of the $\Delta\phi$ distributions decrease and the widths increase indicating a loss in correlation. The same type of correlation loss can be seen in Fig. 6.8(b) with the $\bar{\eta}$ cut.

In Fig. 6.8 (a) and (b) the decorrelation effects are shown only qualitatively. In order to express the decorrelation effect quantitatively we use $\cos[n(\pi - \Delta\phi)]$ and calculate its average as a function of $\Delta\eta$. The results are shown in Fig. 6.9 for the first and second moments n=1 and 2. Since $< \cos(\pi - \Delta\phi) > = 1$ would occur for perfect correlation and $< \cos(\pi - \Delta\phi) > = 0$ for perfect decorrelation between the

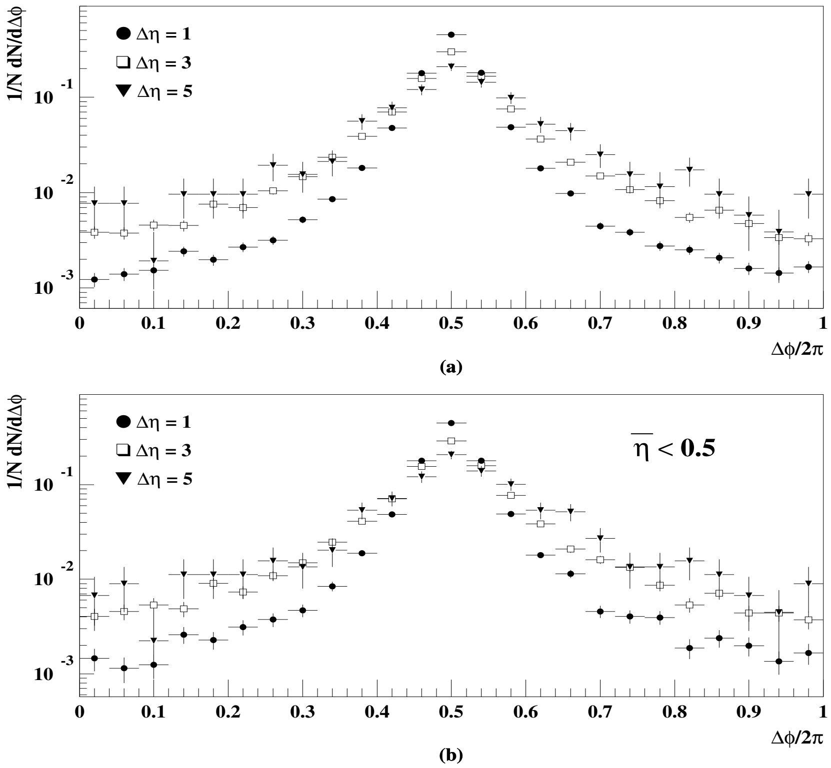

Figure 6.8: (a) Azimuthal angle difference, $\Delta\phi = \phi_{forward} - \phi_{backward}$, for various rapidity intervals, 1, 3 and 5, without the $\bar{\eta}$ cut, (b) with the $\bar{\eta}$ cut. The distributions are normalized to unit area.

two jets the slope in the plot represents the increase in decorrelation as a function of rapidity interval.

In Fig. 6.9 the average values of $\Delta\eta$ in each bin are used for the abscissa and only statistical errors are presented. It appears that the cosine average values decrease linearly as the rapidity interval increases. Or, in other words, the azimuthal decorrelation between the two tagging jets increases as a function of the rapidity interval. The second moment shows a steeper slope than the first moment. When the $\bar{\eta}$=0.5 cut is applied, the overall $< \cos(\pi - \Delta\phi) >$ values barely change except in the $\Delta\eta$

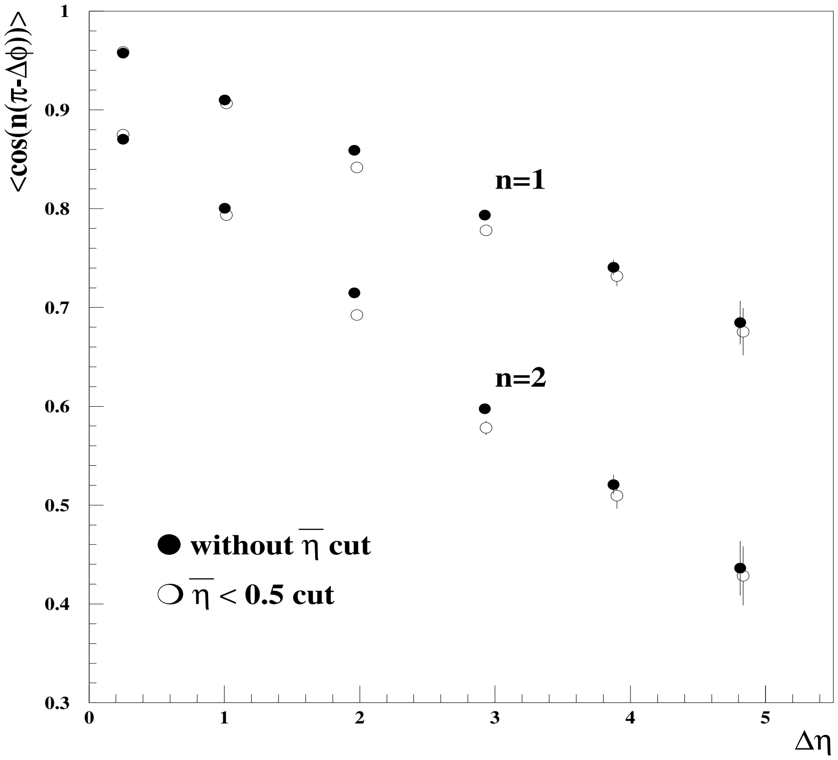

Figure 6.9: Average values of the correlation variables $\cos[n(\pi - \Delta\phi)]$ versus $\Delta\eta$ for the first moment $n = 1$ and second moment $n = 2$.

= 2 and 3 bins which contain surplus ICD jets due to poor energy resolution. In case some of the low E_T jets are identified as higher E_T jets the decorrelation effect may increase. The data values from Fig. 6.9 are listed in Table 6.1

$\Delta\eta$	0.25	1	2	3	4	5
no $\bar{\eta}$						
$< \Delta\eta >$	0.2532	1.0025	1.9596	2.9229	3.8758	4.8118
$< \cos(\pi - \Delta\phi) >$	0.9576	0.9102	0.8590	0.7934	0.7406	0.6847
Stat. Error n=1	0.0012	0.0016	0.0022	0.0037	0.0076	0.0219
$< \cos 2(\pi - \Delta\phi) >$	0.8704	0.8004	0.7147	0.5974	0.5209	0.4361
Stat. Error n=2	0.0024	0.0023	0.0031	0.0051	0.0100	0.0277
$\bar{\eta} = 0.5$						
$< \Delta\eta >$	0.2525	1.0165	1.9794	2.9323	3.9015	4.8333
$< \cos(\pi - \Delta\phi) >$	0.9588	0.9065	0.8419	0.7779	0.7319	0.6755
Stat. Error n=1	0.0021	0.0028	0.0036	0.0055	0.0101	0.0240
$< \cos 2(\pi - \Delta\phi) >$	0.8748	0.7934	0.6924	0.5784	0.5094	0.4285
Stat. Error n=2	0.0042	0.0041	0.0049	0.0073	0.0129	0.0299

Table 6.1: Average values of the correlation variables, $\cos[n(\pi - \Delta\phi)]$, versus $\Delta\eta$ for the first moment $n = 1$ and second moment $n = 2$ with their statistical errors. See Fig. 6.9.

Chapter 7

Systematics

Until now, we have considered only statistical errors. In this chapter, we will investigate several systematic factors which could affect the results of this analysis. The systematic biases to be studied are : the uncertainty in the jet energy scale correction, the finite energy and position resolution of the calorimeter, the offline cuts to remove fake jets, and biases due to the jet reconstruction algorithm. These effects could alter the transverse momentum and position of a jet and sometimes deform a jet event by producing fake jets or removing good jets.

7.1 Jet Energy Scale Uncertainty

7.1.1 Jet Energy Scale V4.0

As described in section 5.2, the jet energy scale carries its own uncertainty due to statistical variations and systematic errors. Since the statistical uncertainty is small, most of the error stems from various systematic biases. In Fig. 5.1 the central curve represents the nominal energy scale and the uncertainty is given by the *high* and *low* energy bands which are about $\pm 5\%$ relative to nominal for the whole energy range. The mismeasurement of jet transverse momentum can affect this azimuthal

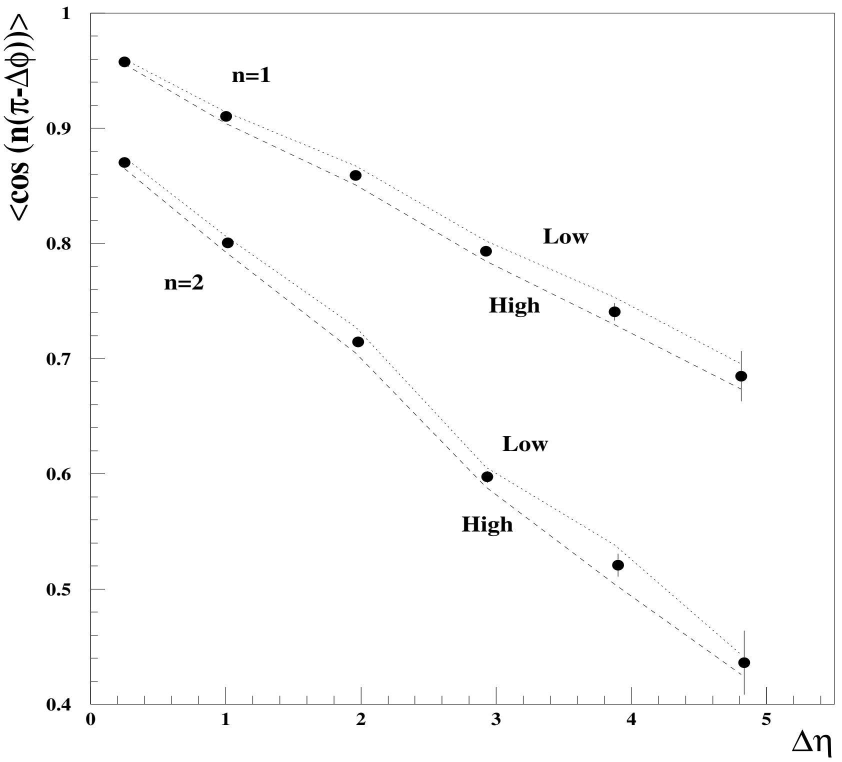

Figure 7.1: The dotted lines represent $< \cos[n(\pi - \Delta\phi)] >$ with the low jet energy scale correction, the dashed lines for the high energy correction, and the solid circles for the nominal values. Only statistical errors are shown.

angle decorrelation study by inserting mismeasured jets into an event. If an 18 GeV jet, for example, is reconstructed as a 21 GeV jet there is a possibility it will be a tagging jet and result in a wrong rapidity interval and wrong azimuthal angle difference, depending on the position of the reconstructed jet.

In order to study the influence of the jet energy scale uncertainty the averages of $\cos(\pi - \Delta\phi)$ are calculated using jets corrected by the *high* and *low* energy scales. The results are shown in Fig 7.1. With the *low* energy scale the averages of $\cos(\pi - \Delta\phi)$ are slightly less decorrelated in all $\Delta\eta$ bins since a smaller number of jets in each event satisfy the minimum transverse momentum or trigger threshold requirements. On the other hand, the averages of $\cos(\pi - \Delta\phi)$ with the *high* energy scale show increased decorrelation. The difference between the nominal $< \cos(\pi - \Delta\phi) >$ values and the values obtained using the low and high jet energy scale is taken as the systematic error on $< \cos(\pi - \Delta\phi) >$ due to the jet energy scale uncertainty. This systematic error dominates for all $\Delta\eta$ except $\Delta\eta = 5$ where the statistical error is dominant. This result and other systematic errors are shown in Fig. 7.7.

7.1.2 Out-of-Cone Showering Correction

The jet energy scale depends on the pseudorapidity of a jet in addition to the transverse momentum. As shown in Fig. 7.2, the jet energy scale is nearly constant for $|\eta| < 2.5$ except in the ICD region, $1.0 < |\eta| < 1.6$. The sharp rise of the correction scale beyond $\eta = 2.5$ is a combined effect of *out-of-cone showering* and *enhanced gluon radiation* in the forward region.

The physical tower size in the calorimeter is a function of pseudorapidity (see Fig. 4.4) and consequently the forward calorimeter towers are physically smaller than their central counterparts. Therefore the energy of particles inside a cone of $R = 0.7$ in the forward calorimeter can smear out-of-the cone through hadronic or electromagnetic showering. This out-of-cone showering accounts for approximately 50% of the sharp increase. The rest of the increase is due to enhanced soft radiation in the forward region [83]. Suppose there is a parton of E_T=20 GeV in the forward region, η=3, balanced with another parton of E_T=20 GeV in the central region, η=1. The forward parton has much higher energy and consequently has a higher probability to radiate gluons. This radiation loss mimics out-of-cone showering. However, this radiation is a physical process and should not be considered in the energy calibration.

Since the calibration of forward jets was done using the dijet balance method described in section 5.2 and due to the lack of Monte Carlo data we are unable to

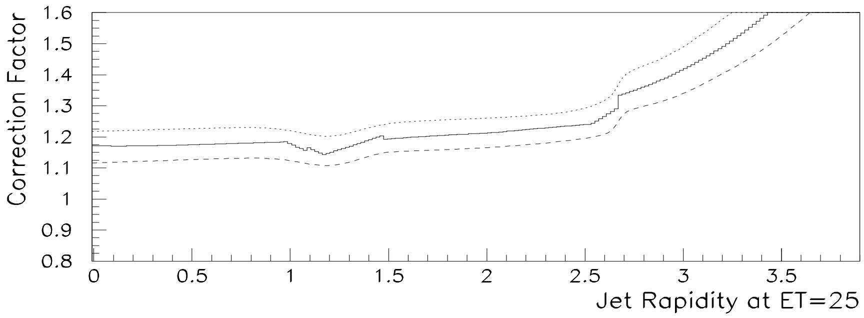

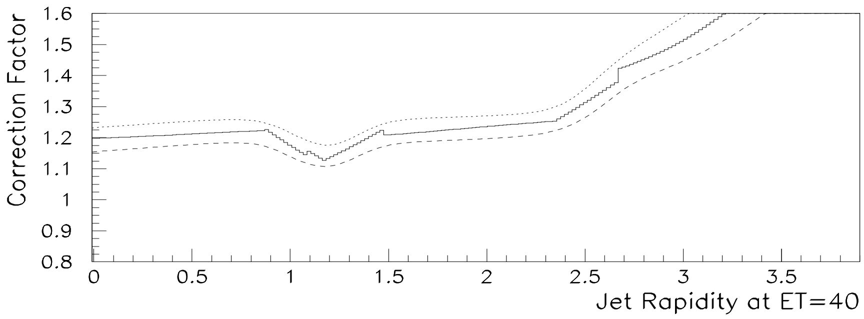

Figure 7.2: The jet energy scale correction as a function of pseudorapidity at fixed transverse momenta, 25 GeV and 40 GeV.

separate the out-of-cone showering and enhanced radiation effects. Thus at large rapidity the jet energy scale of Fig. 7.2 may be overestimated resulting in an increased number of jets above a threshold. Since the excess forward jets could alter the correlation between two tagging jets we also calculated the averages of $\cos(\pi - \Delta\phi)$ by turning off the out-of-cone showering correction. The systematic uncertainty due to the out-of-cone showering is given by the difference between the cosine averages with and without the out-of-cone correction. The result is shown in Fig. 7.7.

7.2 Intercryostat Detector Region

The intercryostat detector region has worse energy resolution $\sim \frac{120}{\sqrt{E}}\%$ than the central and forward regions $\sim \frac{80}{\sqrt{E}}\%$. Due to this degraded resolution an excess

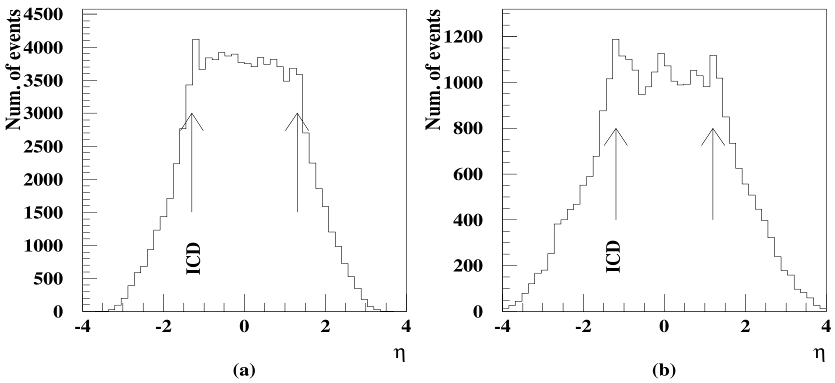

Figure 7.3: The pseudorapidity distribution for, (a) the leading jets and (b), the second leading jets ($E_T > 20$ GeV). Note the excess in the ICR.

number of jets were reconstructed in the ICD region. Figures 7.3 (a) and (b) show the pseudorapidity distributions of the leading jets and the second leading jets, respectively. The bumps in the ICD region are clearly distinguishable and represent additional jets reconstructed in the region.

Since the GEANT detector simulation does not simulate this excess we estimate the effects of this excess on $< \cos(\pi - \Delta\phi) >$ by using smearing method that uses the jet energy resolution obtained in section 5.3. Parton jets were generated by the HERWIG Monte Carlo and the energy of those jets was smeared using the parameterized functions of the DØ jet energy resolution. The average of $\cos(\pi - \Delta\phi)$ is calculated using these smeared jets. Then the parton jets were smeared using the same energy resolutions except that the ICD jet resolution was replaced by the central jet resolution and the average of $\cos(\pi - \Delta\phi)$ is calculated. The difference between the above two $< \cos(\pi - \Delta\phi) >$ values is taken as the systematic uncertainty due to the excess jets in the ICD region. This difference is plotted in Fig. 7.7.

Since the systematic uncertainties in the $\Delta\eta = 4$ and 5 bins are very important, as one way of double checking, the influence of excess ICD jets in these high $\Delta\eta$ bins was estimated by removing all the jets in $1.0 < |\eta| < 1.6$ and calculating the

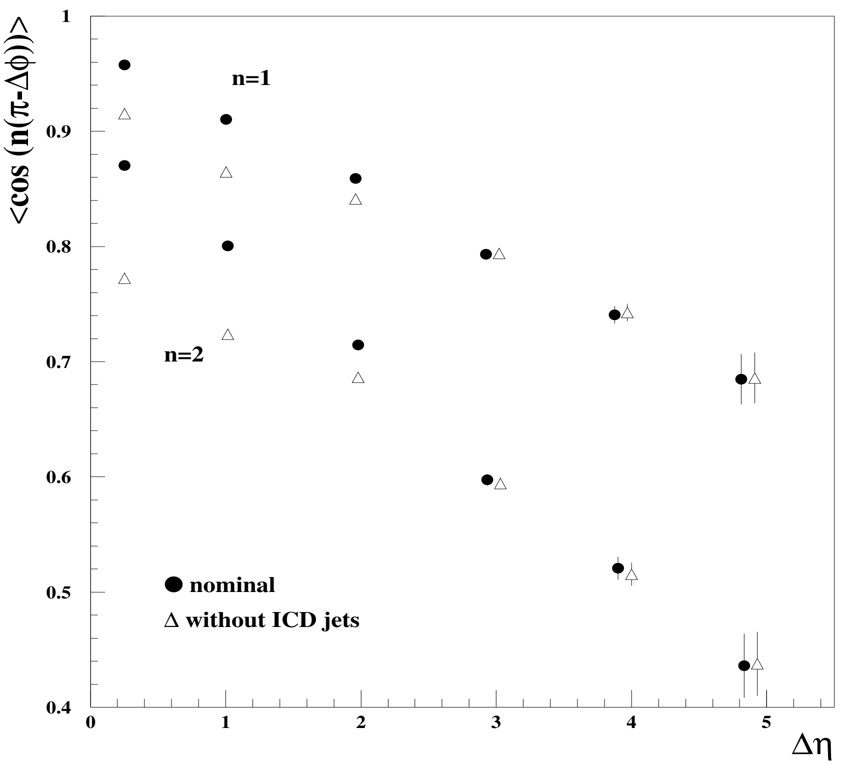

Figure 7.4: The solid circle represent the average of $\cos(\pi - \Delta\phi)$ with ICR jets, and the open triangles without ICR jets.

averages of $\cos(\pi - \Delta\phi)$. As shown in Fig 7.4 the removal of all ICD jets affects the averages of $\cos(\pi - \Delta\phi)$ for $\Delta\eta < 3$, but not in $\Delta\eta = 4$ and 5 bins as we expected. If one of two tagging jets is in the ICD region the event will most probably have a small rapidity interval. Therefore $\Delta\eta = 4$ and 5 bins are found to be very insensitive to additional ICD jets and as can be noticed the effect of removing all ICD jets in the high rapidity interval bins is less than that of the energy resolution smearing described above.

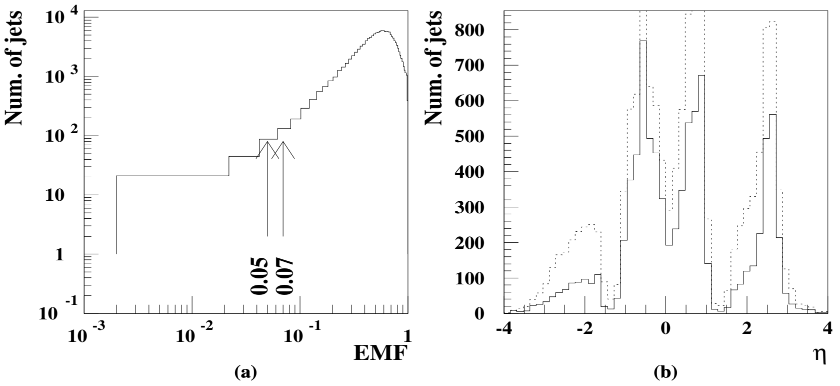

Figure 7.5: (a) The distribution of the electromagnetic fraction (EMF) after the hot cell fraction (HCF) cut and the coarse hadronic fraction (CHF) cut are applied. (b) The solid line represents the jets removed with the $0.05 < \text{EMF} < 0.95$ requirement, and the dotted line with $0.07 < \text{EMF} < 0.92$.

7.3 Good Jet Quality Cut

As mentioned in section 6.2.4 the standard good jet quality cuts remove more than 90% of fake jets and keep 97% of the good jets for the central and forward regions, and 95% for the intercryostat regions when their transverse momenta are around 20 GeV. Even though the influence of the good jet cuts on this analysis are expected to be negligible, if the efficiency of the quality cut depends on the pseudorapidity of the jets, the cut can affect the $< \cos(\pi - \Delta\phi) >$ values at the large pseudorapidity interval.

When we tighten the good jet criteria, for example, from $0.05 < \text{EMF} < 0.95$ to $0.07 < \text{EMF} < 0.92$ (see Fig. 7.5 (a)) the number of removed jets doubles as shown in Fig. 7.5(b). On the average the pseudorapidity and transverse momentum distributions for the jets lost with the standard EMF cut are similar to the distributions for the tight EMF cut. In a similar way the CHF (< 0.4) and HCF (< 10) cuts are also tightened to $\text{CHF} < 0.32$ and $\text{HCF} < 8$ respectively. By comparing

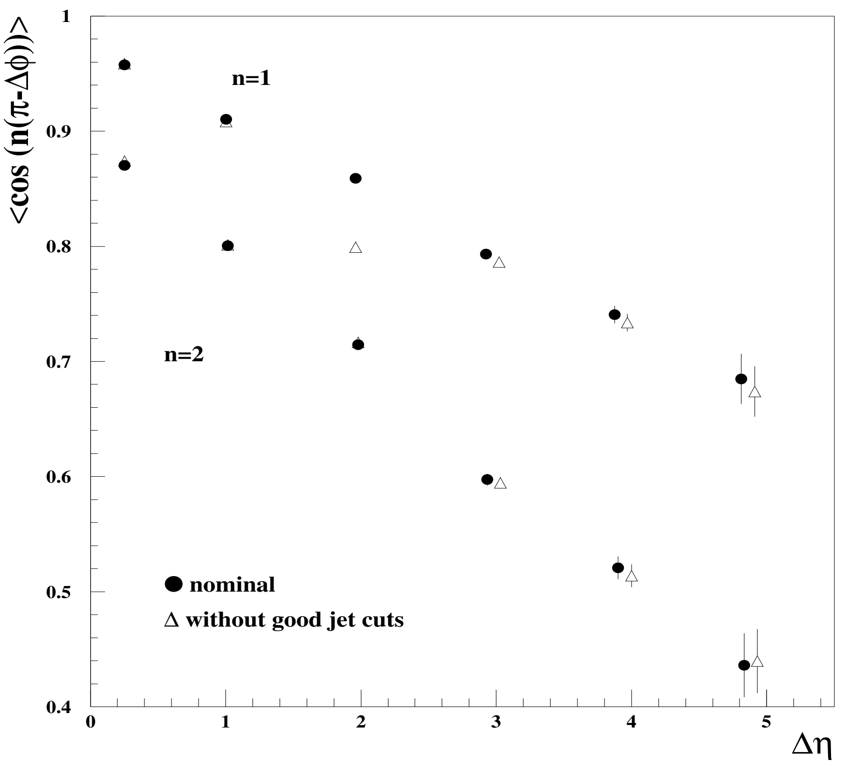

Figure 7.6: The solid circles represent the average of $\cos(\pi - \Delta\phi)$ with the standard good jet cuts, and the open triangles without those cuts.

the $< \cos(\pi - \Delta\phi) >$ values from the standard cuts to those from the tight cuts we estimate systematic errors from the good jet quality cuts. Since the portion of good jets removed by the standard cuts is much smaller than by the tight cuts these errors are conservative.

We have also calculated $< \cos(\pi - \Delta\phi) >$ without any quality cuts and compared these to the nominal values as shown in Fig. 7.6. This plot shows how fake jets affect azimuthal correlations between the two tagging jets. Specifically two hot cell spots at pseudorapidity 1 and 2.6 with the same azimuthal angles, 4.75 radian, deform the distribution of the azimuthal angle difference for the $\Delta\eta = 2$ bin and change the average of $\cos(\pi - \Delta\phi)$. This is a good examples of the importance and credibility of the good jet quality cuts. These results are also shown in Fig. 7.7.

7.4 Jet Position Biases and Resolutions

In section 5.4 we obtained the position biases and position resolutions from a Monte Carlo simulation. The results are utilized in this section to calculate systematic biases on $< \cos(\pi - \Delta\phi) >$.

7.4.1 Position Biases

In order to calculate systematic errors stemming from the η and ϕ biases we calculate the averages of $\cos(\pi - \Delta\phi)$ with and without the η and ϕ bias corrections. The variations in $< \cos(\pi - \Delta\phi) >$ due to these biases are found to be small as shown in Fig. 7.7.

7.4.2 Position resolution

The η resolution for jets is around 0.03. Due to this resolution, events can migrate between $\Delta\eta$ bins. In order to study the magnitude of this effect we have generated parton level event samples using the HERWIG event generator and smeared the pseudorapidity of each jet using the resolution functions obtained in section 5.4. The averages of $\cos(\pi - \Delta\phi)$ before smearing are compared to the averages after smearing. The ϕ resolution for jets is also ~ 0.03. The same procedure has been performed for azimuthal angles and the results are shown in Fig. 7.7 The systematic errors due to the uncertainty in the position measurements are very small compared to other uncertainties.

7.5 Summary

The results of the systematic error studies are listed in Table 7.1 and 7.2 for the first moment and the second moment and plotted in Fig. 7.7 for the first moment n=1. The dotted lines in Fig. 7.7 represent the statistical errors and the solid lines (or hatched area) the systematic errors for the *low* and *high* energy scales. For the other biases we have subtracted the nominal $< \cos(\pi - \Delta\phi) >$ values from the biased $< \cos(\pi - \Delta\phi) >$ values and show the differences with the solid circles. The systematics from the energy scale uncertainty dominate all rapidity intervals except $\Delta\eta = 5$ where statistical error dominates. Among the other uncertainties, the errors calculated by tightening the standard good jet cuts are dominant.

We separate these systematic errors as follows:

- **Systematic uncertainties related to the energy scale :** The errors stemming from the low and high energy scales and the errors from the out-of-cone correction are added in quadrature and the combined errors are called *the systematic uncertainty related to the energy scale uncertainty* for $< \cos(\pi - \Delta\phi) >$. The larger errors between low energy scale and high energy scale uncertainties are used in the quadratic sum.

- **Other systematic uncertainties :** All other uncertainties related to ICR smearing, good jet cuts, position biases and finite resolutions are added in quadrature as *systematic errors not related to the energy scale.* The differences obtained by removing all ICD jets or the good jet cuts are not used in this error calculation. As mentioned in the above sections they were performed as a way of double checking the high $\Delta\eta$ bins and were already estimated using the ICR smearing and tightening the good jet quality cuts.

n=1						
$\Delta\eta$	0.25	1	2	3	4	5
Stat. error	0.0012	0.0016	0.0022	0.0037	0.0076	0.0219
Energy scale related						
High Escale	-0.0021	-0.0062	-0.0083	-0.0089	-0.0112	-0.0111
Low Escale	0.0023	0.0039	0.0084	0.0087	0.0125	0.0108
Out-of-cone corr.	-0.0011	-0.0015	-0.0031	-0.0044	-0.0022	-0.0058
Other systematics						
ICR smearing	-0.0016	-0.0006	-0.0018	0.0000	0.0034	0.0023
$2 *$ good jet cut	-0.0031	-0.0040	-0.0009	-0.0009	0.0039	-0.0072
η bias	-0.0003	-0.0008	-0.0006	0.0005	-0.0020	-0.0023
ϕ bias	0.0000	0.0000	0.0000	0.0000	0.0000	0.0000
η smearing	-0.0002	-0.0002	0.0011	-0.0002	0.0036	0.0003
ϕ smearing	-0.0006	-0.0006	-0.0003	-0.0005	-0.0009	0.0001
Double checking for high $\Delta\eta$						
No ICR	-0.0422	-0.0455	-0.0178	0.0004	0.0020	0.0012
No good jet cut	0.0010	-0.0018	-0.0599	-0.0070	-0.0070	-0.0108

Table 7.1: The lists of statistical errors and the differences between $< \cos(\pi - \Delta\phi) >_{extremes} - < \cos(\pi - \Delta\phi) >_{nominal}$ for the first moment n=1. See text for details.

n=2						
$\Delta\eta$	0.25	1	2	3	4	5
Stat. error	0.0024	0.0023	0.0031	0.0051	0.0100	0.0277
Energy scale related						
High Escale	-0.0055	-0.0081	-0.0096	-0.0090	-0.0167	-0.0102
Low Escale	0.0042	0.0057	0.0128	0.0082	0.0175	0.0068
Out-of-cone corr.	-0.0029	-0.0026	-0.0019	-0.0009	-0.0002	0.0042
Other systematics						
ICR smearing	-0.0016	-0.0006	-0.0018	0.0000	0.0034	0.0023
$2 *$ good jet cut	-0.0072	-0.0061	-0.0031	-0.0017	0.0006	-0.0039
η bias	-0.0004	-0.0013	-0.0005	-0.0015	-0.0050	0.0047
ϕ bias	0.0000	0.0000	0.0000	0.0000	0.0000	0.0000
η smearing	-0.0001	-0.0002	0.0011	-0.0005	0.0047	-0.0044
ϕ smearing	-0.0019	-0.0018	-0.0014	-0.0011	-0.0023	0.0006
Double checking for high $\Delta\eta$						
No ICR	-0.0979	-0.0765	-0.0281	-0.0031	-0.0054	0.0017
No good jet cut	0.0034	0.0007	0.0018	-0.0030	-0.0071	0.0036

Table 7.2: The lists of statistical errors and the differences between $< \cos 2(\pi - \Delta\phi) >_{extremes} - < \cos 2(\pi - \Delta\phi) >_{nominal}$ for the first moment n=2. See text for details.

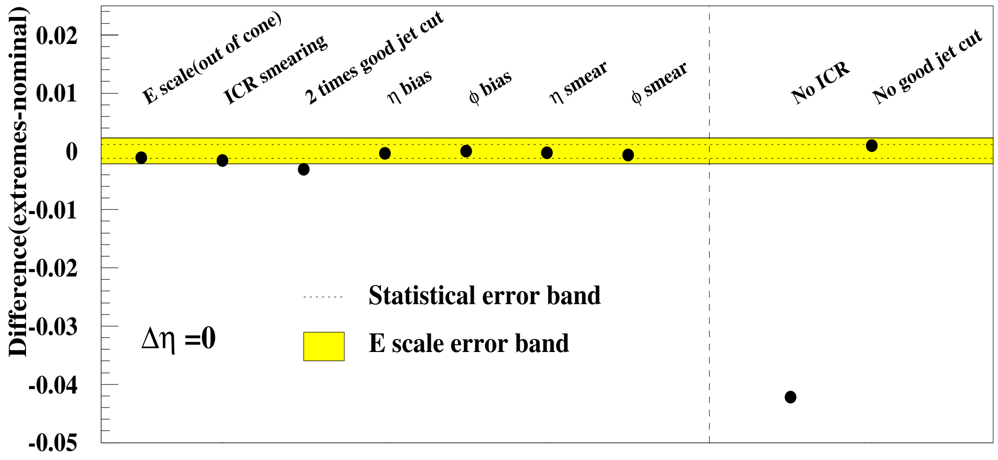

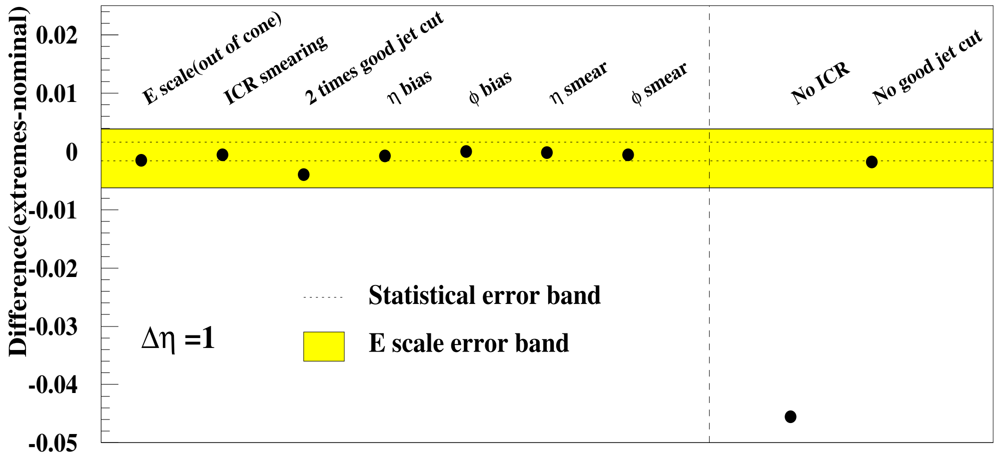

Figure 7.7: The comparison of the systematic errors for $\Delta\eta = 0$ through 5 (n=1). See text for details. (continues in the next page).

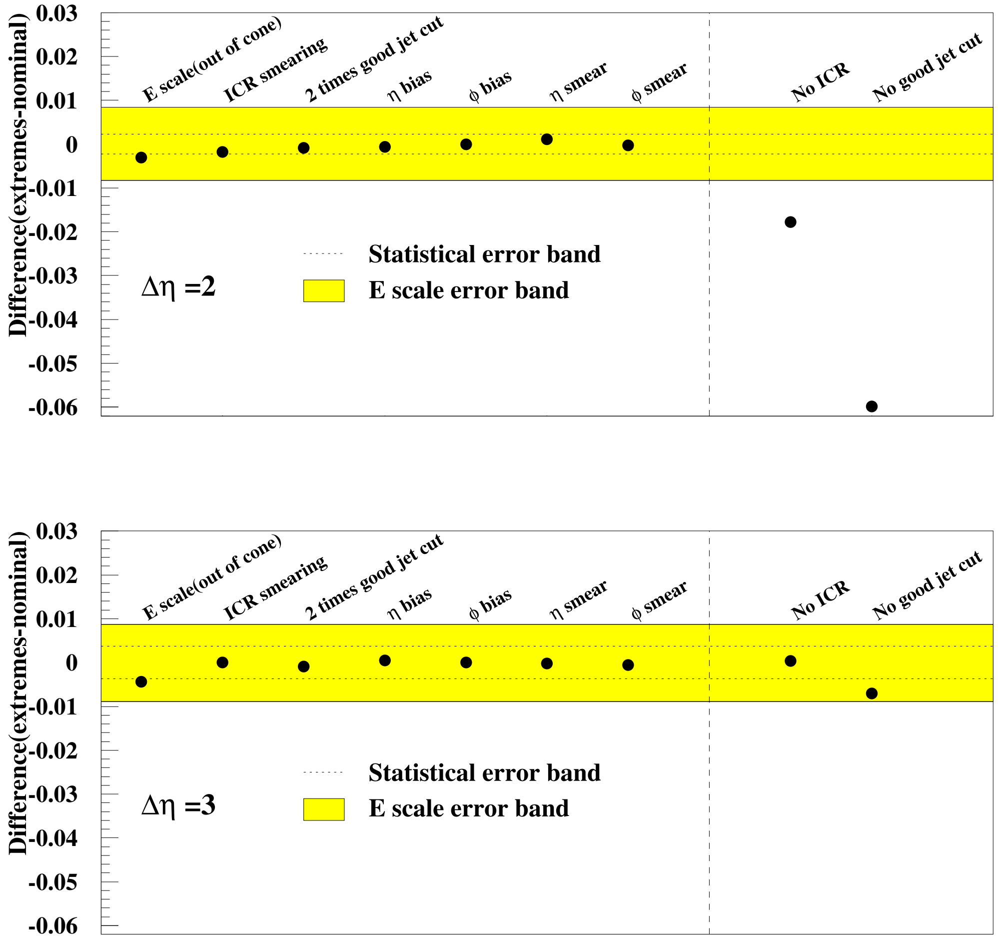

Figure 7.7 : continues.

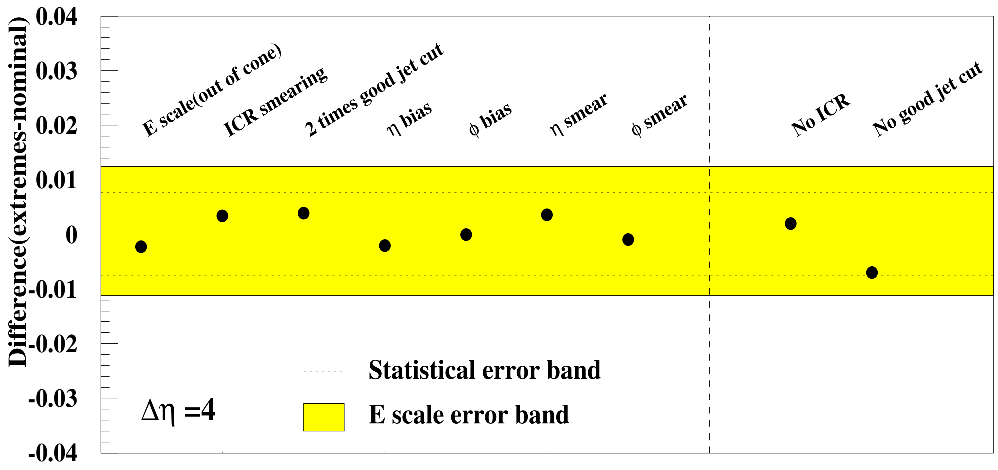

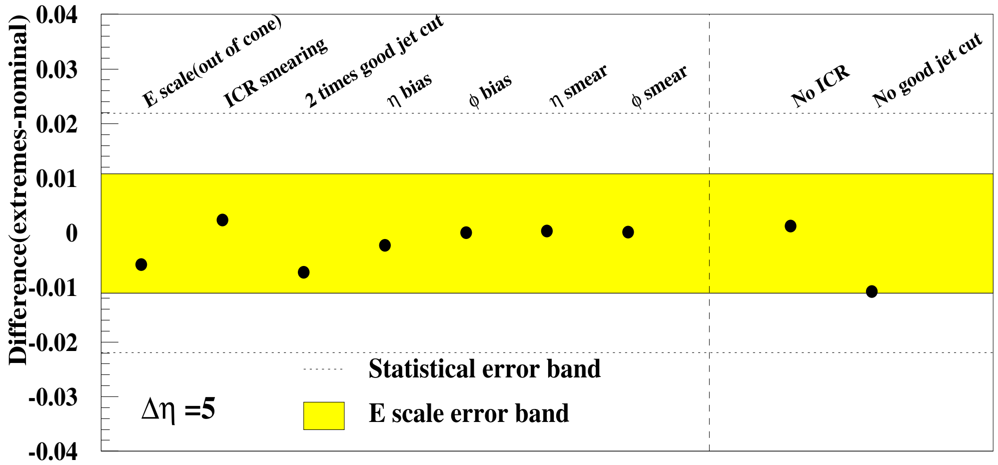

Figure 7.7 : continues.

Chapter 8

Theoretical Predictions

In order to compare the result of our analysis with the theoretical predictions, we use a recently developed next-to-leading order Monte Carlo, JETRAD [79], and a parton shower Monte Carlo, HERWIG (Hadron Emission Reactions With Interfering Gluons) [63]. The BFKL resummation prediction by Del Duca and Schmidt [45, 86] is also used. In JETRAD and HERWIG a jet is defined by a cone of radius R=0.7 which provides jet cross sections approximately independent of renormalization scale μ [31] and the approximated DØ jet position definition was utilized for partons.

8.1 JETRAD

An exact next-to-leading order (NLO) calculation [79] is implemented in the JETRAD Monte Carlo as tree and one loop corrections at $O(\alpha_s^3)$. At this order two or three partons can be generated in the final state. This next-to-leading order calculation provides two important improvements over the leading order predictions. First it reduces the theoretical uncertainties due to the choice of the renormalization and factorization scales and thereby provides more reliable predictions. Second the cross sections become dependent on the jet clustering algorithm.

In the high energy collision of hadrons partons are generated with large momen-

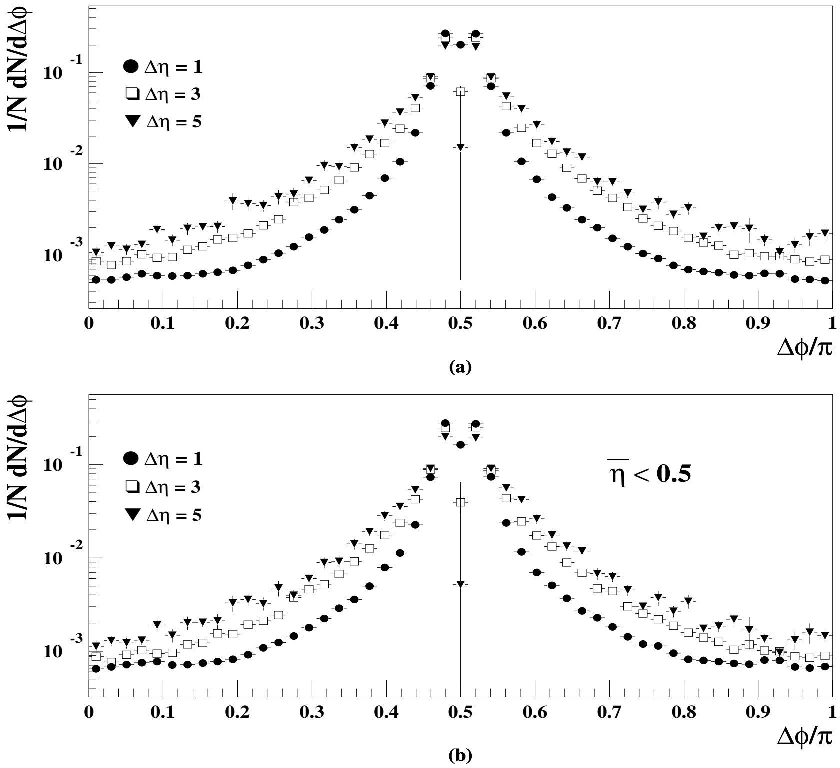

Figure 8.1: The distributions of azimuthal angle differences for various rapidity intervals 1, 3, and 5 (a) without $\bar{\eta}$ cut and (b) with $\bar{\eta} < 0.5$ in JETRAD. The distributions are normalized to unit area.

tum transfer and each parton evolves into a jet. But partons are connected by color strings and the hadrons in a single jet may not be from a single parton. Therefore a quantitative comparison between theory and experiment is hindered by ambiguities which appear in the experimental and theoretical jet definition. Experimentally one needs to use a specific definition of jets based on detected hadronic final states. For instance when we define a jet using a cone algorithm of radius R the measured cross section depends on the cone size for the jets. On the theoretical side the jet ambiguity is related to perturbation theory beyond the Born level. At the Born level (α_s^2), one may expect that each outgoing parton hadronizes into a narrow jet of particles. However, at one order beyond the Born level (α_s^3) a jet may consist of two partons instead of just one and have internal structure. Therefore jet cross sections calculated to order α_s^3 depends on the jet definition.

The distributions of azimuthal angle differences $\Delta\phi$ from JETRAD are normalized and plotted in Fig. 8.1 using the same kinematic cuts as in the experimental data analysis, $|\eta| < 3.0$, $E_T^{min} > 20$ GeV and $E_T^{forward} > 50$ GeV (or $E_T^{backward} > 50$ GeV). Due to loop diagrams at $O(\alpha_s^3)$ the two parton matrix elements can have negative weights and as a result give negative cross sections which is a result of perturbative QCD being unstable with respect to infrared radiations. The central bin in Fig. 8.1 shows smaller cross sections compared to the adjacent bins since most of the events in this bin are dijet events with negative cross sections. Those two jets are highly correlated in transverse momenta and azimuthal angles.

In order to see the effect in the central bin we have calculated the average of $\cos(\pi - \Delta\phi)$ with and without the central bin. Both results are shown in Fig. 8.2(a). The differences between them become smaller as the rapidity interval increases for both moments n=1 and 2. This shift agrees with our expectation that the removal of one central bin where the correlation is maximal results in lower $< \cos(\pi - \Delta\phi) >$ values or more decorrelation. Since the distribution of $< \cos(\pi - \Delta\phi) >$ using all bins shows reasonable linearity as a function of rapidity interval and $< \cos(\pi - \Delta\phi) >$ is near one at $\Delta\eta = 0$ as kinematically expected, we may conclude that $< \cos(\pi - \Delta\phi) >$ using all bins appears physically meaningful despite the abnormal cross sections in the $\Delta\phi$ plots. This was suggested by an author of JETRAD [80].

We also explored several other features of perturbative QCD: renormalization scale dependence, uncertainty in parton distribution functions and jet algorithm dependence.

- **Renormalization scales :** Even though the renormalization scale (μ) dependence of NLO calculation is less than LO calculation, NLO calculation is

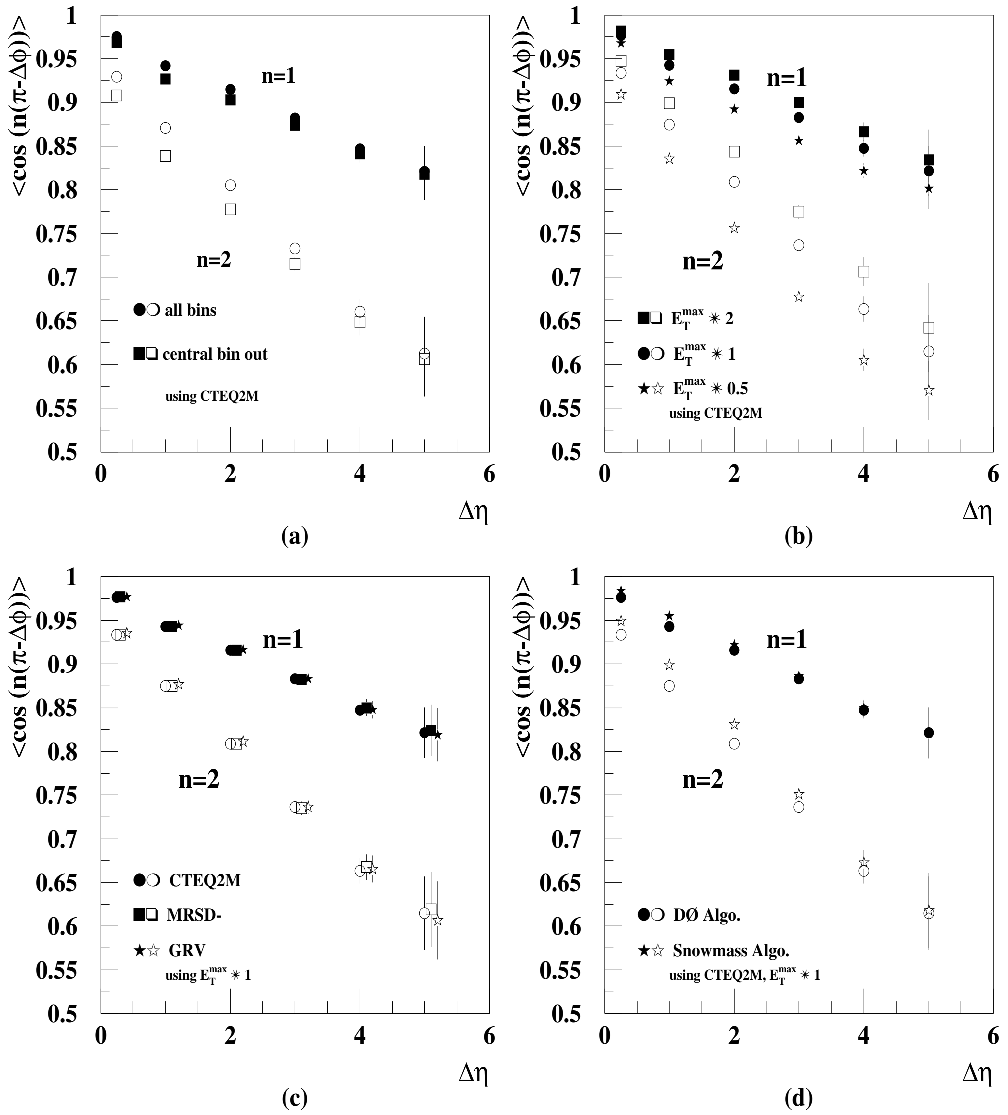

Figure 8.2: (a) JETRAD $< \cos(\pi - \Delta\phi) >$ values with and without exclusion of the one central bin, (b) $< \cos(\pi - \Delta\phi) >$ values using various renormalization scales, (c) using different pdf's, (d) using two different jet algorithms.

still expected to depend on μ. We used the maximum transverse energy E_T^{max} of a jet, two times E_T^{max} and one half E_T^{max} as renormalization scales and calculated the averages of $\cos(\pi - \Delta\phi)$ as shown in Fig. 8.2(b). The influence of different renormalization scales is almost independent of rapidity intervals $\Delta\eta$ and the maximum difference in the $< \cos(\pi - \Delta\phi) >$ is found to be 0.026 for the first moment and 0.058 for the second moment. We have also found that the decorrelation is inversely proportional to the magnitude of renormalization scales.

- **Parton distribution functions :** Since cross sections are a convolution of parton distribution functions and matrix elements, various parton distribution functions described in section 2.5.5 were tested as shown in Fig. 8.2(c). The maximum difference is rather small compared to the renormalization scale dependence, 0.005 for the first moment and 0.013 for the second moment.

- **Jet algorithms :** Since only two or three partons are available as jet seeds next-to-leading order predictions invoke ambiguity in the definition of the transverse energy and position of jets [81]. Thus the Snowmass jet algorithm as mentioned in section 3.2 and 5.1 is also used and the result is shown in Fig. 8.2(d). The difference in $< \cos(\pi - \Delta\phi) >$ between Snowmass and DØ decreases as the rapidity interval increases. The maximum differences are 0.008 and 0.017 for the first and the second moments respectively.

8.2 HERWIG

HERWIG is a general purpose particle physics event generator for the simulation of hadron-hadron collisions. It uses the parton shower approach for initial state and final state QCD radiation and includes color coherence effects and azimuthal correlations both within and between jets [63]. The final state of a QCD event consists of multi-partons or multi-particles through parton shower and particle fragmentation. The simulation of QCD jet production can be factorized as follows:

- **Hard subprocess :** Each hard parton-parton collision ($2 \longrightarrow 2$) is computed exactly to leading order (α_s^2) using perturbative QCD and produces only two partons. The hard process momentum transfer scale Q sets the boundary conditions for the initial and final state parton showers.

- **Final state emission :** Each outgoing parton from a hard process emits partons according to the Altarelli-Parisi splitting functions (GLAP evolution, see section 2.5) and generates a shower of partons. The available phase space for parton emission is restricted to an angular ordered region. At each parton emission, the emission angle of a parton is smaller than that of the previous parton emitted. The amount of emission depends on the virtuality of each parton controlled by the momentum transfer scale Q.

- **Initial state emission :** An incoming parton in the hard subprocess generates a shower of partons through "backward" Altarelli-Parisi evolution. Since the parton that participated in the hard subprocess is evolved from an initial parton inside a hadron as described in Chapter 2.5 this parton emits daughter partons according to the backward evolution function until it reaches its initial state in the hadron.

- **Hadronization process :** A QCD event contains a number of partons from the initial and final state emissions. These partons are converted into hadrons to construct a realistic event. This hadronization occurs at low momentum transfer scale and the perturbation theory is not applicable. Therefore, a phenomenological hadronization model is required. HERWIG adopted a cluster hadronization model which is local in color and independent of the hard process and the energy [63].

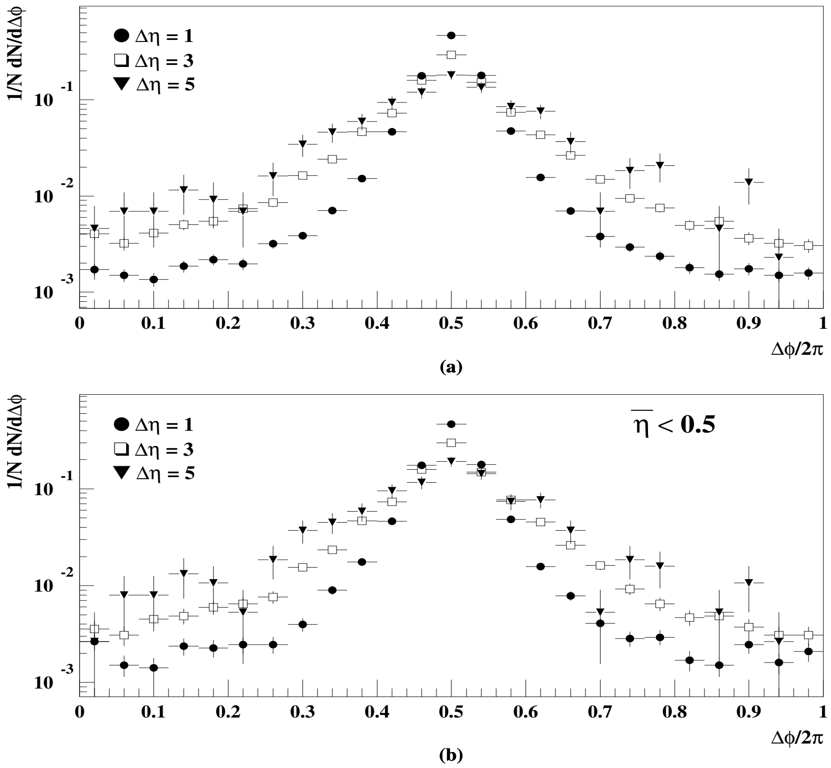

Figure 8.3: The distributions of the azimuthal angle differences for various rapidity intervals 1, 3, and 5 (a) without $\bar{\eta}$ cut and (b) with $\bar{\eta} < 0.5$ using the parton jets of HERWIG. The distributions are normalized to unit area.

In hadron-hadron collisions spectator partons from the incoming hadrons have color connections with the partons participating in the hard subprocess. These color connections mimic a soft collision and the interactions between the spectator beams produce soft collisions. These soft collisions are called underlying events and produce additional soft hadrons in the QCD events. This feature is also implemented in HERWIG.

We have generated 200,000 QCD events with the HERWIG event generator using the CTEQ2MS parton distribution function [82]. The standard DØ jet algorithm

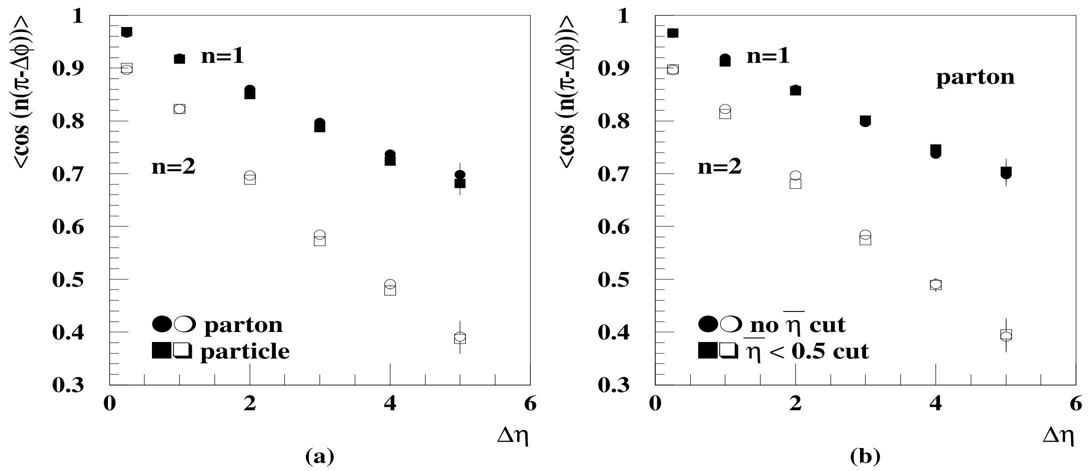

Figure 8.4: The average of $\cos(\pi - \Delta\phi)$ using HERWIG events, (a) for comparison between parton and particle jets and, (b) for the effects of rapidity boost cut.

was used to reconstruct parton and particle jets using partons and particles as jet seeds instead of the calorimeter towers. The analysis cuts used for the data and JETRAD events were utilized for these HERWIG events. The azimuthal angle differences between the two tagging parton jets are plotted in Fig. 8.3. Figure 8.3 (a) shows the increase in the decorrelation between tagging jets. In these distributions, as the rapidity interval increases, the center peaks diminish and the tails grow. Figure 8.3 (b) shows the same decorrelation trend when the rapidity boost cut $\bar{\eta} < 0.5$ applied. These normalized distributions, with and without the rapidity boost cut, are similar except for the size of the statistical errors.

Figure 8.4 shows the averages of $\cos(n(\pi - \Delta\phi))$ for parton and particles jets. There is a linear relationship between the rapidity interval and $< \cos(\pi - \Delta\phi) >$. The averages of $\cos(\pi - \Delta\phi)$ for parton and particle jets are consistent within statistical errors. The difference in the first moment at $\Delta\eta = 5$ is 0.019 which is less than the statistical error 0.022. For the second moment, the difference in the $\Delta\eta = 5$ bin is

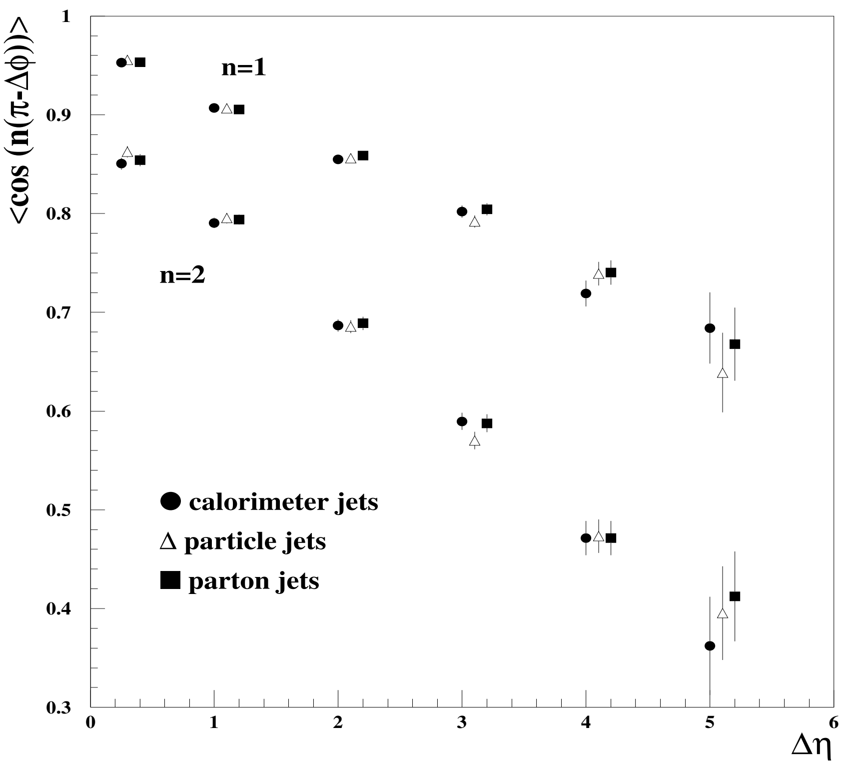

Figure 8.5: The evolution of azimuthal angle decorrelations from parton level to particle and calorimeter levels. Particle jets contain the effects of fragmentation and calorimeter jets contain the effects of particle showering in the calorimeter.

much less, 0.004. The values of $< \cos(\pi - \Delta\phi) >$ with and without the rapidity boost cut are compared as shown in Fig. 8.4. As in the experimental data and JETRAD the difference is negligible being only 0.004 in the last bin for the first moment.

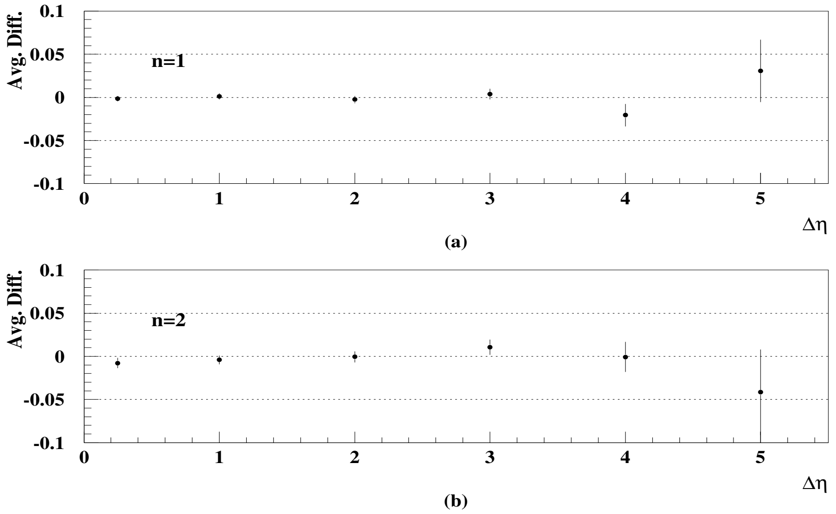

Figure 8.6: The showering uncertainty: $\frac{(<\cos>_{cajet}-<\cos>_{pejet})+(<\cos>_{cajet}-<\cos>_{pjet})}{2}$ for (a) the first moment and (b) the second moment.

8.3 GEANT Detector Simulation

We have used parton or particle jets in the Monte Carlo study. The jets in the experimental data are reconstructed from the calorimeter cells or towers which contain the energy of particles deposited through electromagnetic and hadronic showering. After energy smearing in the calorimeter, the characteristics of an event can vary, e.g. a different number of jets, different energy for a jet. In order to study these showering effects we have generated 50,000 HERWIG events and performed a full detector simulation based on GEANT [64]. In the event generation the leading jet is required to have $|\eta| > 1.6$ in order to reduce the computer processing time and populate the bins of large rapidity interval. This requirement is found to produce biases for small rapidity intervals $\Delta\eta = 0, 1$ and 2, but not for large rapidity intervals $\Delta\eta = 4$ and 5.

Jets in the calorimeter are reconstructed using the standard DØ jet algorithm and the energies of jets are corrected by the jet energy scale. The averages of $\cos(\pi - \Delta\phi)$

at parton, particle and calorimeter levels are calculated and compared in Fig. 8.5. The effect of fragmentation is contained in particle jets and the showering effect is in the calorimeter jets. All these levels appear to be consistent within statistical errors. Since these values are from the same set of HERWIG samples these statistical errors are highly correlated. Therefore the showering uncertainty is defined as follows:

$$\frac{(< \cos >_{cajet} - < \cos >_{pejet}) + (< \cos >_{cajet} - < \cos >_{pjet})}{2} \tag{8.1}$$

where $< \cos >$ is the average of $\cos(\pi - \Delta\phi)$ for parton (pjet), particle (pejet), and calorimeter jets (cajet). These differences are plotted in Fig. 8.6. The error bars are statistical. The difference at $\Delta\eta = 5$ is 0.03 for the first moment and 0.042 for the second moment.

8.4 BFKL Prediction

Using the LO CTEQ parton distribution functions [85] with the renormalization and factorization scales set to $\mu^2 = p_{t1}p_{t2}$ (where p_{t1} and p_{t2} are transverse momenta of two tagging jets), Del Duca and Schmidt used the BFKL resummation technique [45, 86] and calculated the average of $\cos[n(\pi - \Delta\phi)]$ as shown in Fig. 8.7. The same kinematic cuts are used as in the experimental data analysis. The boost cut, $\bar{\eta} < 0.5$ does not change the average of $\cos(\pi - \Delta\phi)$ very much. Since the prediction is valid at large rapidity interval $< \cos(\pi - \Delta\phi) >$ is shown from $\Delta\eta = 2$. This BFKL prediction shows steeper slopes than the experimental data and HERWIG, which indicates more radiation is expected between the two jets.

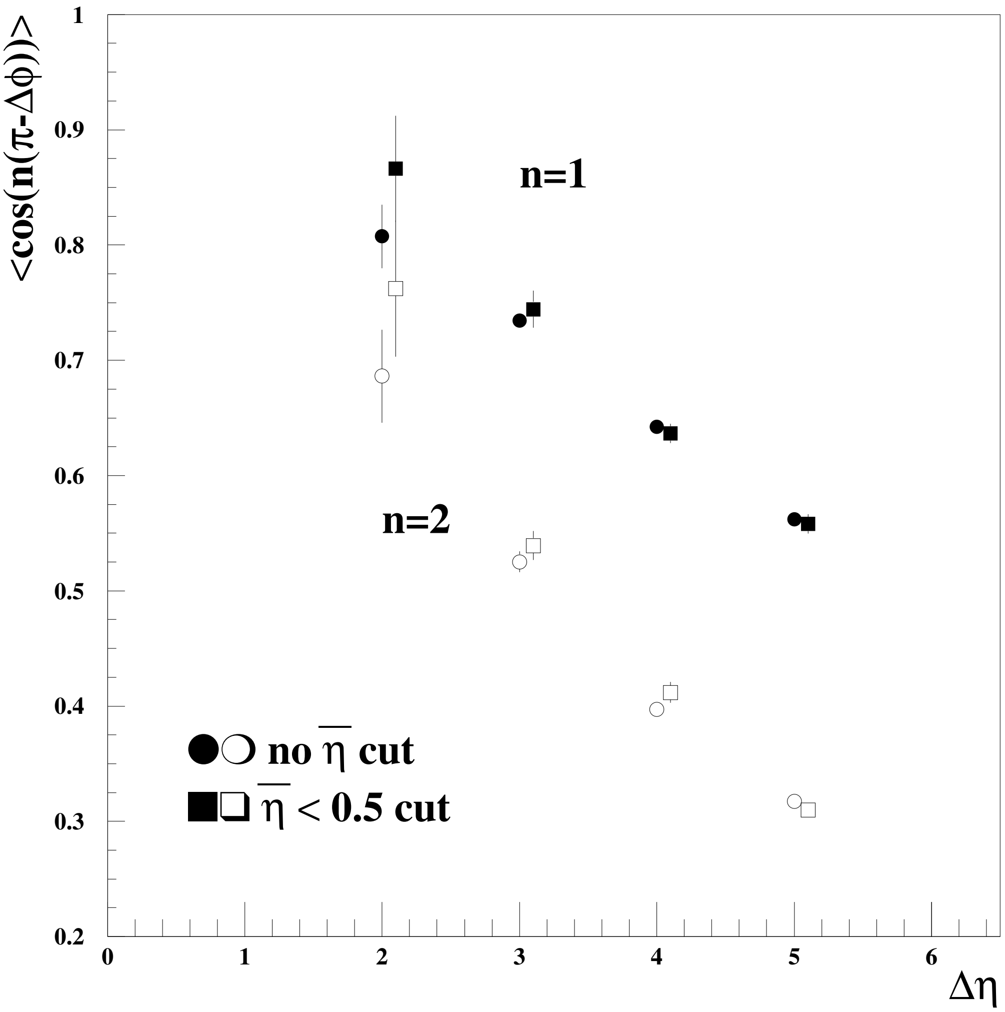

Figure 8.7: The average of $\cos[n(\pi - \Delta\phi)]$ with and without $\bar{\eta}$ cut using BFKL resummation.

Chapter 9

Comparisons to Theory and Conclusions

9.1 Experimental Results and Comparison

In this section, we compare experimental results with various theoretical predictions. JETRAD [79] is an exact next-to-leading order (α_s^3) Monte Carlo calculation for inclusive QCD 2 jet processes. HERWIG is a parton shower Monte Carlo including initial and final state QCD radiation, color coherence effects and azimuthal correlations both within and between jets. These higher order effects are calculated by resumming the leading logarithmic terms to all orders in α_s. The leading log approximation of Del Duca and Schmidt [86] is based on the BFKL resummation. The averages of $\cos[n(\pi - \Delta\phi)]$ for these various theoretical predictions and the data are plotted as a function of rapidity interval in Fig. 9.1 and Fig. 9.2. The second moment n=2 of Fig. 9.2 might be sensitive to the shape variation of $\Delta\phi$ distribution. The error bars for JETRAD, HERWIG are the Monte Carlo statistical uncertainties, and the errors for the BFKL predictions represent the numerical calculation errors.

On the experimental data the uncertainty related to the jet energy scale is rep-

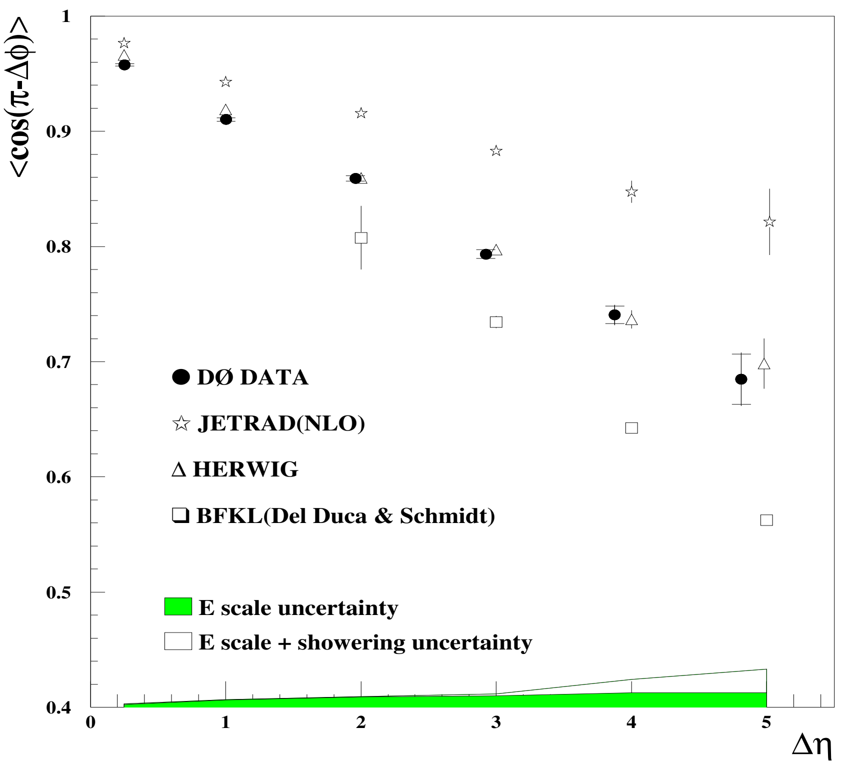

Figure 9.1: The average of $\cos(\pi - \Delta\phi)$ as a function of rapidity interval, for the experimental data, JETRAD, HERWIG, and the BFKL predictions of Del Duca and Schmidt. (for the first moment, n = 1)

resented as a gray band at the bottom of the plots. These energy scale uncertainties and the calorimeter showering uncertainties are added in quadrature, and these combined uncertainties are represented as an open band at the bottom of the plot. Other systematic errors and the statistical errors are added in quadrature and represented as bars on the data points. The errors within horizontal bars on each data point indicate statistical errors. The detector showering uncertainty at $\Delta\eta = 5$ is the largest among all systematic uncertainties.

As shown in the figures the next-to-leading order prediction underestimates the

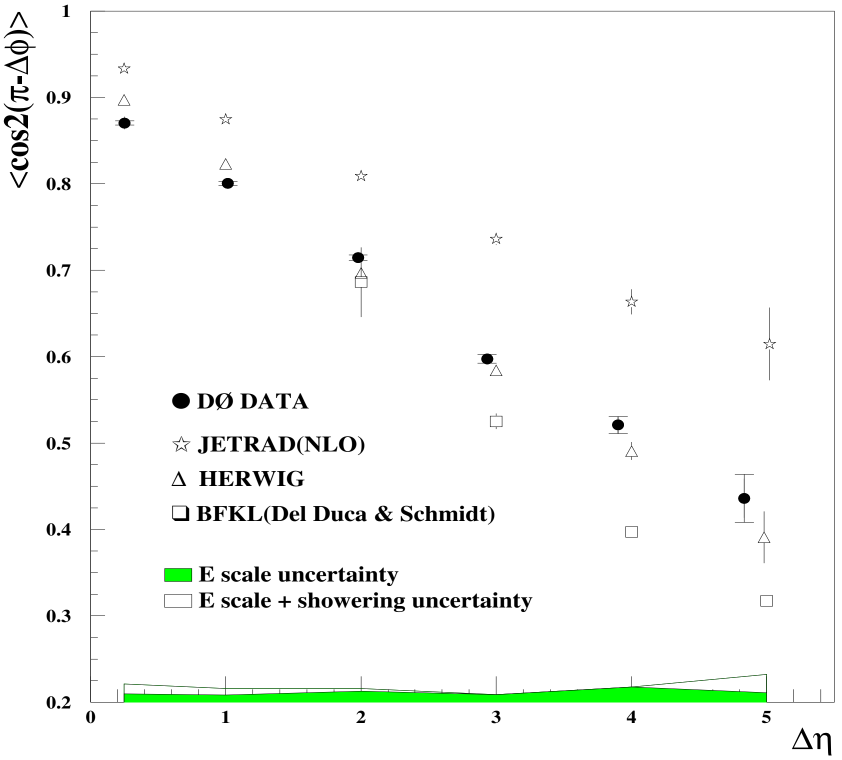

Figure 9.2: The average of $\cos 2(\pi - \Delta\phi)$ as a function of rapidity interval, for the experimental data, JETRAD, HERWIG, and the BFKL predictions of Del Duca and Schmidt. (for the second moment, n = 2)

decorrelation at large rapidity separation while the BFKL calculations of Del Duca and Schmidt predict too much decorrelation over their range of validity. HERWIG, however, seems to describe the data rather well over the entire rapidity interval studied.

9.2 Conclusions

We have made the first measurement of azimuthal decorrelation as a function of rapidity separation in inclusive dijet samples at the center of mass energy $\sqrt{s} = 1.8$ TeV using the DØ detector. We have calculated the azimuthal angle difference between the two jets most widely separated in rapidity. The distributions of the azimuthal angle differences are used to calculate the averages of $\cos(\pi - \Delta\phi)$ and the results were compared to various theoretical predictions as shown in Fig. 9.1 and Fig. 9.2.

JETRAD, an exact next-to-leading order Monte Carlo, shows more azimuthal correlation at large rapidity interval than the experimental data since only two and three jets are available in the final states. HERWIG, the parton shower Monte Carlo using the leading log approximation technique (GLAP evolution), describes the data rather well for all rapidity intervals. A prediction based on BFKL resummation overestimates the decorrelation in the large rapidity interval. The characteristics of GLAP evolution is the strong ordering in the transverse momenta of emitted partons and involves hard and soft gluon radiation. On the other hand, BFKL evolution is based on mostly soft gluon radiation. This difference may be the reason that BFKL resummation estimates more decorrelation than HERWIG. This also indicates that the Tevatron energy might not be high enough to explore the QCD regime requiring the leading order BFKL approximation, or the smaller transverse momentum threshold and larger rapidity interval are necessary to probe the BFKL regime.

Bibliography

[1] F. Abe *et al.*, *Phys. Rev. Lett.* **68**, 1104(1992).

[2] F. Abe *et al.*, *Phys. Rev. Lett.* **69**, 2896(1992).

[3] A.H. Mueller, Proc. of the 2nd Workshop on Small-x and Diffractive Physics at the Tevatron, (Fermilab, Batavia, IL USA, Sep. 1994).

[4] L.N. Lipatov, *Sov. J. Nucl. Phys.* **23**, 338(1976);
E.A. Kuraev, L.N. Lipatov, V.S. Fadin, *Sov. Phys. JETP* **44**, 443(1976); *Sov. Phys. JETP* **45**, 199(1977);
Ya.Ya. Balitsky, L.N. Lipatov, *Sov. J. Nucl. Phys.* **28**, 822(1978)

[5] S. Abachi, *et. al.*, *Nucl. Instr. and Math.* **A338**, 185(1994)

[6] M. Gell-Mann, *Phys. Lett.* **B8**, 214(1964); G. Zweig, CERN-Report-8182/TH-401(1964);CERN-Report-8419/TH-412(1964).

[7] O.W. Greenberg, *Phys. Rev. Lett.* **13**, 598(1964).

[8] M. Shochet, The Physics of Proton Antiproton Collisions, FERMILAB-Conf-91/341-E.

[9] C.N. Yang, R.L. Mill, *Phys. Rev.* **96**, 191(1954).

[10] CTEQ collaboration, Handbook of Perturbative QCD, Version1.0: April 1993.

[11] J.D. Bjorken, *Phys. Rev.* **179**, 1547(1969); *Phys. Rev.* **163**, 1767(1967).

[12] J. Yu, Ph.D. Thesis (New York State University at Stony Brook), 1993.

[13] A. Bodek *et al.*, *Phys. Rev.* **D20**, 1471(1979).

[14] R.D. Field, Applications of perturbative QCD, Addison Wesley Inc., Chap. 4.

[15] J. Collins, D. Soper and G. Sterman, "Factorization of Hard Processes in QCD", in *Perturbative Quantum Chromodynamics*, ed. by A.H. Mueller, (1989).

[16] T. Ahmed, *et al.* H1 Collaboration, DESY95-006, (Jan. 1995).

[17] F. Halzen, A. Martin, Quarks and Leptons, John Wiley & Sons Inc., Chap. 9.

[18] ZEUS Collaboration, DESY94-143, (Aug. 1994).

[19] E. Levin, Lectures given at the LAFEX, CBPF, Rio De Janeiro, CBPF-NF-010/95, Sep. 1994.

[20] J. Kwieciński,INP-1681-PH, Review talk presented at "QCD94",7-13 Jul. 1994.

[21] A.H. Mueller, H. Navelet, *Nucl. Phys.* **B282**, 727(1987).

[22] S. Catani, DEF 207/6/94, Invited talk at *Results and Perspective in Particle Physics,* La Thuile, Mar. 1994.

[23] M. Glück, E. Reya, A. Vogt, *Zeit. Phys.* **C53**, 127(1992); *Phys. Lett.* **306B**, 391(1993).

[24] A.D.Martin, R.G. Roberts, W.J. Stirling, *Phys. Lett.* **306B**, 145(1993).

[25] CTEQ Collaboration, *Phys. Lett.* **304B**, 159(1993).

[26] A.D.Martin, R.G. Roberts, W.J. Stirling, RAL-94-055,DTP/94/34, Jun. 1994.

[27] H.L. Lai, *et al.*, MSU-HEP-41024, CTEQ-404, Oct. 1994.

[28] H1 Collaboration, DESY 95-081, May. 1995.

[29] G. Marchesini, Proc. of Workshop "QCD at 200 TeV", Eric 1990, Plenum press, 183(1992); IFUM 486-FT, Nov. 1994.

[30] S.D. Ellis, Z. Kunzt, D.E. Soper, *Phys. Rev. Lett.* **64**, 2121 (1990); *Phys. Rev. D* **40**, 2188(1989).

[31] S.D. Ellis, Z. Kunzt, D.E. Soper, *Phys. Rev. Lett.* **69**, 1496(1992).

[32] W.T. Giele, E.W.N. Glover, D.A. Kosower, *Phys. Rev. Lett.* **73**, 2019(1994); *Nucl. Phys.* **B403**, 633(1993).

[33] F. Abe *et al.*, CDF collaboration, *Phys. Rev. Lett.* **68**

[34] V. Del Duca, Talk presented at the 10th Topical Workshop on Proton-Antiproton Collider Physics, Ferimlab, Batavia, IL, May 9-13, 1995.

[35] S. Abachi *et al.*, DØ collaboration, *Phys. Rev. Lett.* **72**, 2332(1994).

[36] T. Regge, Neuvo Cimento **14**, 951(1959); P.D.B. Collins, Introduction to Regge Theory, Cambridge University Press, (1977).

[37] A. Donnachie, Univ. of Manchester, M/C-TH 94/07 (1994).

[38] F.E. Low, *Phys. Rev.* **D12**, 163(1975); S. Nussinov, *Phys. Rev.* **D14**, 246(1976).

[39] A.H. Mueller, W.K. Tang, *Phys. Lett.* **284B**, 123(1992); V Del Duca, W.K. Tang, *Phys. Lett.* **312B**, 225(1993).

[40] A.R. Baden, N.J. Hadley, DØ Note 957

[41] S.D. Ellis, Proc. Summer Study on high Energy Physics, *Research Direction for the Decade*, Snowmass, CO. Jun. 25-Jul. 13, 1990.

[42] B. Flaugher, Kmeier, Proc. Summer Study on high Energy Physics, *Research Direction for the Decade*, Snowmass, CO. Jun. 25-Jul. 13, 1990.

[43] J.E. Huth, *et al.*, Proc. Summer Study on high Energy Physics, *Research Direction for the Decade*, Snowmass, CO. Jun. 25-Jul. 13, 1990.

[44] W.J. Stirling, *Nucl. Phys.* **B423**, 56(1994)

[45] V. Del Duca, DESY-95-023, Mar. 1995;
V. Del Duca, C. R. Schmidt, DESY-94-163, Invited talk at 6th Rencontres de Blois: The Heart of the Matter: from Nuclear Interactions to Quark - Gluon Dynamics, Blois, France, Jun. 20-25 1994;
V. Del Duca, C. R. Schmidt, DESY-94-128, Invited talk at High Energy Physics: QCD Workshop 94, Montpellier, France, 7-13 Jul 1994;
V. Del Duca, C. R. Schmidt, *Phys. Rev.* **D51**, 2150(1995);
V. Del Duca, C. R. Schmidt, *Phys. Rev.* **D49**, 4510(1994).

[46] B.L. Combridge, J. Kripfganz, J. Ranft, *Phys. Lett.* **70B**, 234(1977)

[47] B.L. Combridge, C.J. Maxwell, *Nucl. Phys.* **B239**, 429(1984)

[48] V. Radeka, *IEEE Trans. Nucl. Sci.* **21, No. 1**, 51(1974).

[49] W.W.M.Allison, P.R.S. Wright, *Formulae and Methods in Experimental Data Evaluation,* **2** *ed. R.K. Bock, et al*, (EPS, CERN), 1984.

[50] S. Abachi, *et. al.*, *Nucl. Instr. and Math.* **A324**, 53(1993)

[51] P.C. Bhat, DØ collaboration, Fermilab-Conf-93/049-E *presented at 7th DPF at Fermilab*, Nov. 1992.

[52] R.V. Astur, Ph.D. Thesis (Michigan State University), 1992.

[53] M. Bhattacharjee, *et. al.*, DØ Note 2557 (unpublished), 1994.

[54] R. Williams, *Nucl. Instr. and Math.* **A259**, 389(1987);**A265**, 53(1986)

[55] N.J. Hadley, DØ Note 904 (unpublished).

[56] B.J. May, Ph.D. Thesis, University of Arizona(1994), (unpublished).

[57] A. Milder, R.V. Astur, DØ Note 1595 (unpublished).

[58] Combined 1994 Analysis of the LEP experiments, by the LEP electroweak group, (to be published)

[59] U. Heintz, DØ Note 1758 (unpublished).

[60] F. Abe, *et al.*, (CDF Collaboration), Phys. Rev. Lett. **69**, 2896(1992)

[61] M. Bhattacharjee, *et al.*, DØ Note 2197 (unpublished).

[62] C.L. Kim *et al.*, DØ Note 2477 (unpublished).

[63] G. Marchesini, M. Webber, Nucl. Phys. **B310** 461(1988); I.G. Knowles,Nucl. Phys. **B310** 571(1988); G. Marchesini, *et al.*, Comp. Phys. Comm. **67** 465(1992).

[64] F. Carminati, *et al.*, GEANT User's Guide, CERN Program Library (Dec.1991); A.M. Jonckheere, Proc. Argonne National Laboratory Detector Simulation Workshop (Aug.1987); DØ Note 638 (unpublished).

[65] B. Abbott, K. Streets DØNote 2176 (unpublished).

[66] B. Klima, C. Stewart DØNote 905 (unpublished).

[67] V.D. Elvira, DØ Note 2173 (unpublished).

[68] B. Hirosky DØNote 2405 (unpublished).

[69] J. Bantly, *et al.*, DØ Note 2401 (unpublished).; DØ Note 2544 (unpublished).

[70] T.L. Geld, DØ Note 2474 (unpublished); R.V. Astur, F. Nang, DØ Note 2135 (unpublished).

[71] N. Amos *et al.*, DØ Note 2031 (unpublished).

[72] N. Amos, *et al.*, *Phys. Lett.* **B243**, 158(1990).

[73] F. Abe, *et al.*, FERMILAB-Pub-93/232-E(1993); FERMILAB-Pub-93/233-E(1993); FERMILAB-Pub-93/232-E(1994), submitted to *Phys. Rev.* **D.**

[74] J. Bantly, *et al.*, DØ Note 1996(unpublished).

[75] J. Bantly, DØ Note 1849(unpublished).

[76] V.D. Elvira, J. Blazey, R. Astur, DØ Note 1763 (unpublished).

[77] M. Bhattacharjee, V.D. Elvira, J. Blazey, DØ Note 2197 (unpublished).

[78] R. Astur, DØ Note 1662 (unpublished).

[79] W.T. Giele, E.W.N. Glover, D.A. Kosower, *Nucl. Phys.***B403**, 633(1993).

[80] private communication with W.T. Giele

[81] S. Abachi *et al.*, *Phys.Lett.* **B357**, 500(1995).

[82] H. Plothow-Besch, *PDFLIB: A library of all available Parton Density Functions of the Nucleon, the Pion and the Photon and the corresponding α_s Calculations, Comp. Phys. Comm.* **75**, 396(1993).

[83] C. L. Kim, a talk in QCD group, DØ Workshop on QCD Physics, Tucson, Arizona, Jan. 8-13, 1995.

[84] R. V. Astur, DØ news (general folder) #2427, #2479 , 1994.

[85] J. Botts *et al.*, *Phys.Lett.* **B304**, 159(1993).

[86] V. Del Duca, C. R. Schmidt, *Private Communications.*